# NEW CROSS SECTION MEASUREMENTS FOR THE REACTION $^{16}O(p, \gamma)^{17}F$ WITH AN EXTRAPOLATION TO ASTROPHYSICAL ENERGIES

by

THOMAS HAMMOND HALL

B.A., Earlham College, Richmond, Indiana, 1963

M.Sc., Indiana University, 1966

A THESIS SUBMITTED IN PARTIAL FULFILMENT OF THE REQUIREMENTS FOR THE DEGREE OF DOCTOR OF PHILOSOPHY

in the Department

of

Physics

We accept this thesis as conforming to the required standard

THE UNIVERSITY OF BRITISH COLUMBIA

JUNE, 1974

In presenting this thesis in partial fulfilment of the requirements for an advanced degree at the University of British Columbia, I agree that the Library shall make it freely available for reference and study. I further agree that permission for extensive copying of this thesis for scholarly purposes may be granted by the Head of my Department or by his representatives. It is understood that copying or publication of this thesis for financial gain shall not be allowed without my written permission.

Department of Physics

The University of British Columbia
Vancouver 8, Canada

Date August 8, 1974

## ABSTRACT

Improved absolute cross section and angular distribution measurements have been made for the direct radiative capture of protons by $^{16}O$. Gamma ray yields have been obtained at four center of mass energies from 1.288 to 2.404 Mev for direct capture to the $d^{+}_{5/2}$ ground state of $^{17}F$ and at seven center of mass energies from 0.795 to 2.404 Mev for direct capture to the $s^{+}_{1/2}$ first excited state. Angular distribution data have been obtained for both transitions for three angles at 0.778 Mev and four angles at each of 1.289, 1.840 and 2.306 Mev in the center of mass. In addition, separate measurements have determined differential cross sections to ± 0.5% for the elastic scattering of protons by $^{16}O$ at 171°.5 in the center of mass from the energy region of pure Rutherford scattering to 2.0 Mev bombarding energy.

The direct capture cross section was normalized to the elastic scattering cross section by a technique which allowed simultaneous observation of both reactions. This was made feasible by the development of transmission targets consisting of a layer of $WO_3$ sputtered onto a self-supporting gold backing. A large volume Ge(Li) detector was used to observe the gamma rays and to provide accurate measurements of the gamma ray yields. The present measurements agree to within 5% with the most recent cross section calculations of Chow (1973).

The reaction $^{16}O(p, \gamma)^{17}F$ is important in stellar astrophysics through the role it plays in the CNO bi-cycle. Its cross section at stellar energies affects the relative abundances of the catalyst nuclei

carbon, nitrogen and oxygen in those stars which are burning hydrogen by this cycle of reactions. By lending confidence to, and providing an accurate normalization for the direct capture calculations, the present measurements allow a reliable extrapolation of the theory to stellar thermal energies.

For center of mass energies below 100 Kev, the contributions to the astrophysical S-factor from capture to the $1/2^+$ first excited state and the $5/2^+$ ground state of $^{17}F$ can be expressed as

$$S_{(1/2^+ \text{ state})}(E) = (9.245 - 0.0329E + 0.00007E^2) \pm 4.1\% \quad \text{Kev barns}$$

$$S_{(5/2^+ \text{ state})}(E) = (0.302 + 0.0002E) \pm 6.8\% \quad \text{Kev barns.}$$

The large energy dependence of $S_{(1/2^+ \text{ state})}$, in particular its dramatic increase with decreasing energy in the region of thermal energy, arises from the low binding energy of the $1/2^+$ first excited state. Consequently, the $^{16}O(p, \gamma)^{17}F$ reaction rate at stellar thermal energies is determined almost entirely by direct capture to this state.

TABLE OF CONTENTS

TABLE OF CONTENTS
(Continued)

# LIST OF TABLES

# LIST OF ILLUSTRATIONS

# LIST OF ILLUSTRATIONS
(Continued)

## ACKNOWLEDGEMENTS

I wish to express my appreciation to Professor G.M. Griffiths, without whom this thesis would never have materialized. He gave to me the initial interest and sense of discipline which helped me thoughout this work. He also provided the necessary technical supervision and assistance when it was needed.

I also wish to thank Martin Salomon, who gave me considerable assistance during the early stages of this work, and Peter Bosman and the rest of the Van de Graaff staff who diligently maintained the Van de Graaff in a usable state.

I am indebted to the Atomic Energy of Canada and the National Research Council from whom I received financial assistance.

Finally, I want to thank my wife, Pamela, for her continued patience, cooperation and guidance.

# CHAPTER 1

# INTRODUCTION

## 1.1 DIRECT RADIATIVE CAPTURE

Direct nuclear reactions result when a particle makes a direct or one step transition from an initial continuum state to a final bound state, or unbound resonant state of lower energy, without the formation of an intermediate resonant compound state. Energy is conserved by transferring back to the continuum the energy difference between the initial continuum state and the final state of well defined energy by means of a second particle, in the case of stripping or pickup reactions, or by means of a photon in the case of direct radiative capture. In either case these reactions have non-resonant excitation functions since the final continuum state can take whatever energy difference is available. Direct reactions are intrinsically simpler than resonant reactions which proceed in two steps, first forming a resonant compound state at a particular bombarding energy and then decaying to a final state. Consequently direct reactions can provde sensitive tests of certain features of nuclear states, in particular, those involving information about the single particle reduced widths or spectroscopic factors of the final states. When the final states are bound states it may be difficult to get the same information in other ways.

Compared to direct nuclear reactions such as stripping or pickup reactions which involve the strong and only partly understood nuclear force, direct radiative capture proceeds via the well understood and

much weaker electromagnetic interaction. It is, therefore, particularly amenable to calculation since the electromagnetic interaction can be treated accurately by first order perturbation theory. If accurate information about the continuum states is available from elastic scattering measurements then, with knowledge of the perturbation responsible for the interaction, the only unknown in the transition matrix element is the final state wavefunction. Direct radiative capture is then a sensitive method of probing final state wavefunctions. At low bombarding energies direct radiative capture may be dominated by extra nuclear effects and thus be relatively insensitive to the details of the interior region of the nucleus which is dominated by complex many-body interactions. In such cases direct radiative capture cross sections are relatively independent of the particular model used to describe the interior region of the nucleus and essentially depend only on the one parameter determining the amplitude of the single particle wavefunction at the nuclear surface. The objectives of the present work were to measure the cross section for the reaction $^{16}O(p, \gamma)^{17}F$, to compare the results with recent theoretical calculations in order to assess the adequacy of these assumptions about the direct capture process and then to extrapolate the cross section to stellar thermal energies where the reaction plays a role in the larger hydrogen burning stars.

Resonant radiative capture has been more extensively studied than has direct radiative capture. In the neighborhood of resonances it has, in general, a larger cross section and it gives rise to narrow peaks in excitation functions which clearly distinguish it from non-resonant

capture and background effects. The larger cross section for resonant radiative capture in the neighborhood of resonances can be understood in terms of a simple qualitative model. Resonant capture is characterized by

$$A + B \rightarrow C^* \rightarrow C + \gamma$$

where projectile A, having an energy at or near a resonance in the bombarding energy, is captured via the strong nuclear interaction by target nucleus B into a resonant excited state $C^*$ in the continuum of the compound nucleus C. It is then held there for several nuclear periods before it is either re-emitted (resonant scattering) or drops to a lower state of C via the electromagnetic interaction with the emission of a gamma ray (resonant capture). In contrast, for direct radiative capture, characterized by

$$A + B \rightarrow C + \gamma$$

the continuum state corresponds to potential scattering where those particles which come within the range of the nuclear force pass through the nuclear potential only once. The weak electromagnetic interaction has a much shorter time (the time for projectile A to go past the target nucleus B) to cause any of the incident particles to drop into final states of lower energy with the emission of a gamma ray. The final state in direct radiative capture can be either a bound state of C or a resonant state in the continuum of C with an energy lower than the initial continuum state. The energy dependence of the electromagnetic operators tends to favor the lower states, however other factors such as selection rules and the form of the radial matrix elements may favor higher ones.

Direct capture is most readily observed in energy regions away from compound resonances in the continuum where it is not in competition with resonant capture, however it can occur at any energy and in resonance regions it may appear as a smoothly varying background under a region dominated by resonances. The interference between resonant and direct capture has been observed for the $^{16}O(p, \gamma)^{17}F$ reaction by Domingo (1965) in the neighborhood of the 2.66 Mev resonance and recently Rolfs (1973) has studied direct capture contributions in resonance regions for the reactions $^{12}C(p, \gamma)^{13}N$ and $^{17}O(p, \gamma)^{18}F$.

The present work is concerned with measurements of the direct radiative capture of protons by $^{16}O$ in a region where there are no resonances. The elastic scattering of protons by $^{16}O$ has also been measured since the results are used in calculating the initial continuum wave functions for the direct capture matrix elements as well as providing a normalization for the direct capture experiment. These reactions are shown schematically in Fig. 1.1. The data appearing in the figure are those given by F. Ajzenberg-Selove (1971). The labeling of the gamma rays, shown in the figure, will be used throughout the following work.

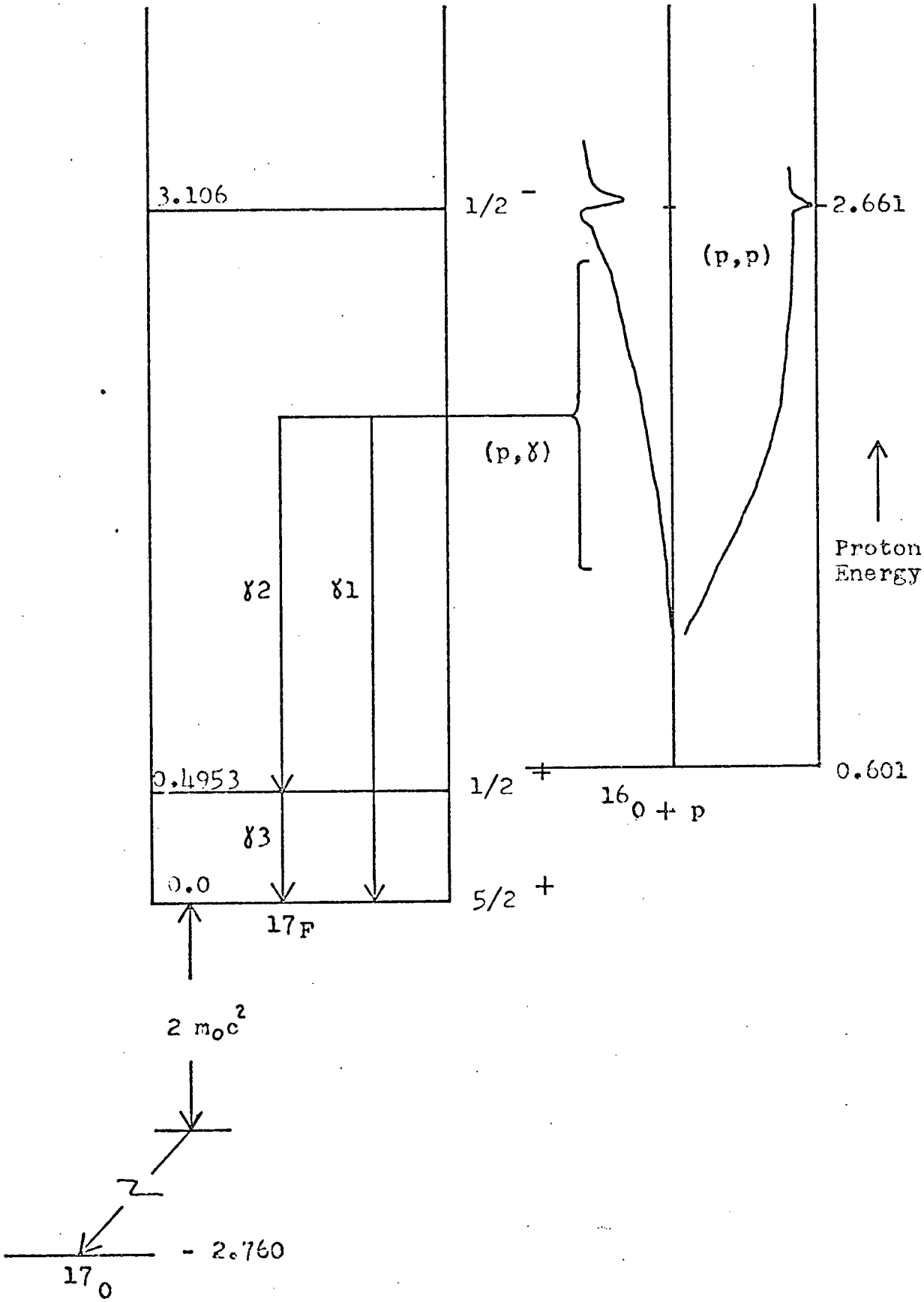


Figure 1.1 : $^{16}O(p,\gamma)^{17}F$ and $^{16}O(p,p)^{16}O$ reactions.

## 1.2 PREVIOUS MEASUREMENTS

Cross sections have been measured for the radiative capture of low energy protons (< 3 Mev) by many of the light nuclei. The capture of protons by deuterons has been investigated by Fowler, et. al. (1949) and later by Griffiths, et. al. (1962b) who found it to obey an $A + B \sin^2\theta$ angular distribution and to have an absolute cross section that increased smoothly with energy from 1 μbarn at 275 Kev to 3.5 μbarn at 985 Kev bombarding energy.

Studies of radiative proton capture have been made for $^{6}Li$ by Bashkin and Carlson (1955) and Warren, et. al. (1956), $^{7}Be$ by Kavanagh (1960), $^{9}Be$ by Meyerhof and Tanner (1959), $^{12}C$ by Woodbury, et. al. (1954), $^{13}C$ by Trost, et. al. (1964), and $^{14}N$ by Bailey and Hebbard (1963a and 1963b).

The $^{16}O(p, \gamma)^{17}F$ reaction was first studied experimentally by Du Bridge, et. al. (1938), who observed the 66.0 second positron decay of $^{17}F$ following the capture of 4 Mev protons. Curran and Strothers (1940) and Laubenstein et. al. (1951a) measured the relative capture cross section from 0.55 to 0.95 Mev and from 1.4 to 4.1 Mev respectively, also observing the $^{17}F$ positron decay. The individual gamma ray transitions were first observed by Warren et. al. (1954), who studied the relative yields from 0.8 to 2.1 Mev and measured an absolute cross section of 6 ± 3 μbarns for $\gamma 2$ at 1.35 Mev. Angular distribution data were also obtained, indicating that $\gamma 2$ followed a $\sin^2\Theta$ relation, whereas $\gamma 1$ and $\gamma 3$ were approximately isotropic. Further data on the gamma rays were obtained by Robertson (1957) and Riley (1958), who measured absolute cross sections from 0.583

to 2.02 Mev, and by Domingo (1965), who scanned the region around the 2.66 Mev, $\frac{1}{2}^-$ resonance in $^{17}F$. By observing the positron decay of $^{17}F$, absolute cross sections were extended to lower energies from 0.275 to 0.616 Mev by Tanner (1959) and from 0.140 to 0.170 Mev by Hester et. al. (1958).

Approximate theoretical calculations confirming the direct nature of the capture process were made by Griffiths (1958) and Nash (1959). Further direct capture calculations were made by Christy and Duck (1961), Lal (1961), and Griffiths et. al. (1962a). Donnelly (1967) extended the direct capture theory to include calculations using both a square-well plus coulomb potential (Model I) and a Saxon-Woods plus coulomb potential with a spin-orbit term included (Model II). Chow (1973) has refined these calculations still further.

The $^{16}O(p, p)^{16}O$ elastic scattering cross section was first measured by Laubenstein, et. al. (1951a, 1951b), who determined the excitation function from 0.6 to 4.5 Mev at 159°-169° and assigned angular momenta to the energy levels of $^{17}F$. Eppling (1952) and later Eppling, et. al. (1953) and Eppling, et. al. (1955) measured the elastic scattering from 0.28 to 4.6 Mev at eight angles from 90°.4 to 168° and performed a phase shift analysis of the data. However, the majority of their latter work remains unpublished. Henry, et. al. (1956) measured the cross section at four angles from 2.5 to 5.6 Mev.

## 1.3 ASTROPHYSICAL INTEREST

The $^{16}O(p, \gamma)^{17}F$ reaction is of particular interest because of its role in hydrogen burning stars. In the interiors of the hotter main sequence stars and in the shells of red giant stars where temperatures range from about 15 to 30 x $10^6$ °K, the primary source of energy production is from the burning of hydrogen through the CNO bi-cycle (Fig. 1.2). In this cycle the C, N and O nuclei serve as catalysts and the net effect, upon the completion of a cycle, is the conversion of four hydrogen nuclei into a helium nucleus with the release of 26.7 Mev of energy.

Relative abundances of C, N and O in these stars can be obtained by comparing the lifetimes of the individual nuclei for proton capture with the lifetime of the complete cycle (Caughlan and Fowler, 1962). The abundance of $^{16}O$ depends, among other things, on the branching ratio of the reaction $^{15}N(p, \alpha)^{12}C$ (which completes the main cycle) to the reaction $^{15}N(p, \gamma)^{16}O$ (which leaks nuclei from the main cycle to the oxygen side cycle). From a priori arguments of charged particle versus electromagnetic widths, Bethe (1939) originally estimated this branching ratio as $10^4$:1.

Hebbard (1960) showed however that the (p, $\alpha$) and (p, $\gamma$) cross sections at thermal energies were strongly affected by two interfering $1^-$ levels in $^{16}O$ at excitation energies of 338 and 1010 Kev. Using a two-level Breit-Wigner analysis of his (p, $\gamma$) data he showed that there was destructive interference in the region between these two levels. In addition, by a similar analysis of the existing (p, $\alpha$)

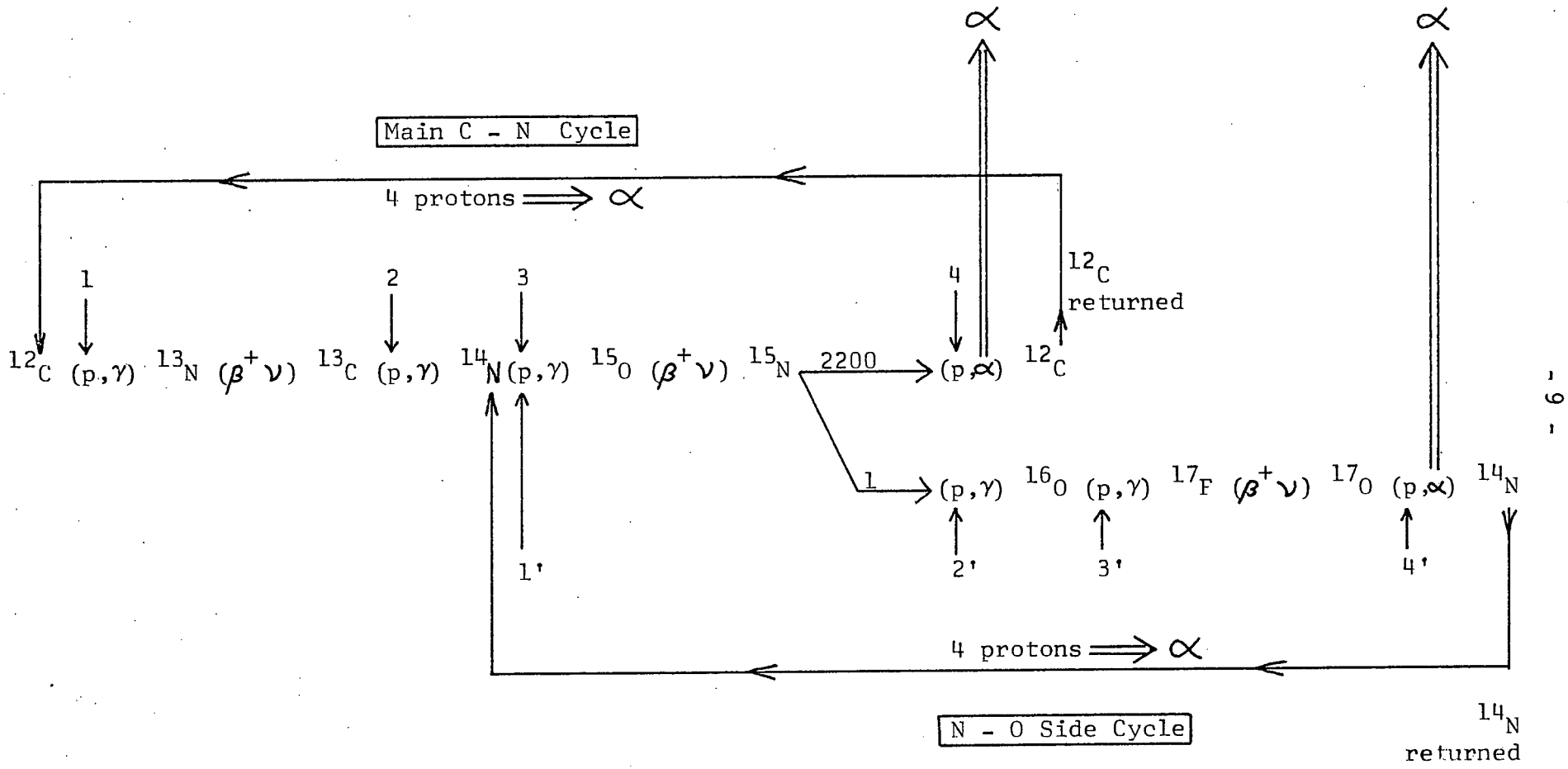


Figure 1.2 : The Carbon - Nitrogen - Oxygen (CNO) Bi-Cycle.

data, and using the same parameters, he showed the interference between the levels for the (p, $\alpha$) reaction to be constructive. Taking into account the change in phase of the 338 Kev resonance when moving from the energy region between the resonances to the region of thermal energies below the resonances the analysis predicts an enhancement at thermal energies of the (p, $\gamma$) cross section resulting from constructive interference between the contributions from the tails of the two $1^-$ levels and, a corresponding reduction of the (p, $\alpha$) cross section at thermal energies, relative to the values expected on the basis of single level properties of the 338 Kev state alone. Although this analysis did not consider possible direct capture contributions and may even contain an error (Vogt, 1973) the revised branching ratio of 2200:1 that it gives still suggests an increase in the significance of the oxygen side cycle.

## 1.4 THEORETICAL BACKGROUND

For the present work the direct capture calculation can be adequately treated in terms of a two-body model which reduces to a single particle model in the center of mass frame. Matrix elements of the electromagnetic operator are calculated for the transitions between states described by wavefunctions representing an initial continuum state of the equivalent single particle and a final bound state of the same particle, corresponding to the direct radiative capture of the particle.

At low bombarding energies, defined as energies where the De Broglie wavelength of the incoming particles is large compared to the nuclear radius, the initial continuum function is largely excluded from the interior of the nucleus as well as from the region of the nuclear surface by coulomb and centrifugal barriers. As a result the amplitude of the continuum function increases for some distance beyond the nuclear surface. On the other hand the final bound state function will be largely interior with a tail extending beyond the nuclear surface by an amount which increases with decreasing binding energy. Consequently the integrand of the radial overlap integral contributing to the transition matrix element will tend to have a maximum outside the nuclear surface, an effect that will be particularly true if the final state has a low binding energy. In this case the radial integral and corresponding matrix element will be relatively insensitive to the unknown interior parts of both initial and final state wave functions. For electric multipoles this effect is further enhanced by the $r^L$ dependence of the

electromagnetic 2L-pole operator. Chow (1973) has calculated the energy dependence of the percentage of interior contribution for some radial integrals. He estimates that at 1 Mev, for example, capture to the $\frac{1}{2}^+$ and $5/2^+$ states is about 97% and 88% extranuclear respectively.

These arguments suggest that the theoretical calculations used here, which introduce much simplified single particle wave functions for the interior wave functions, should give a good description of the direct capture cross section since the results are relatively insensitive to the particular assumptions about the interior region. The adequacy of the approximations can, of course, be tested only by a comparison between the theoretical and experimental cross sections.

Since the $^{17}F$ nucleus consists of a tightly bound $^{16}O$ core containing a doubly closed shell structure plus a loosely bound proton in both the ground and first excited states, it conforms to the conditions of the above theoretical model where the single odd proton (in the center of mass) moves in a potential provided by the $^{16}O$ core in both continuum and bound states. In order to generate the wave functions it is necessary to define the properties of this potential. It is interesting to note that the observed spin and parity of the ground state, $5/2^+$, and the first excited state, $\frac{1}{2}^+$, of $^{17}F$ are consistent with the single particle shell model assignments of $d_{5/2}{}^+$ and $s_{\frac{1}{2}}{}^+$. The bound state wave functions used to calculate the direct capture cross sections to these two final states were generated so as to be consistent with these angular momentum and parity assignments. In addition, the low binding energies of 0.601 Mev for the ground state and 0.106 Mev for the first excited state (equivalent

to the Q values for the direct radiative capture reaction), ensure that the direct capture should be significantly extranuclear.

Following is a brief outline of the direct capture calculation based on Chow (1973). The differential cross section for the direct radiative capture of a projectile A by a target nucleus B to form a final nucleus C, treating the electromagnetic interaction as a first order time dependent perturbation is given by

$$\frac{d\sigma}{d\Omega} = \frac{2\pi}{\hbar v} \frac{dn(E)}{d\Omega} \sum_{m,M,P} \frac{1}{(2I_1+1)(2I_a+1)} \left| \langle \Phi_M | H^P_{int} | \Phi_m \rangle \right|^2 \quad - 1.1$$

where $v$ = relative velocity of the incident projectile A

$I_1$, $I_2$ = spins of A and B respectively

$P$ = circular polarization of the photon ($P = \pm 1$)

$n(E)$ = density of final states in the radiation field

$|\Phi_m\rangle$ = initial continuum state with magnetic quantum number m

$|\Phi_M\rangle$ = final state with magnetic quantum number M

$H^P_{int}$ = the electromagnetic interaction hamiltonian.

The $^{16}O$ interaction is represented by a diffuse edged Saxon-Woods potential with a spin-orbit term of the Thomas form and a Coulomb potential corresponding to a uniformly charged sphere, and is given by

$$V(r) = V_{SW}(r) + V_{SO}(r) + V_{Coulomb}(r) \quad - 1.2$$

where $$V_{sw}(r) = -V_0 \left[ 1 + e^{\left(\frac{r-R}{a}\right)} \right]^{-1} \quad - 1.2a$$

$$V_{so}(r) = -V_s \left(\frac{\hbar}{m_\pi c}\right)^2 \times \frac{1}{r} \times \left| \frac{d}{dr} \left( \frac{V_{sw}(r)}{V_0} \right) \right| \vec{l} \cdot \vec{\sigma} \quad - 1.2b$$

$$V_{Coulomb}(r) = \begin{cases} \frac{Ze^2}{2R}\left(3 - r^2/R^2\right) & r \leq R \\ \frac{Ze^2}{r} & r > R \end{cases} \qquad - 1.2c$$

where R = nuclear radius parameter = $r_0 A^{1/3}$ with a = 16

a = diffuseness parameter

$V_0$ = central well depth

$V_s$ = spin-orbit well depth

$\vec{l} \cdot \vec{\sigma}$ = orbital and spin angular momentum respectively.

The central well depth, $V_0$, does not have to be energy independent. It is often assumed to vary linearly with energy and given the form

$$V_0 = V_1 + cE \qquad - 1.3$$

where $V_1$ = energy independent part of the potential

c = coefficient ascribed to the "effective mass" of the proton in the nucleus.

This choice of a potential gives five adjustable parameters R, a, $V_s$, $V_1$ and c. Chow (1973) carried out a potential well parameter search and found the set of parameter values which "best" described the $^{16}O$ + p interaction in the continuum and bound states of $^{17}F$ to be

R = $1.23 \times 16^{1/3}$ = 3.09 fm

a = 0.65 fm

$V_s$ = 5.0 Mev

$V_0$ = (55.29 - 0.67E) Mev.

The wave functions for direct capture are generated by solving the Schroedinger equation with this energy dependent potential for the continuum energies desired.

# CHAPTER 2

# TARGET FABRICATION

## 2.1 INTRODUCTION

The study of nuclear reaction probabilities is usually initiated by directing an accelerated beam of charged particles against stationary "target" nuclei. The construction of a target, with characteristics suitable for a particular experiment, is thus a very common experimental problem. In most cases the properties of the beam and target may affect the data collected so as to alter it from the idealized situation corresponding to individual nuclei interacting with each other.

The measurements made in this work gave rise to three different experimental situations, each imposing certain criteria for possible targets. These situations were:

a) Measurement of the $^{16}O(p, p)^{16}O$ cross section at the backward angle of 170°.9 for mean laboratory proton energies from 0.354 to 1.991 Mev.

b) Measurement of the $^{16}O(p, \gamma)^{17}F$ cross section at 90° for mean laboratory proton energies from 0.845 to 2.556 Mev.

c) Measurement of the $^{16}O(p, \gamma)^{17}F$ angular distribution for mean laboratory proton energies from 0.828 to 1.956 Mev.

The targets used for each of these cases is discussed below. The chapter concludes with a discussion of the method used to measure the target thicknesses.

## 2.2 TARGETS FOR ELASTIC SCATTERING

### 2.2a BASIC REQUIREMENTS

The $^{16}O(p, p)^{16}O$ scattering cross section was measured in this work primarily to provide a normalization for the $^{16}O(p, \gamma)^{17}F$ cross section measurements. If this normalization is to introduce no significant error in the final direct capture cross section, the elastic scattering cross section should be determined to $\leq \pm 1\%$. As discussed in Chapter 3, the scattering cross section was measured as a function of energy by pairs of runs that alternated between a progressively higher bombarding energy and a reference bombarding energy chosen low enough that only Rutherford scattering contributed.

The targets must be sufficiently stable under bombardment and uniform with respect to variations in size and location of the beam spot to allow the runs at higher energies to be normalized to the runs at the reference energy. The target must have a composition and a thickness that yields a scattering spectrum with an oxygen peak that is well enough resolved from all other peaks and high enough above its local background to allow an unambiguous determination of its area to $\leq \pm 1\%$. And the target must have a well defined thickness measureable to an accuracy that, in turn, allows an appropriately accurate determination of the mean proton energy at which the normalizing Rutherford cross section is to be calculated. At 0.400 Mev, the Rutherford cross section has an uncertainty of 1% for an error of 2 Kev in the beam energy. Finally, once a target meets these basic requirements, its parameters, particularly its thickness, should be adjusted to optimize other interrelated factors such as multiple scattering,

count rate, variation of reaction cross section with energy loss in the target, and signal-to-noise ratio versus peak separation in the scattering spectrum.

One candidate is a differentially pumped oxygen gas target. This, however, was not considered; partly because its large spatial extent leads to uncertainty in the definition of the reaction volume and partly because the general complexity of its operation is unattractive when compared to the simplicity of a solid oxide target.

The energetics of elastic scattering dictate that the target be composed only of oxygen together with either very light or very heavy nuclei if the oxygen peak is to be isolated in the scattering spectrum. The relative abundances of $^{17}O$ (0.037%) and $^{18}O$ (0.204%) to $^{16}O$ (99.759%) are small enough that the use of isotopically pure oxygen was considered unnecessary. The $^{18}O$ (p, p)$^{18}O$ scattering cross section is known well enough over the energies and angles of interest (Carlson, et. al., 1961) to enable sufficiently accurate corrections ($\leq$ 0.2%) to be made to the $^{16}O$ data at a few of the lower energy runs where the $^{18}O$ scattering was resonant and scattering from $^{18}O$ and $^{16}O$ was unresolved. Elastic scattering measurements for the even rarer $^{17}O$ (F. Ajzenberg-Selove, 1972) do not indicate resonances large enough for the presence of this isotope to introduce a significant error.

If one chooses an oxide of a heavy nucleus, then the energetics also dictate the necessity of a thin, transmission target that will eliminate the otherwise unacceptably high background under the oxygen peak which is caused by thick target scattering from the heavy nuclei present. Scattering observed from thick targets of iron, nickel, and molybdenum, which had been oxidized on the surface to FeO, NiO, and $MoO_2$ showed a poorly defined oxygen peak rising only a few percent above a large thick target background. The poor

signal-to-noise ratio, resulting from the much larger scattering cross section for the high Z nuclei in the metal substrate than for the oxygen nuclei in the oxide surface, indicates the difficulty inherent in using thick targets. In addition thick oxide layers made by oxidizing the surface layer of some thicker substrate tend to result in a diffuse oxygen distribution in the substrate and as a result do not exhibit a very well defined thickness. This is particularly true of oxide layers made by a heating process, although much less so for oxide films made by electrolytic anodization. The need for a definite target thickness suggests the attractiveness of a process such as evaporation or sputtering that uniformly "deposits" the oxygen or oxide onto an existing surface.

The foregoing considerations lead to the development and construction of transmission targets composed of self-supporting gold films onto which were deposited layers of tungsten tri-oxide ($WO_3$). The targets were mounted on copper washers, one inch in diameter, 1/32 inch thick, with a 3/8 inch diameter hole.

## 2.2b GOLD LAYER

The method used to make the self-supporting gold films was largely borrowed from techniques that have been developed for making carbon films. See, for instance, Kashay, et. al. (1959) and Dearnaley (1960). Gold was evaporated onto glass, removed intact from the glass, and mounted onto copper washers.

Self-supporting gold films could be made easily in the thickness range from 150 to 300 $\mu g/cm^2$ and with difficulty down to a lower limit of about 75 $\mu g/cm^2$. A thickness of 100 $\mu g/cm^2$ corresponds to $0.3 \times 10^{18}$ atoms/$cm^2$.

Gold is both a good electrical and thermal conductor. Its electrical conductivity prevents the targets breaking from electrostatic forces arising from static charges that would accumulate on non-conducting oxide films. However, its good thermal conductivity relative to $WO_3$ does not seem to ameliorate the problem of target heating since for all else constant, the thinner gold film usually makes a more durable target.

## 2.2c OXIDE LAYER

The oxygen content of the targets was supplied by subsequent deposition of $WO_3$ onto successfully prepared gold films by the method of cathodic sputtering. $WO_3$ was an attractive oxide to choose because of its high degree of oxidation, its stability (M.P. = 1473°C), and the high atomic weight of tungsten.

The subject of cathodic sputtering is described extensively in the literature. See, for instance, Holland (1963) for a useful and practically oriented discussion. As noted by Holland, it is usually difficult to determine accurately the sputtering rate for a particular system. In practice the thickness of the $WO_3$ layers was measured independently (section 2.4a), and knowledge of the sputtering rate was therefore needed only accurately enough to make targets within a desired thickness range. For consistent sets of sputtering parameters, the approximate rate was determined by trial and error. Unfortunately, it was not possible to determine thicknesses reliably by the simple method of weighing. Variation in deposition over the one inch diameter of the copper washers was too large. And attempts to use small test pieces of aluminum foil also failed because of different geometries and different holding properties for the

different receiving surfaces.

It was found that targets made with too slow a deposition rate were susceptible to contamination. This is not surprising in view of the high chemical activity of the tungsten and oxygen during deposition together with the extremely long total time (many hours) and the large residual pressure (5 to 10 x $10^{-3}$ torr) required for the process. In comparison, evaporations are characteristically done in seconds or minutes at pressures from $10^{-4}$ to $10^{-6}$ torr. On the other hand, the larger the current, the more susceptible the films were to breaking; probably due to heating or electrostatic effects. Conditions were therefore chosen to increase the deposition rate relative to the positive ion current as much as possible. As one step in this direction, the sputtering from the unused top surface of the cathode was quenched by placing a grounded plate above the cathode a distance away less than the cathode dark space. It was noted, but not understood, that when the time came to terminate the process, all of the targets shattered immediately unless the discharge was quenched by reducing the pressure before reducing the cathode voltage.

Representative sputtering parameters used for target preparation are listed below:

Cathode - 5 cm x 10 cm x 0.002 inch tungsten sheet

Cathode voltage - 2500 volts negative

Cathode to target distance - 5-6 cm

Positive ion current - 2-4 ma

Residual gas - 5-10μ of oxygen for which the mean free path of tungsten atoms is about 0.5-1.0 cm.

Effective Rate - 20 ma hours deposits approximately $10^{18}$ oxygen atoms/$cm^2$. Eight targets were sputtered at a time. The rate varied by ± 15% for targets in different locations. The breakage factor was about 50%.

Typical $WO_3$ layer - $60\mu g/cm^2 \simeq 0.5 \times 10^{18}$ oxygen atoms/$cm^2$ using the atomic stopping cross section data of Whaling (1962).

## 2.3 TARGETS FOR DIRECT CAPTURE

### 2.3a ABSOLUTE CROSS SECTION

As mentioned in Chapter 1, the direct capture excitation function was measured and normalized by observing the $^{16}O(p, p)^{16}O$ and $^{16}O(p, \gamma)^{17}F$ reactions simultaneously. Consequently, these targets must satisfy those requirements set forth in section 2.2a plus any additional requirements imposed by the direct capture reaction. This is difficult because for the direct capture, at the bombarding energies being considered, the photon yield is lower than that for elastic scattering by as much as seven orders of magnitude!

The further requirements are then those associated with measuring any low yield reaction; namely, collecting spectra with acceptable counting statistics and signal-to-noise ratios for the peaks of interest. The target must give rise to a low gamma ray background, withstand a high beam current, and contain enough oxygen in a layer that has the highest possible percentage of the beam energy loss arising from oxygen atoms rather than from other atoms. The beam spot on the target must also be small since the detector should be able to subtend as large a solid angle as possible without introducing uncertainties arising from large geometrical corrections.

The above criteria were met by a "thicker" version of the Au-$WO_3$ targets which were used for the scattering cross section measurements. Gold and tungsten both have low gamma ray background yields because their large Z effectively inhibits inelastic scattering and they can be obtained with high purity. As indicated earlier, $WO_3$ is one of the more stable oxides. $WO_3$ also compares satisfactorily with other oxides with regard to the

percentage beam energy loss attributed to oxygen, the triple oxide state compensating for the large Z of tungsten. From Whaling (1962), the energy loss is 48% due to oxygen in $WO_3$ for 0.8 Mev protons and 41% for 2.5 Mev protons. An oxygen gas target provides 100% of the beam energy loss in oxygen, but its large size makes it undesirable from the viewpoint of solid angle considerations.

The choice of an optimum oxide thickness involves a consideration of many factors. Below about 0.8 Mev the capture cross section becomes too small to measure with the experimental set-up used here. This lower limit on the beam energy considerably relaxes the maximum thicknesses of the gold and oxide layers that had previously been set for the elastic scattering targets by the 0.354 Mev monitor runs. Initially, then, the greater the oxide thickness, the higher the reaction yield and the better the signal-to-noise ratio in both the capture and scattering spectra. However, the thicker the oxide, the greater is the beam energy lost in it and the smaller the beam current that can be used. Therefore, for

$N_o$ = number of oxygen atoms/$cm^2$ of target

$N_p$ = number of incident protons/sec,

it is the total count rate, proportional to the product $N_o N_p$, rather than the reaction yield per incident proton, proportional to $N_o$, which should be maximized.

Since the energy of the direct capture gamma rays varies with the incident proton energy, the corresponding peaks in the gamma ray spectrum are broadened by the energy loss in the target. This introduces another factor into the choice of an optimum oxide thickness. The thickness can be increased until the energy loss in the oxide becomes greater than the

energy resolution of the gamma ray detecting system so that the peaks in the spectrum develop a flat top. Any further increase in the oxide layer will no longer improve the signal-to-noise ratio. Further increase will, however, continue to increase the total number of counts in the peaks and improve their counting statistics. But this latter improvement is accomplished at a risk. The broader the direct capture peak, the greater is the probability that it may contain an unresolved background peak. This problem is discussed in more detail in section 4.2.

These thicker targets were made similarly to the Au-$WO_3$ targets described in sections 2.2b and 2.2c. Oxide layers were used that were between 15 to 30 Kev thick to whatever beam energy was being used. Again from Whaling (1962), this gives oxide thicknesses of

0.35 to 0.70 x $10^{18}$ oxygen atoms/$cm^2$ at 0.8 Mev beam energy

0.66 to 1.32 x $10^{18}$ " " at 2.5 " " " .

The targets could withstand beam currents from two to four μamps for several hours with less than 25% loss in their oxygen content. Such target deterioration did not, however, affect the accuracy of the cross section measurements. With the method of normalization being used, both the direct capture yield and the scattering yield were affected similarly by any target deterioration or non-uniformity that occurred since both systems were observing the same beam-target interaction at each instant of time. In fact, data for a single capture cross section measurement could be, and in some cases were, collected using more than one target. The maximum current which could be used was very dependent upon the focus condition of the beam spot, two to four μamps being possible with a beam spot of about 1/8 to 3/16 inches in diameter. For each target there seemed to be a rather definite

upper limit in the current above which the target would break almost immediately. After bombardment, the targets were usually torn or cracked in one way or another.

## 2.3b ANGULAR DISTRIBUTION

The targets used for these measurements consisted of a tantalum sheet whose front surface had been electrolytically anodized to form $Ta_2O_5$. Anodization probably produces oxide films of better defined thickness than any other method except the deposition techniques discussed earlier, and certainly more uniform than heating methods. The bottom surface of an oxide layer formed by anodization will still have a somewhat diffuse junction with the underlying substrate, with the oxygen content not falling abruptly to zero at a certain depth. On the other hand, these anodized $Ta_2O_5$ films are probably more uniform in thickness than $WO_3$ layers laid down by sputtering when a large enough surface area is considered.

Targets were made by anodizing one inch by six inch sheets of highly polished tantalum to either 250 or 300 volts and positioning them at 45° with respect to the beam direction. For a ratio of 10-25 Å/volt (Young, 1961) between oxide thickness and anodization voltage, this gives a $Ta_2O_5$ layer about 400 $\mu g/cm^2$ thick. There is a maximum voltage (about 300-400 volts for tantalum) above which dielectric breakdown starts to occur and further film growth is not possible (Young, 1972), A better indication of film thickness, and of the oxygen content versus film depth, was obtained by analysing the shape of the direct capture peaks produced by these targets with corrections made for detector system resolution.

Two thicknesses of tantalum were tried; 0.005 inches and 0.0005 inches.

After being anodized, a tantalum sheet was screwed to a 1/32 inch thick copper backing whose surface had been coated with Dow Corning # 340 Silicone Heat Sink Compound. Although the thinner sheet had less of the poorly conducting tantalum between the copper and the beam spot, it tended to wrinkle from the heat deposited by the beam and separate from the copper. Heat dissipation was usually achieved better with the thicker, more rigid, tantalum sheets. For a beam spot between 1/8 and 3/16 inches in diameter and optimum running conditions the targets could withstand up to 9 μa at 2.0 Mev and 6 μa at 2.5 Mev for a few hours. Whenever it was felt that the oxygen content had diminished by too much, it was a simple matter to slide the target up or down and shift the beam spot to a new location. One target could provide twenty or more beam spot locations without any overlapping.

## 2.4 THICKNESS MEASUREMENTS

### 2.4a TRANSMISSION TARGETS

The measurement of an absolute cross section depends upon an accurate measurement of the beam energy loss in the target so that the average reaction energy can be deduced from a knowledge of the bombarding beam energy. The sensitivity of the different absolute cross sections measured, to changes in energy, are shown in Table 2.1 as a function of bombarding energy. For each energy the uncertainty in energy which would contribute a 1% error in the corresponding cross section is shown, based on the cross sections measured in this work. With the experimental methods adopted here, only a determination of the energy loss in the targets is required, and not the more difficult measurement of their exact oxygen content.

The energy loss in the transmission targets was determined in terms of the measured energy loss suffered by incident alpha particles emitted from an $^{241}Am$ $\alpha$ source. Since the targets were used with their gold layer facing the beam, thicknesses were measured independently for the gold layer and for the oxide layer (i.e. total thickness minus thickness of gold). The $\alpha$ decay scheme of $^{241}Am$, showing only the four transitions that are strong enough to be seen in the spectra taken, is shown in Fig. 2.1. The energy shown for the most intense $\alpha$ transition, $\alpha 3$, is that of Leang (1962). The values shown for the gamma ray transitions between levels of $^{237}Np$, which are used to determine the energy differences of the observed $\alpha$ transitions are from Lederer, et. al. (1967).

The following sources of error, associated with the evacuated chamber housing the $\alpha$-source, the target and the detector, were considered:

| C. M. Reaction Energy (Mev) | Change in Energy (in kev) needed to change Cross Section by 1 % | | |
|---|---|---|---|
| | $^{16}O(p,\gamma)^{17}F$ Differential Cross Section at 90° | | $^{16}O(p,p)^{16}O$ Differential Cross Section at 170°.9 |
| | $\gamma_1$ | $\gamma_2$ | |
| 0.300 | - | - | 1.5 |
| 0.400 | - | - | 2.0 |
| 0.800 | 2.2 | 2.2 | 6.7 |
| 1.500 | 6.2 | 7.9 | 32.3 |
| 2.500 | 14.9 | 17.6 | 53.8 |

Table 2.1 : Sensitivities of reaction cross sections with respect to energy.

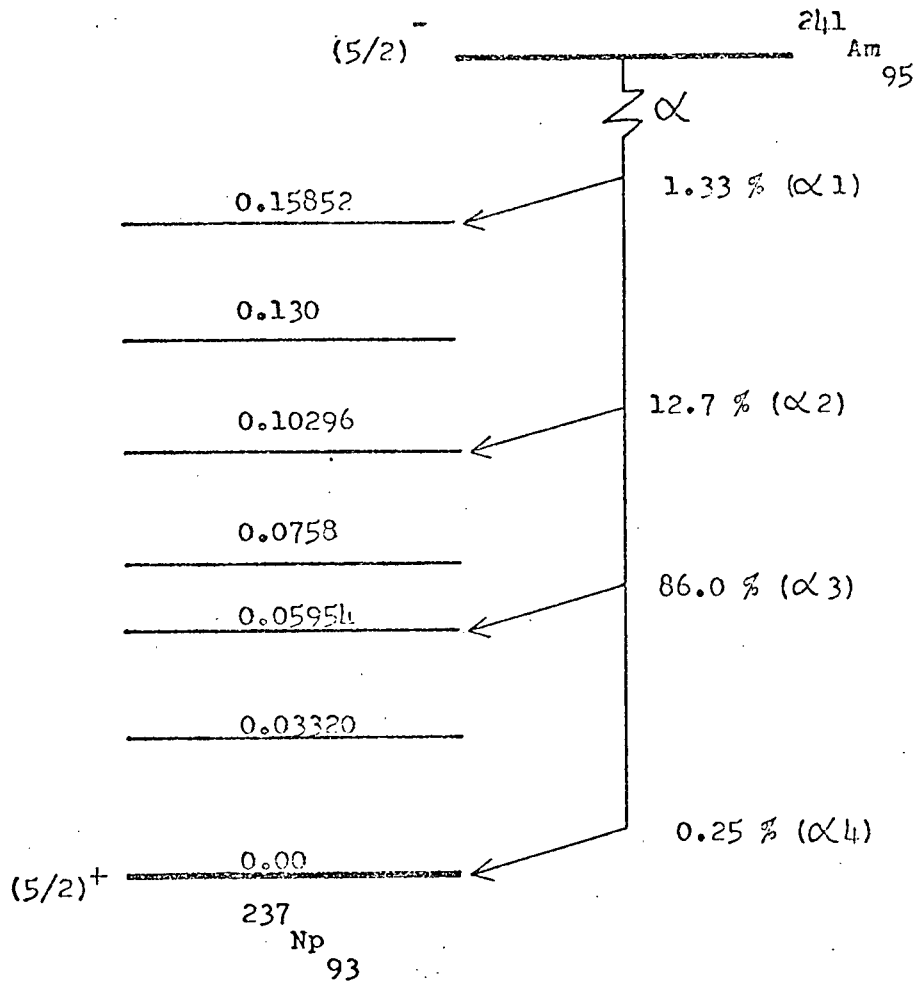


$E_{\alpha 3}$ = 5.4860 ± 0.0009 Mev

$E_{\alpha 1 - \alpha 2}$ = 55.56 Kev

$E_{\alpha 2 - \alpha 3}$ = 43.42 Kev

$E_{\alpha 3 - \alpha 4}$ = 59.54 Kev

Figure 2.1 : $\alpha$ - decay of $^{241}_{95}Am$ .

1) The target is normal to the α source to within ± 5°. Therefore, the thickness measured is the normal thickness to within < ½%.

2) Due to the size, closeness, and non-collimation of the α source, α particles can traverse the target up to 10° from the normal and still be counted in the detector. This would have the effect of skewing the α peaks to the low energy side, and those α particles traversing by 10° from the normal would record a thickness 1.5% greater than the normal thickness. However, most of the α particles will traverse the target much nearer the normal than 10°, and no such skewing of the peaks was seen. This error was estimated to be < ½%.

3) Spectra were taken with a chamber pressure less than 20μ. The energy of the α particles emitted by the source was consequently degraded by < 0.07 Kev.

Therefore, the thicknesses measured are the normal thicknesses to < ½%.

The shift in the channel position of α3 in the multichannel analyser was measured for the cases of no target between the source and detector and with a target inserted. This shift was converted to "energy loss for 5.486 Mev α particles" using the system gain established by the known energy differences of the four α transitions. A pulse generator peak was included in both spectra to monitor gain stability. A pair of such spectra is shown in Fig. 2.2. The use of this method relies upon having a detector system with energy resolution that is good enough to resolve the individual α transitions in order to use them for a reliable determination of the system gain. Peak positions were determined to approximately ± 0.2 channels for a gain of about 2 Kev/channel. For the targets used, the measurement of

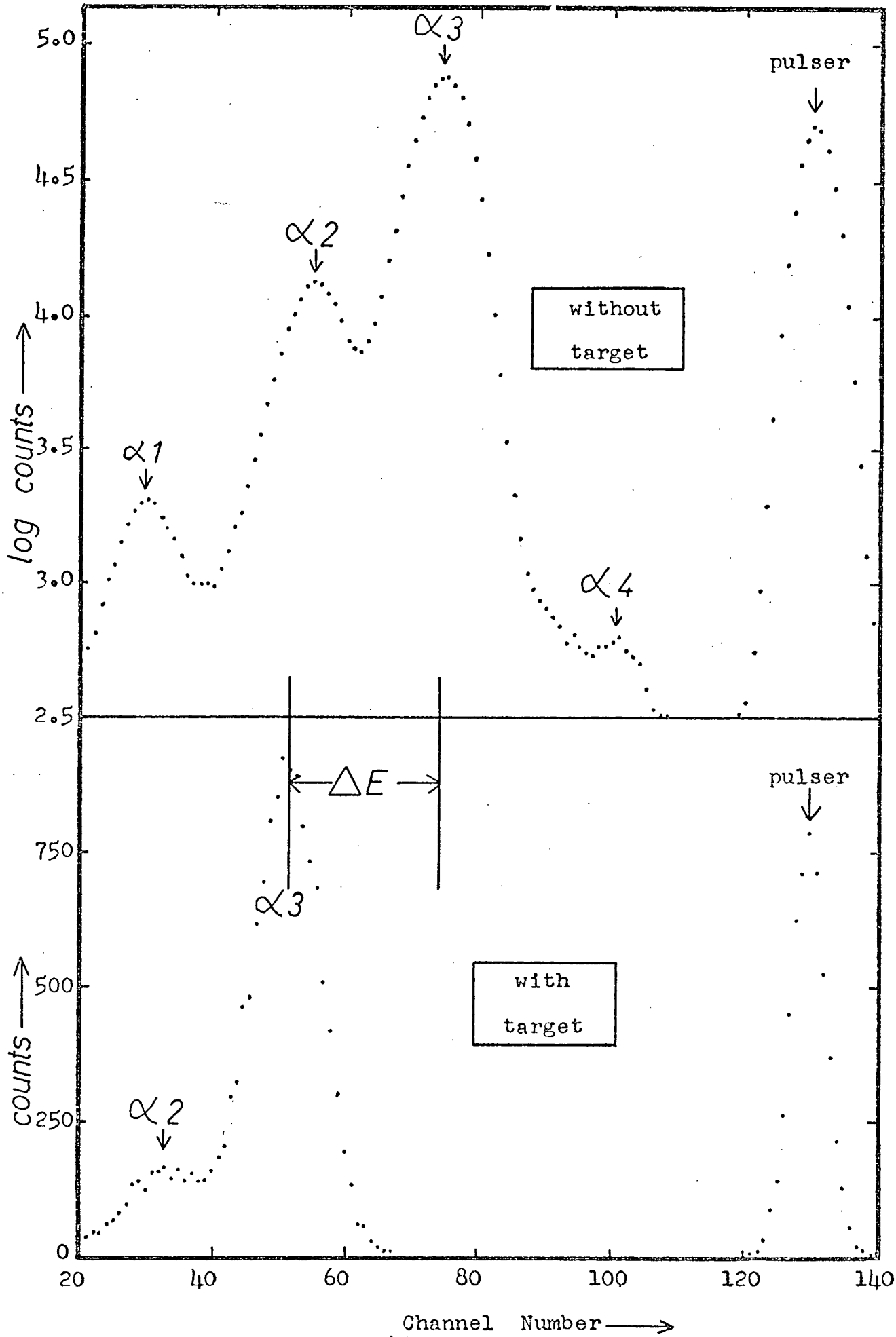


Figure 2.2 : Pair of $^{241}Am$ alpha spectra.

the energy loss by $\alpha 3$ could be made to about ±3% for the oxide layer. Target uniformity was checked for some of the targets by measuring their thickness in three places; the center and either side near the outer edge. The thicknesses of the gold layers were found to be uniform to within 1 Kev for $\alpha 3$. The oxide layers were non-uniform to about 2 ±1% of their total thickness. The thicknesses of the two targets eventually used for the runs that determined the $^{16}O(p, p)^{16}O$ excitation function were remeasured after being used. Their thicknesses had not measurably changed.

Atomic stopping cross sections of Whaling (1962) and Northcliffe and Schilling (1970) were used to convert energy loss for 5.486 Mev $\alpha$ particles to energy loss for protons in the energy range from 0.354 Mev to 2.556 Mev. The energy of $\alpha 3$ is large enough that variations in its charge state due to the capture and loss of electrons while traversing the target material were unimportant, and the energy loss relation for heavy ions,

$$(dE/dx)_{A,\ Z,\ E} = Z^2\ (dE/dx)_{A=1,\ E/A}$$

where dE/dx is the stopping cross section and A, Z and E are the atomic mass, charge and energy of the incident ion, should be valid. Specifically this becomes $(dE/dx)_{5.486\ \text{Mev}\ \alpha\text{'s}} = 4\ (dE/dx)_{1.372\ \text{Mev protons}}$. A comparison of the stopping cross sections of Whaling for 1.372 Mev protons in gold and in $WO_3$ with those of Northcliffe and Schilling for 5.486 $\alpha$ particles confirms the correctness of this relation to within 1%.

The actual degree of oxidation, $WO_x$, could be determined from the final scattering data. The oxygen content of a given target was obtained from a knowledge of the scattering yield, the scattering cross section and the

detector solid angle (eqn. 3.1). Comparing this measured oxygen content with the measured energy loss, the effective degree of oxidation necessary to give the observed energy loss with the available number of oxygen atoms/$cm^2$ could be determined. Such a calculation for the two targets used gave $x \simeq 2.2 \pm 0.1$. Therefore, the oxide layer, hitherto assumed to be $WO_3$, was most likely a combination of the possible oxides of tungsten. However, whatever the actual state of oxidation was, it does not modify significantly the original assessments that lead to the choice of "$WO_3$" as the target material. Since it does not affect the cross section measurements, for simplicity, $WO_3$ will continue to be assumed.

The final uncertainty in the thickness of the transmission targets, arising from measurement of their thickness described above, was approximately ± 5 to 6% for the gold layer and ± 7% for the oxide layer. For the direct capture cross section measurements, the reaction energy was also determined by an independent method using the energy scale of the direct capture spectra and the energetics of the $^{16}O(p, \gamma)^{17}F$ reaction (section 4.2). In all cases the error in the cross section due to the uncertainty in the reaction energy was less than errors from other considerations.

## 2.4b ANODIZED TARGETS

Several methods exist for measuring the thickness of a surface oxide film. Some of these include measuring the film's capacitance, weighing before and after formation, and various optical methods (Young, 1961). In the final analysis, the reaction energies of the direct capture angular distribution measurements were obtained from the energy calibration of the

gamma ray spectra and the reaction energetics (section 4.2). Any information still needed about the target thickness was then inferred from this and a knowledge of the beam energy.

However, it was still useful to have an initial idea of the oxide thicknesses accruing while anodizing the tantalum sheets in the first place. Originally it was thought that satisfactory transmission targets could be made from self-supporting $Ta_2O_5$ films. Following the method of Aladjem and Brandon (1969), an attempt was made to electrochemically etch the underlying tantalum substrate from the $Ta_2O_5$ layer. This method never produced useable transmission targets. There always remained a small residue of "islands" of tantalum that became electrically isolated on the non-conducting $Ta_2O_5$ film in the final stages of the etching process. The scattering background under the oxygen peak produced by the residual tantalum was less for these targets than for thick target blanks, but was not as low as for the Au-$WO_3$ targets.

As a by-product of this work, the thickness of the anodized oxide films versus anodization voltage was found, by the $\alpha$ particle energy loss method described above, to be $0.58 \times 10^{18}$ oxygen atoms/cm$^2$ per 100 volts.

# CHAPTER 3

# EXPERIMENTAL METHODS

## 3.1 $^{16}O(p, p)^{16}O$

### 3.1a PROCEDURE

The $^{16}O(p, p)^{16}O$ differential elastic scattering cross section was measured at a backward scattering angle for incident protons from 0.4056 Mev, an energy low enough that the scattering was totally Rutherford scattering, up to about 2.0 Mev. The excitation function obtained was normalized to the classical Rutherford cross section at the lower energy. With a fixed charged particle detector, placed at 170°.9, measurements were made at each of 15 bombarding energies from 0.5053 to 2.000 Mev. Interleaved with these measurements were eight measurements at the reference energy of 0.4056 Mev. To determine if the scattering at this reference energy was pure Rutherford scattering, a similar series of runs was made to see if the observed yield in the region of the reference energy was proportional to the inverse square of the energy which should be the case for pure Rutherford scattering. This series consisted of measurements at bombarding energies of 0.3750, 0.4250 and 0.4500 Mev interspersed with three measurements at 0.4055 Mev.

The observed yield at an energy, E, for any of the above measurements can be expressed as

$$N_c = N_p N_o \left(\frac{d\sigma}{d\Omega}\right)_{(E,\theta)} d\Omega \qquad -3.1$$

where $N_c$ = number of counts per sec.

$N_p$ = number of incident protons per sec.

$N_o$ = number of oxygen atoms/$cm^2$ of target

$\left(\frac{d\sigma}{d\Omega}\right)_{(E,\theta)}$ = differential cross section in $cm^2$/ster for scattering at energy, E, into angle, $\theta$

$d\Omega$ = solid angle in steradians subtended by the detector.

Comparing the count rate observed at an energy, E, with the count rate observed at the reference energy, $E_R$, it follows that

$$\left(\frac{d\sigma}{d\Omega}\right)_{(E,\theta)} = \frac{N_p(E_R)}{N_p(E)} \times \frac{N_c(E)}{N_c(E_R)} \times \left(\frac{d\sigma}{d\Omega}\right)_{(E_R,\theta)} = \frac{N_p(E_R)}{N_p(E)} \times \frac{N_c(E)}{N_c(E_R)} \times \left(\frac{d\sigma(Rutherford)}{d\Omega}\right)_{(E_R,\theta)} \quad -3.2$$

to the extent that $N_p$ and $N_o$ are common to both measurements and the scattering at ($E_R$, $\theta$) is totally Rutherford. The frequent runs made at the reference energy provided an accurate check on the stability of the oxygen content of the target.

The protons for this experiment were provided by the U.B.C. 3 Mev Van de Graaff generator. The proton beam energy was calibrated by using the known energies of the many resonances of the $^{27}Al(p, \gamma)^{28}Si$ reaction which are distributed throughout the energy region studied (Appendix A). The oxygen targets consisted of gold-tungsten oxide transmission targets described in Chapter 2. Each series of measurements was made using a single target; the differential cross section series at higher energies with target #16 and the series to check the Rutherford scattering at the reference energy with target #17. The measured thicknesses for these targets was:

| TARGET | TARGET THICKNESS | |
|---|---|---|
| | Gold (atoms/$cm^2$) | Oxide ($WO_3$ molecules/$cm^2$) |
| # 16 | $0.470 \pm 0.026 \times 10^{18}$ | $0.162 \pm 0.011 \times 10^{18}$ |
| # 17 | $0.473 \pm 0.026 \times 10^{18}$ | $0.152 \pm 0.011 \times 10^{18}$ |

Care was needed in measuring the scattering spectra at the lower energies in order to ensure that the oxygen peak had a sufficiently good signal-to-noise ratio and was sufficiently well resolved from the long, low energy tail of the very much larger Au-W peak. Target thicknesses were chosen to optimize these conditions. The targets were positioned with their gold layer facing the beam. A backward scattering angle was chosen to maximize the energy separation of the peaks while minimizing the sensitivity of the cross section to the value of the angle.

### 3.1b SCATTERING CHAMBER

The scattering was observed in a 23 5/8 inch diameter x 15 inch high aluminium scattering chamber (Fig. 3.1). This chamber was originally assembled and alligned by Mint (1970). The angular scale of the externally rotatable assembly that carried the detector was calibrated just prior to this work. This was done by rotating the detector, with its collimator in place, toward 180° and noting the angle reading at which it intersected the beam axis as defined by a laser beam which was positioned to pass through the beam collimators and the small pin hole of a rear port allignment flange. For this setting the angular scale read 179°.1 ± 0°.1.

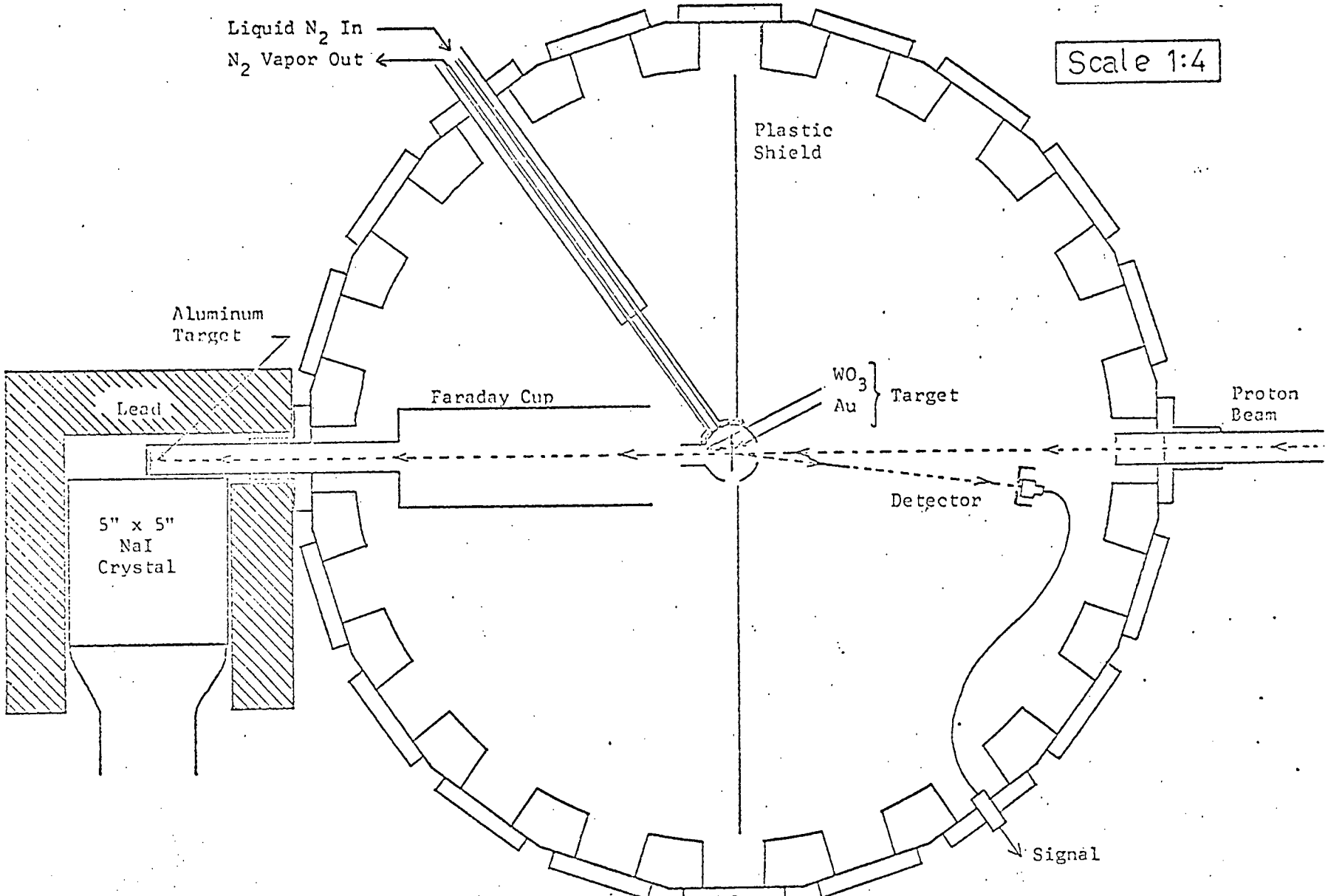


FIGURE 3.1: $^{16}O(p,p)^{16}O$ Scattering Chamber.

This calibration was confirmed by similar checks at 90° using the two 90° ports.

The interior of the chamber was bisected at 90° to the beam axis with a plastic shield to reduce background scattering. The prolific scattering within the chamber probably originated from small angle forward scattering of the beam as a result of passing through the relatively thick target. The effect would have been enhanced at the low energies and by the absence of a skimmer associated with the detector collimator. Neglecting multiple scattering, the calculated Rutherford scattering into all angles $\geq \theta$ would have been 25% for $\theta = 5°$ for the runs at the reference energy. Omitting the plastic shield increased the background under the oxygen peak by almost a factor of ten at the lower energies.

Scattering spectra taken with the target exposed to the inside of the chamber had sizeable background peaks interfering with the oxygen peak. Subsequent investigation showed these to be due to carbon build-up in approximately equal amounts on the front and rear surfaces of the target. This was deduced by observing the scattering from targets of gold only (Fig. 3.2). Two peaks of approximately equal size could be seen, separated in energy by the energy loss in gold, and with energies corresponding to scattering from carbon. The intensity of the peaks grew approximately linearly with bombarding time and showed an energy dependence consistent with $^{12}C(p, p)^{12}C$ scattering.

The source of such carbon contamination is generally attributed to the residual hydrocarbon molecules present in the vacuum system from the oil of the diffusion pump. As these molecules randomly collide with the target, which has become heated by the beam, they are "cracked" and

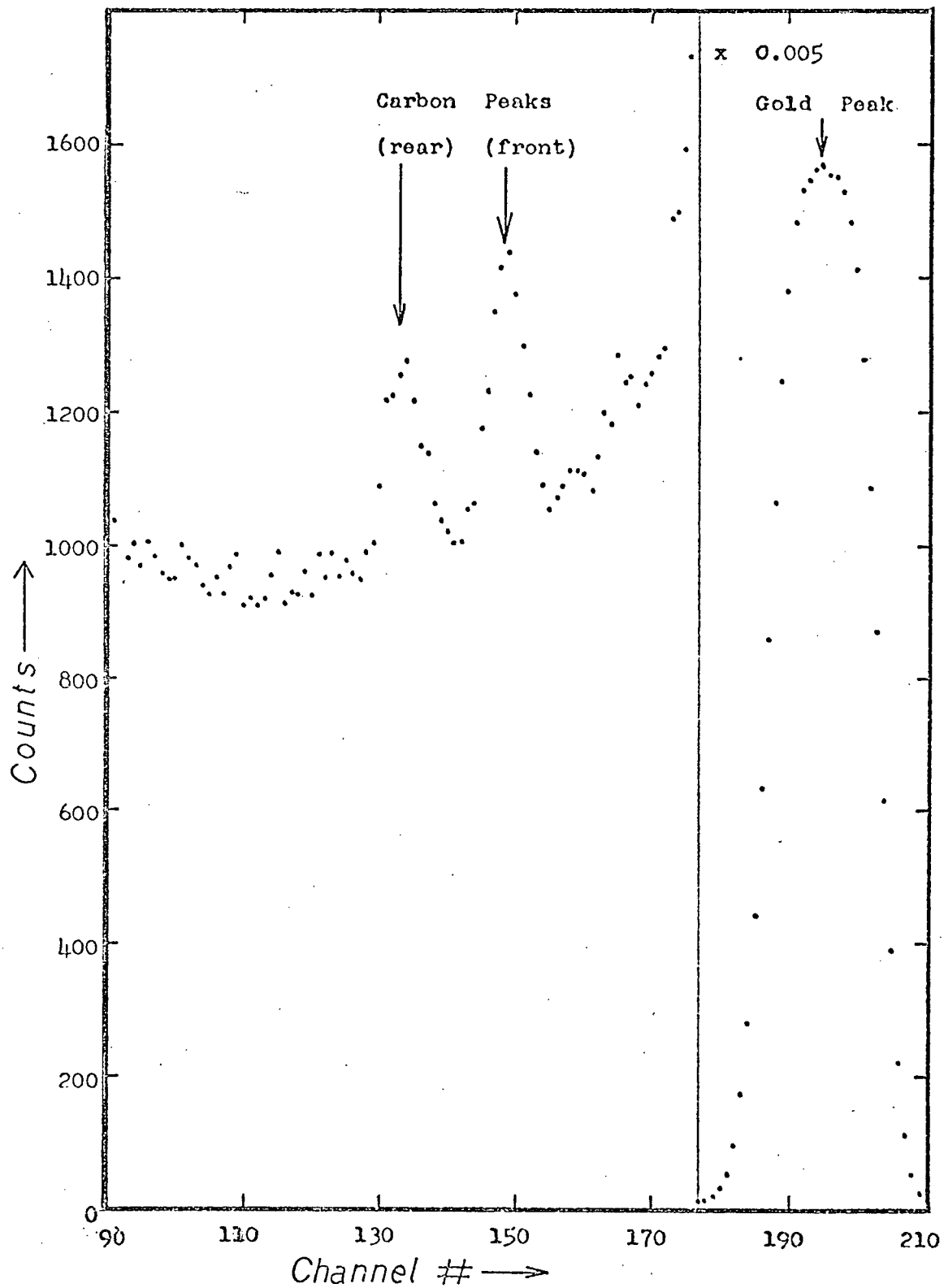


Figure 3.2 : Carbon build-up on gold target.

deposit carbon atoms. However, from the equal build-up on both sides of the target, it must be concluded that the generally accepted explanation that the beam "drags" the residual molecules into the target by colliding with them and imparting to them a preferential motion toward the target is minimal here.

By surrounding the target with a liquid nitrogen cooled cylindrical sleeve, the carbon contamination was reduced by almost a factor of ten. Fig. 3.3 shows scattering spectra taken under similar bombarding conditions with and without this cold sleeve. The sleeve was constructed from a copper cylinder 1 3/4 inch O.D. x 1/16 inch wall x 7 3/4 inch long with holes of 5/8 inch, 5/8 inch, and 7/16 inch diameter placed at 180°, 0°, and 90° to allow entrance and exit of the beam and observation of the target area respectively. The liquid nitrogen flowed by gravity, from a suspended reservoir, down and through a side port of the chamber at 53°, circulated through copper coils soldered to the sleeve, and finally exited by the same port. The sleeve and port assembly were mounted rigidly to the chamber and insulated electrically and thermally from it by lucite and teflon. The back pressure was regulated so that the nitrogen had become a vapor by the time it was expelled. The following pressures were representative of the chamber.

1) $5 \times 10^{-7}$ torr - chamber isolated from beam line and sleeve at room temperature.

2) $1.5 \times 10^{-7}$ torr - chamber isolated from beam line and sleeve cooled with liquid nitrogen.

3) $2 \times 10^{-7}$ torr - system pressure with incident beam.

Although the total chamber pressure is not reduced much by cooling the sleeve, the marked decrease in carbon build-up reflects a much larger drop

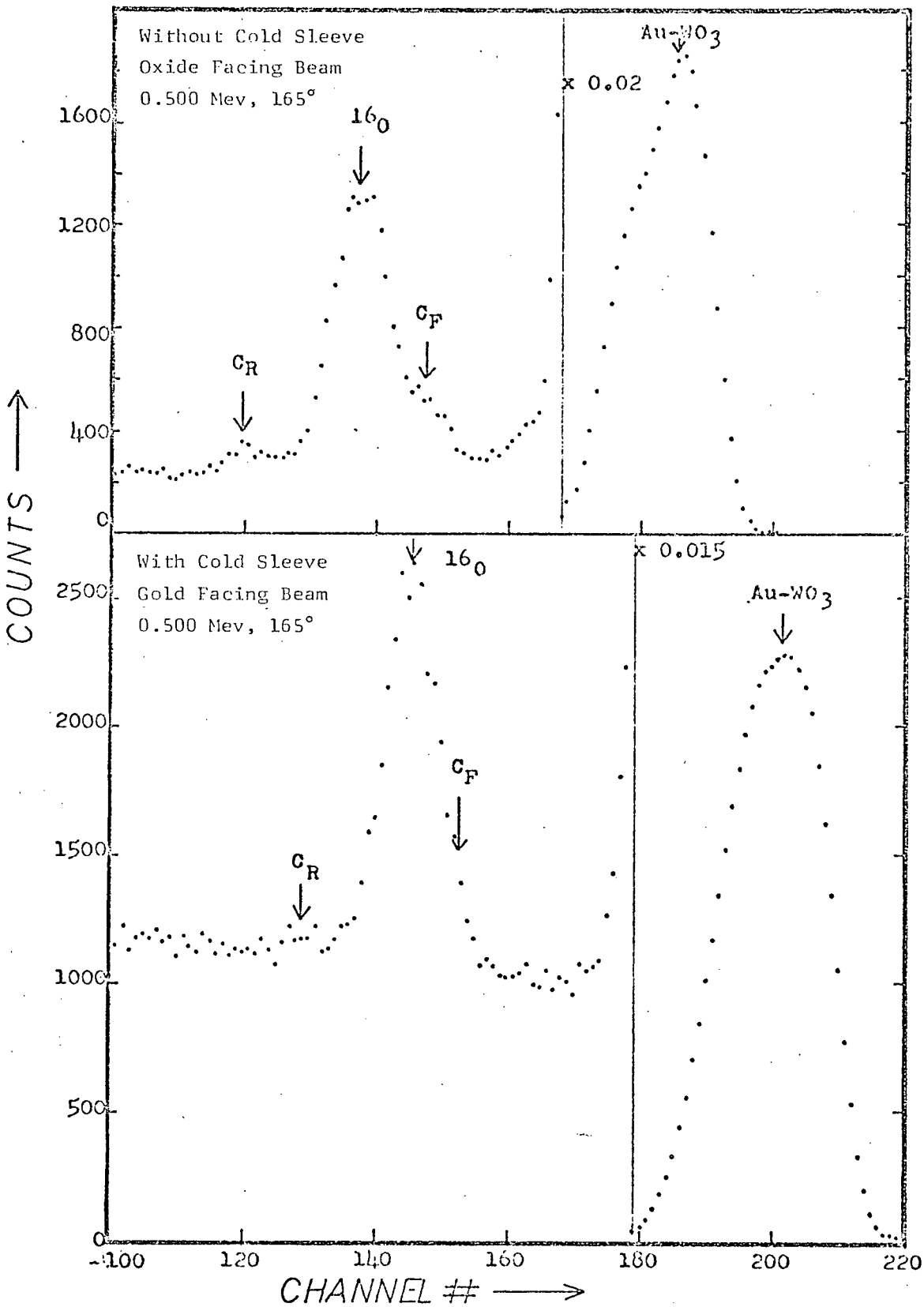


Figure 3.3 : $^{16}O(p,p)^{16}O$ with and without cold sleeve.

in the partial pressure of condensable hydrocarbon vapors in the vicinity of the target.

The target assembly could accommodate four targets and a viewing quartz. The assembly was moveable in the vertical direction and was electrically insulated from ground. Using the two 90° ports, the targets could be positioned normal to the beam to within ± 1°. One of the target positions was left empty to allow the beam to be directed against the aluminum target, located in the Faraday cup, so that scattering runs and beam energy calibration runs could be made alternately (Appendix A). The incident protons were collimated into a cone of half angle ≃ 0°.4. This confined the beam to a 1/16 inch spot on the target and defined it well enough to prevent a significant amount of scattering out of the 3/8 inch diameter region of the target which was located 12 inches from the final beam skimmer. The detector was positioned at an angle of 170°.9 ± 0°2 and collimated with a 0.226 ± 0.001 inch diameter circular collimator whose front surface was 9.00 ± 0.05 inches from the target. The mean scattering angle was therefore defined to ± 0°.5 and the direction of all protons seen by the detector was defined to within ± ≃0°.8.

The target region was electrically biased as shown schematically in Fig. 3.4. The target and Faraday cup were biased positively to suppress secondary electron emission. The cold sleeve, which completely surrounded the target except for small entrance and exit holes to allow passage of the beam, served as a Faraday cup for protons scattered by more than 10° and was therefore included in the charge integration circuit. Note, however, that the cold sleeve was insulated from ground and not biased.

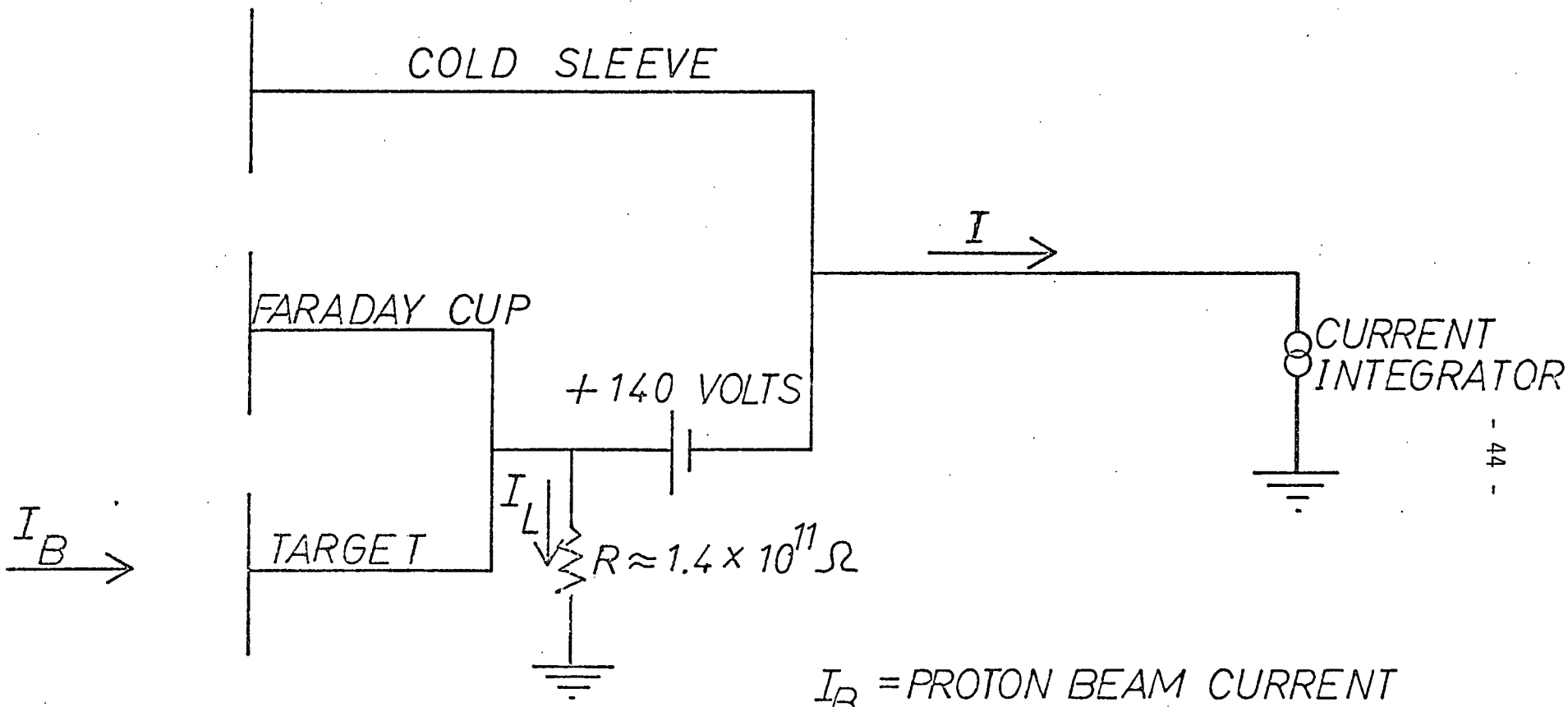


$I_B$ = PROTON BEAM CURRENT

$I_L$ = PROTON LEAKAGE CURRENT

$I = I_B - I_L$ = INPUT CURRENT TO CURRENT INTEGRATOR

FIGURE 3.4 : $^{16}O(p,p)^{16}O$ TARGET BIASING (SCHEMATIC).

Although liquid nitrogen by itself, and the sleeve by itself at room temperature are each good insulators, the combination of a biased cold sleeve with liquid nitrogen flowing between it and ground had a resistance of around $10^9\Omega$. For the bias of + 140 volts, this gave a leakage current of 100-200 namps which was larger than the beam current itself. In addition, this current fluctuated widely. However with the cold sleeve not biased, the leakage was reduced to around 1 namp. It was measured before and after each run to ± 0.05 namps. The integrated current was measured by an Ortec # 439 Digital Current Integrator having a rated accuracy of o.1% and reproducibility of 0.01%.

Since the individual scattering measurements were normalized to each other for the same number of incident protons, a measurement was needed only of the relative integrated charge between runs. This measurement is much less susceptible to error than is a measurement of the absolute integrated charge, but it still has uncertainties associated with it. The absolute calibration must be stable over all runs and it is possible for the actual current collected with a given target geometry and bias circuit to change as a function of bombarding energy and quality of target surface. Extensive tests to determine the exact uncertainty in the integrated charge were not made. However, it was estimated that the error in the measurement of the relative charge was less than ± 1% and would not contribute an additional significant error to the final yield measurements.

### 3.1c ELECTRONICS

The detection and pulse height analysis of the scattered protons was made with the electronics shown in the block diagram Fig. 3.5. The

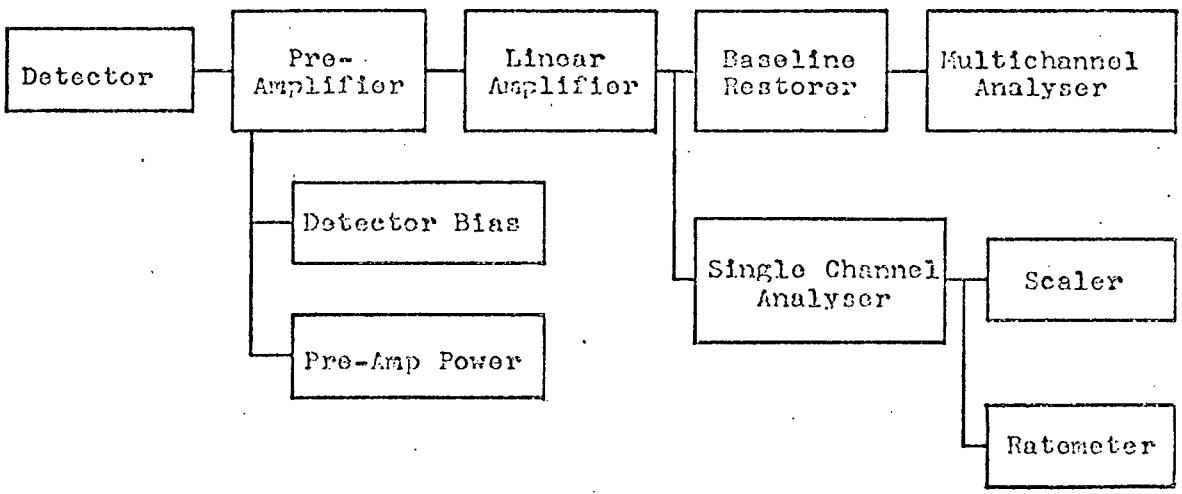


Pre-Amplifier ---------- Ortec 109A

Detector Bias ---------- Ortec 210

Pre-Amp Power ---------- Ortec 115

Linear Amplifier --------- Ortec 440A

Baseline Restorer -------- Ortec 438

Multichannel Analyser ---- Kicksort Inc. 705/706 (4096 channels)

Single Channel Analyser -- Ortec 406A

Scaler ------------------- Canberra Industries 1470

Ratemeter ---------------- Ortec 441

Figure 3.5 : $^{16}O(p,p)^{16}O$ electronics.

detector used was an Ortec silicon surface barrier detector for charged particles (model #A-016-050-100, serial #9-134C) with

active area - > 50 $mm^2$

depletion depth - > 100 microns.

For an operating bias of +55 volts it had a leakage current of less than 0.2 μa and an energy resolution of 18 Kev FWHM for 5.486 Mev α particles. The integrated beam current was recorded with an Ortec 439 Current Digitizer, with an accuracy of 0.01% or 0.1% depending upon the sensitivity setting.

The electronics was a basic nuclear spectroscopy system with some special attention given to minimizing high count rate distortion effects. In particular, since an accurate measurement of the absolute cross section was required, it was necessary to minimize and monitor the number of proton-oxygen scattering events removed from the oxygen peak due to counting rate effects. These effects include:

1) Pulse pile-up in the linear amplifier.

2) Pulse summing in the analyser (two pulses arriving within the "input gate open" time interval).

3) Analyser dead time.

To the slight detriment of the energy resolution, the shaping time constant of the linear amplifier was set at its minimum value of 0.25 μsec. The unipolar pulse used, as observed at the output of the Baseline Restorer, returned to the D.C. baseline level within 1.4 μsec. The input gate of the analyser was set at its minimum value of 2.0 μsec. Count rate distortion also depended upon further details of the analyser, which had the facility to reject low level pulses with a sensitivity control, reject

low and high level pulses with a single channel analyser window, and adjust the channel position of the spectrum. Using a pair of Datapulse (model 101) pulse generators, the actual time it took the analyser to perform each of these relevant functions was determined. And an investigation of scattering spectra taken for a variety of running conditions and analyser settings showed that for spectra similarly positioned within a fixed number of channels and with similar portions of their counts rejected rather than analysed, the per cent loss from counts removed from the oxygen peak (or any peak) varied linearly with the total count rate (as it should theoretically).

All scattering data were obtained from 256 channel spectra that were collected with the low energy end and the gold-tungsten peak rejected by the analyser, and with the oxygen peak roughly centered in the middle channels. This set of conditions gave a loss of

$$0.61\% \pm 0.05\% \text{ per } 1000 \text{ total counts/sec.}$$

All spectra were taken with a count rate of approximately 3000 counts/sec., as monitored by the ratemeter. The exact rate for each run was recorded with the scaler. It was later realized that count rate losses could be treated in a simpler, more direct way. The simpler method was used for the direct capture measurements and will be discussed there.

The data was released by dumping the analyser memory onto paper tape which was punched with a Teletype high speed (up to 110 lines per sec.) tape punch (model BRPEII). The paper tape was converted by an optical reader to magnetic tape which was subsequently read by a computer program and converted to printed, plotted, and/or card output for further analysis.

## 3.2 $^{16}O(p, \gamma)^{17}F$

### 3.2a PROCEDURE

The differential cross section at 90° for the $\gamma 1$ and $\gamma 2$ transitions following the direct capture of protons by $^{16}O$ was measured at seven laboratory energies from 0.845 to 2.556 Mev. Two of the energies were chosen close enough together to serve as a reproducibility check. The data were normalized by simultaneously observing the elastically scattered protons whose cross section had been previously measured over this energy range. Angular distribution data were taken at three angles at 0.828 Mev laboratory energy and at four angles at each of the laboratory energies 1.370, 1.956 and 2.452 Mev. For each energy, the runs at different angles were normalized to each other using the isotropy of the 0.495 Mev $S_{1/2}^{+} \rightarrow d_{5/2}^{+}$ $\gamma 3$ transition. Background runs made on gold targets showed a clean spectrum in the energy region of the $\gamma 3$ line.

For the absolute cross section measurements, the yields for the (p, $\gamma$) and (p, p) reactions can be expressed as

$$(p,\gamma): \quad N_{c\gamma} = N_{p\gamma}\, N_{o\gamma} \left(\frac{d\sigma}{d\Omega}\right)_{(E,\,\theta_\gamma)} (d\Omega\, \epsilon\, T)_\gamma \qquad -3.3a$$

$$(p,p): \quad N_{cp} = N_{pp}\, N_{op} \left(\frac{d\sigma}{d\Omega}\right)_{(E,\,\theta_p)} d\Omega_p \qquad -3.3b$$

where $\gamma$, p denote the direct capture and scattering spectra respectively

$N_{c\gamma}$, $N_{cp}$ = number of counts

$N_{p\gamma}$, $N_{pp}$ = number of incident protons

$N_{o\gamma}$, $N_{op}$ = number of oxygen nuclei/cm$^2$ of target

$\left(\frac{d\sigma}{d\Omega}\right)_{(E,\theta_\gamma)}$ , $\left(\frac{d\sigma}{d\Omega}\right)_{(E,\theta_p)}$ = differential cross sections

$(d\Omega\ \varepsilon\ T)_\gamma$ , $d\Omega_p$ = detector responses.

Since both reaction yields arise from one and the same source,

$$N_{p\gamma} = N_{pp} \qquad \text{and} \qquad N_{O\gamma} = N_{Op}$$

Therefore,

$$\left(\frac{d\sigma}{d\Omega}\right)_{(E,\theta_\gamma)} = \frac{N_{c\gamma}\ d\Omega_p}{N_{cp}\ (d\Omega\ \varepsilon\ T)_\gamma} \times \left(\frac{d\sigma}{d\Omega}\right)_{(E,\theta_p)} \qquad - 3.4$$

where $\left(\frac{d\sigma}{d\Omega}\right)_{(E,\theta_p)}$ is measured independently

$d\Omega_p$ can be determined by direct geometrical measurement

$(d\Omega\ \varepsilon\ T)_\gamma$ can be determined (Appendix B)

$N_{c\gamma}$ , $N_{cp}$ are determined by analysis of the respective spectra.

Once again a normalization proceedure has been devised which avoids having to measure the absolute oxygen content of the target. Even though the scattering and capture cross sections depend quite differently on the energy, for the target thicknesses used the measurements are independent of non-uniformity, deterioration and even replacement of the target. They are also independent of flucuations and uncertainties of the beam current or integrated charge.

For the angular distribution measurements, the yields at a given energy, E, and a given angle, $\theta_1$, can be expressed as

$$(N_c)_{\gamma i} = N_p\, N_o \left(\frac{d\sigma}{d\Omega}\right)_{(E,\theta_1)_{\gamma i}} (d\Omega\ \varepsilon\ T)_{\gamma i,\theta_1} \qquad - 3.5a$$

$$(N_c)_{\gamma 3} = N_p\, N_o \left(\frac{d\sigma}{d\Omega}\right)_{(E,\theta_1)_{\gamma 3}} (d\Omega\ \varepsilon\ T)_{\gamma 3,\theta_1} \qquad - 3.5b$$

where $\gamma i = \gamma 1$ or $\gamma 2$

$N_p$ , $N_o$ , as indicated, are the same for both cases.

Dividing gives

$$\frac{\left(\frac{d\sigma}{d\Omega}\right)_{(E,\theta_1)\gamma i}}{\left(\frac{d\sigma}{d\Omega}\right)_{(E,\theta_1)\gamma 3}} = \frac{(N_c)_{\gamma i}\ (d\Omega\,\epsilon T)_{\gamma 3,\theta_1}}{(N_c)_{\gamma 3}\ (d\Omega\,\epsilon T)_{\gamma i,\theta_1}} = K(\theta_1) \qquad -3.6$$

where $K(\theta_1)$ can be determined by evaluation of the detector responses (Appendix B) and analysis of the peak intensities in the energy spectrum. At the same energy but a different angle, $\theta_2$ ,

$$\left(\frac{d\sigma}{d\Omega}\right)_{(E,\theta_1)\gamma 3} = \left(\frac{d\sigma}{d\Omega}\right)_{(E,\theta_2)\gamma 3} \qquad -3.7$$

since $\gamma 3$ is isotropic. Therefore, from eqns. 3.6 and 3.7,

$$\frac{\left(\frac{d\sigma}{d\Omega}\right)_{(E,\theta_1)\gamma i}}{\left(\frac{d\sigma}{d\Omega}\right)_{(E,\theta_2)\gamma i}} = \frac{K(\theta_1)}{K(\theta_2)} \qquad -3.8$$

In this way, the ratios of the cross sections for $\gamma 1$ and $\gamma 2$ to $\gamma 3$ can be compared to each other at different angles to give the angular distribution.

## 3.2b REACTION CHAMBER

The $^{16}O(p, \gamma)^{17}F$ differential cross section at 90° was measured with the Au-$WO_3$ transmission targets and the gamma ray angular distributions were measured with the $Ta_2O_5$ targets that have been described in Chapter 2.

The reaction was measured in a chamber (Fig. 3.6) constructed for

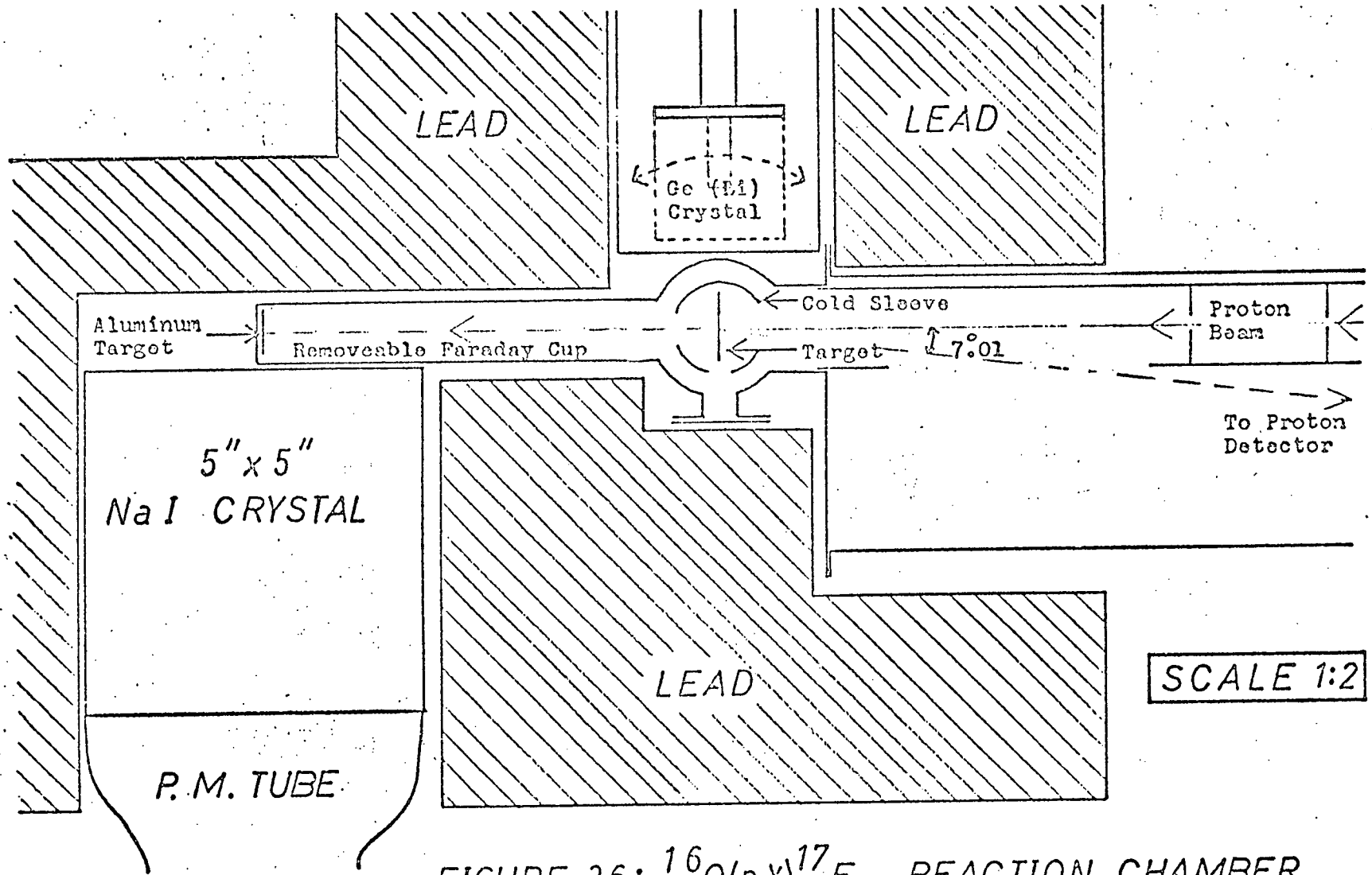


FIGURE 3.6: $^{16}O(p,\gamma)^{17}F$ REACTION CHAMBER.

this experiment. The chamber was mounted on the center-post of a 46 inch diameter heavy duty angular distribution table (originally built as a gun carriage) and positioned with the axis of its target assembly parallel with the axis of the angular distribution table. An adjustable supporting structure was built on the table to house the gamma ray detector and its 200-300 pounds of lead shielding. Using a laser to define the beam direction, the angular distribution table was positioned with its axis coincident with the point of intersection of the beam and target to within 1 mm. Using the laser as an optical lever, the cryostat which encloses the Ge(Li) crystal (Appendix B) was leveled with respect to the beam direction to within $<<1°$. The detector angle could be set to $\pm\frac{1}{2}°$.

The target assembly could accommodate either the 1 x 6 x 1/32 inch copper blank (holding a $Ta_2O_5$ sheet - Section 2.3b) or a 1 x 6 x ¼ inch aluminum bar with holes and insets machined to hold up to five 1 inch diameter copper washers (holding the Au-$WO_3$ films). The aluminum bar could also hold the 1 inch diameter discs containing the calibrated gamma sources which were used to measure the Ge(Li) detector response (Appendix B). In fact, the 1 inch diameter dimension was chosen for the copper washer mount to allow this direct substitution. For beam calibration, one target space was left empty to allow the beam to be directed against the aluminum target located in the Faraday cup. Finally, the aluminum bar was enclosed in a 0.005 inch tantalum cover fitted with 7/16 inch diameter holes placed concentrically with the 3/8 inch diameter transmission target regions. The water cooled target assembly could be moved vertically and could be rotated at an angle with respect to the

beam direction to an accuracy of ± 2 or 3°. The beam spot on the target could be observed via a viewing quartz.

Because of the very low yield of the direct capture cross section, one of the principle constraints on the chamber design was that it allowed close positioning of the Ge(Li) detector to the target. There were, however, considerations other than yield which limited the closeness to which the detector could be brought. First, was the 1 inch diameter of the calibrated gamma source discs. Second, was the decision to include a liquid nitrogen cooled cylindrical sleeve as was done for the $^{16}O(p, p)^{16}O$ measurements. Since the lowest energy used was 0.845 Mev (rather than 0.375 Mev) the interference of the carbon and oxygen peaks in the scattering spectra used for normalization was less of a problem. In retrospect it is still debatable whether including the cold sleeve was worthwhile. Third, and perhaps most fundamental, was the precision to which the locations of the calibrated gamma sources and the "integrated history" of the beam spot on the target could be assumed to be the same. This problem is discussed in Chapter 4. The closer the detector, the greater the precision required for a given error in the calibration and, therefore, in the normalization of the cross section data. A final consideration, namely the correction for the finite solid angle subtended by the Ge(Li) detector (Appendix B), did not turn out to be a limiting factor in choosing the target to detector distance. This was partly because the correction was determined accurately by experiment, but more because of the relatively smooth nature of the angular distributions. The extended Faraday cup which allowed the beam to be dumped in a place that could be shielded from the Ge(Li) detector during the excitation runs

at 90°, served no purpose when the $Ta_2O_5$ targets were being used. It could be removed and replaced by a flange to allow angular distribution measurements at forward angles. Distortion of the angular distribution due to uneven gamma ray absorption in the flange at different angles was resolved by measuring separate detector effeciency functions for each geometry used (Appendix B).

The design of the beam collimator system involved a compromise similar to the choice of the target to detector distance. The larger the beam spot, the larger the current that the targets could withstand, with a correspondingly higher count rate. On the other hand, the less sharply collimated the beam spot, the larger the geometrical error inherent in the calibration of the Ge(Li) detector. Two collimators were used, both 1/8 inch in diameter, and 22 inches apart; the last one was followed 2 inches further by a 3/16 inch diameter skimmer located 7 inches from the target.

The chamber also had to allow for the observation of the scattered protons at a backward angle near 170°.9 for comparison with the scattering data at this angle. For a circular collimator of given thickness, the ratio of the solid angle for scattering "off the collimator edge into the detector" to the solid angle for "unobstructed passage into the detector" increases as the collimator diameter decreases and the energy resolution and signal-to-noise ratio suffer accordingly. Therefore the proton detector had to be far enough away such that for a reasonable size collimator, the solid angle subtended would be small enough to keep the count rate to a manageable level. The proton detector was positioned with:

| | |
|---|---|
| Scattering angle, $\Theta$ | $173°.0 \pm 0°.4$ |
| Collimator dimensions - diameter, d | $2.383 \pm 0.002$ mm |
| - thickness, t | $0.190 \pm 0.015$ mm |
| Distance from target, D | $568.7 \pm 0.4$ mm |

For this position, scattered protons were observed at an angle $\simeq 2°$ different than the angle used for measurement of the scattering cross section. This necessitated a small correction (p. 82).

The following precautions were taken to minimize background gamma radiation. All internal surfaces of the chamber that were exposed to scattering from the beam were lined with 0.005 inches of tantalum. The inner surface of the cold sleeve was electroplated with 87 mg/cm$^2$ of gold, more than enough to stop 2.5 Mev protons. This was done rather than using a similar lining of tantalum sheet in order to maintain a good thermal contact between the cooled copper sleeve and the surface exposed to the target. The Ge(Li) detector was shielded in all directions as well as possible with lead blocks to an over-all thickness of about four inches. This reduced the room background to about 5% of its level for no shielding. To reduce the neutron flux from (d, n) reactions which will inevitably occur to some extent in the 90° magnet of the Van de Graaff accelerator a 16 inch thick barrier of concrete blocks was built between the magnet box and the chamber region.

For bombarding energies below about 1.5 Mev, the room background was the major contributor and $4\pi$ detector shielding was used which enclosed the detector and the target area together. This room background was the limiting factor in extending the measurements to lower energies. Even if enough running time had been available to overcome the diminishing cross section, with the beam current and the target oxygen content available

under the circumstances, the reaction count rate would have been low enough relative to the room background that the poor quality of the spectra with respect to signal-to-noise ratio would not have justified the effort. For higher bombarding energies the beam dependent background from the target area became dominant over background from external sources (room dependent plus beam dependent) and better signal-to-noise ratios were obtained with $2\pi$ detector shielding.

The most intense peaks in the room background spectrum were the annihilation radiation and 1.460 Mev peaks from $^{40}K$. The peaks of the RdTh spectrum were also visible. Otherwise the background spectrum was continuous. Bombarding energies had to be choosen to avoid overlap between the background peaks and the capture peaks. In fact, the lower bombarding energies were chosen to utilize the low background region between the full energy peak and the compton edge of the 1.460 Mev line.

### 3.2c ELECTRONICS

A block diagram of the electronics used in the (p, p) and (p, $\gamma$) spectrometer systems is shown in Fig. 3.7. As before, high count rate distortion was dealt with by using short amplifier time constants. The Nuclear Data multichannel analyser was not equipped with a simple single channel analyser window at its input as was the Kicksort analyser. Rejection of the low energy region and the gold-tungsten peak in the scattering spectra was done by running the analyser in its coincidence mode as shown and the single channel analyser following the delayed output of the Selective Active Filter amplifier was set to reject the portions of the spectra that were not to be analysed.

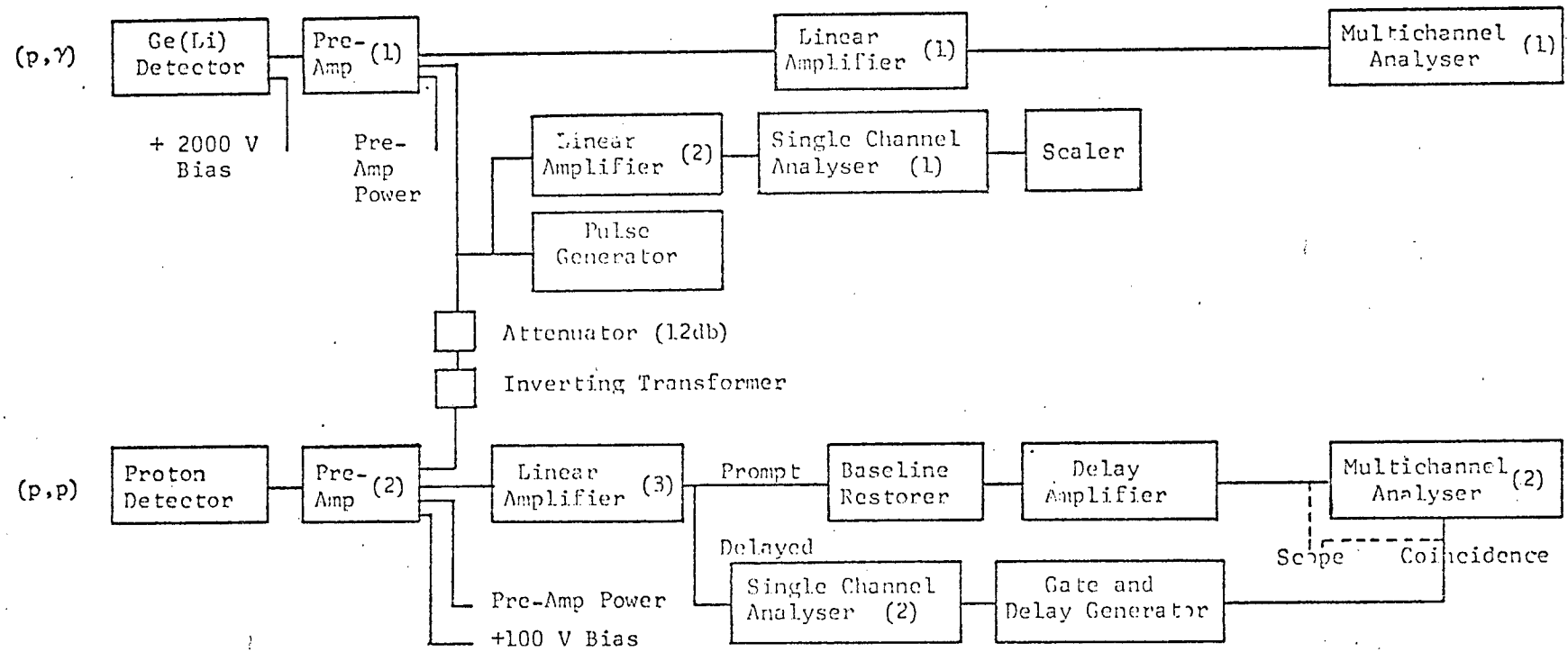


Pre-Amp - (1) ---------- Nuclear Diodes, Inc.
- (2) ---------- Ortec 109A
Linear Amplifier - (1) - Tennelec TC203BLR
- (2) - Ortec 485
- (3) - Ortec 440A
Pulse Generator -------- Ortec 448
Baseline Restorer ------ Ortec 438

Delay Amplifier ---------- Ortec 427
Single Channel Analyser - (1)- Ortec 406A
- (2)- Ortec 406A
Gate and Delay Generator ----- Ortec 416
Multichannel Analyser --- (1)- Kicksort 705/706
--- (2)- Nuclear Data 160
Scaler ---------- Canberra 1470

Figure 3.7 : $^{16}O(p,\gamma)^{17}F$ electronics for (p,γ) and (p,p) systems.

Scattering spectra were again collected in 256 channels. An approximate energy calibration could be made by running the analyser in its free mode for a short while, taking separate calibration spectra that included the gold-tungsten peak as well. Such spectra were useful when checking for contributions due to possible contaminants. Sample scattering spectra are shown for 0.845 Mev (Fig. 3.8) and 2.556 Mev (Fig. 3.9).

Gamma ray data was collected in spectra of either 1024 or 2048 channels and covering a range to include the $\gamma 1$ and $\gamma 3$ peaks. The gain was always roughly 1 Kev/channel. Accurate energy calibration spectra were taken before and after each direct capture run using several gamma sources of known energies. Some sample direct capture spectra are shown in Figs. 3.10 and 3.11. Note in Fig. 3.10, showing the angular distribution spectrum taken at the lowest bombarding energy, that $\gamma 1$ is only detectable above background because of its favorable location between the full energy peak and compton edge of the 1.460 Mev line. As it is, it was interfered with by two background peaks from the $^{18}O(p, \gamma)^{19}F$ reaction. In the spectrum for the absolute cross section measurement at a similarly low bombarding energy, but made with a smaller beam current, $\gamma 1$ was not visible at all and $\gamma 2$, even after 40 hours of running, had $< 10^4$ counts and was only about 50% above the background level. Consequently, runs at even lower energies were not taken.

For these spectra count rate losses were monitored using the Ortec pulse generator connected to the test inputs of the pre-amplifiers and to a scaler as shown in Fig. 3.7. The percentage removal of counts from

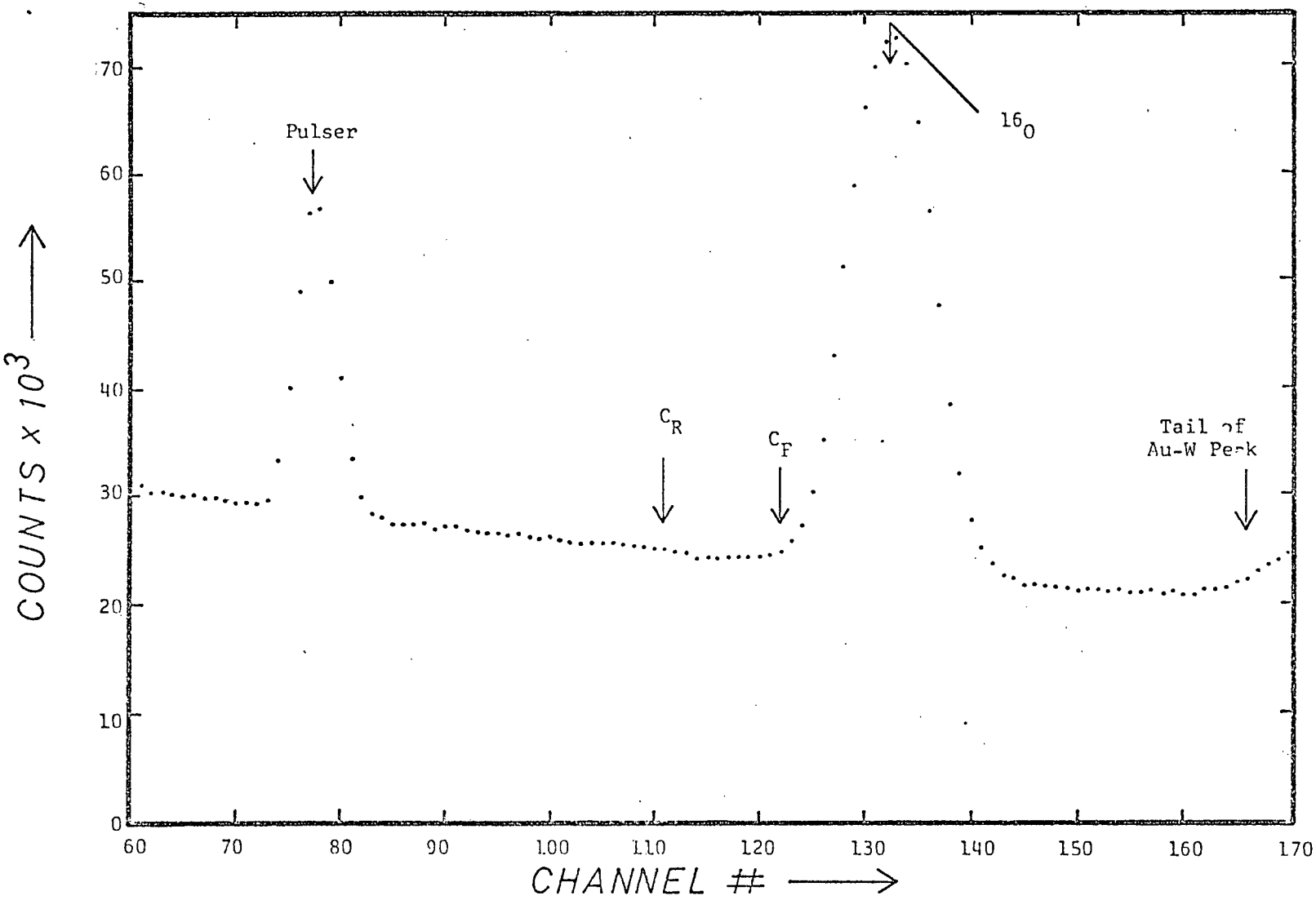


Figure 3.8 : $^{16}O(p,\gamma)^{17}F$ - associated scattering spectrum at 0.845 Mev proton energy.

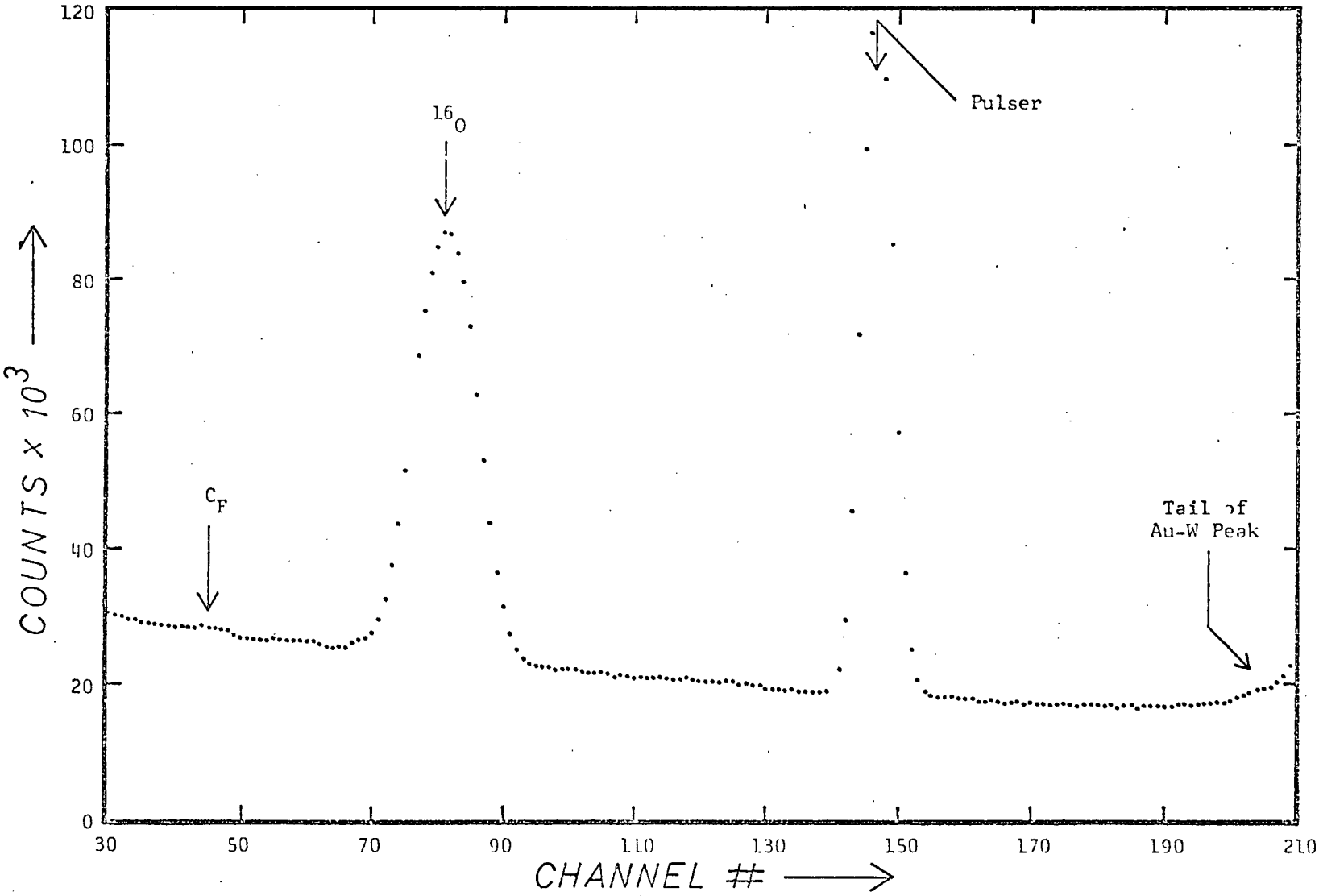


Figure 3.9 : $^{16}O(p,\gamma)^{17}F$ - associated scattering spectrum at 2.556 Mev proton energy.

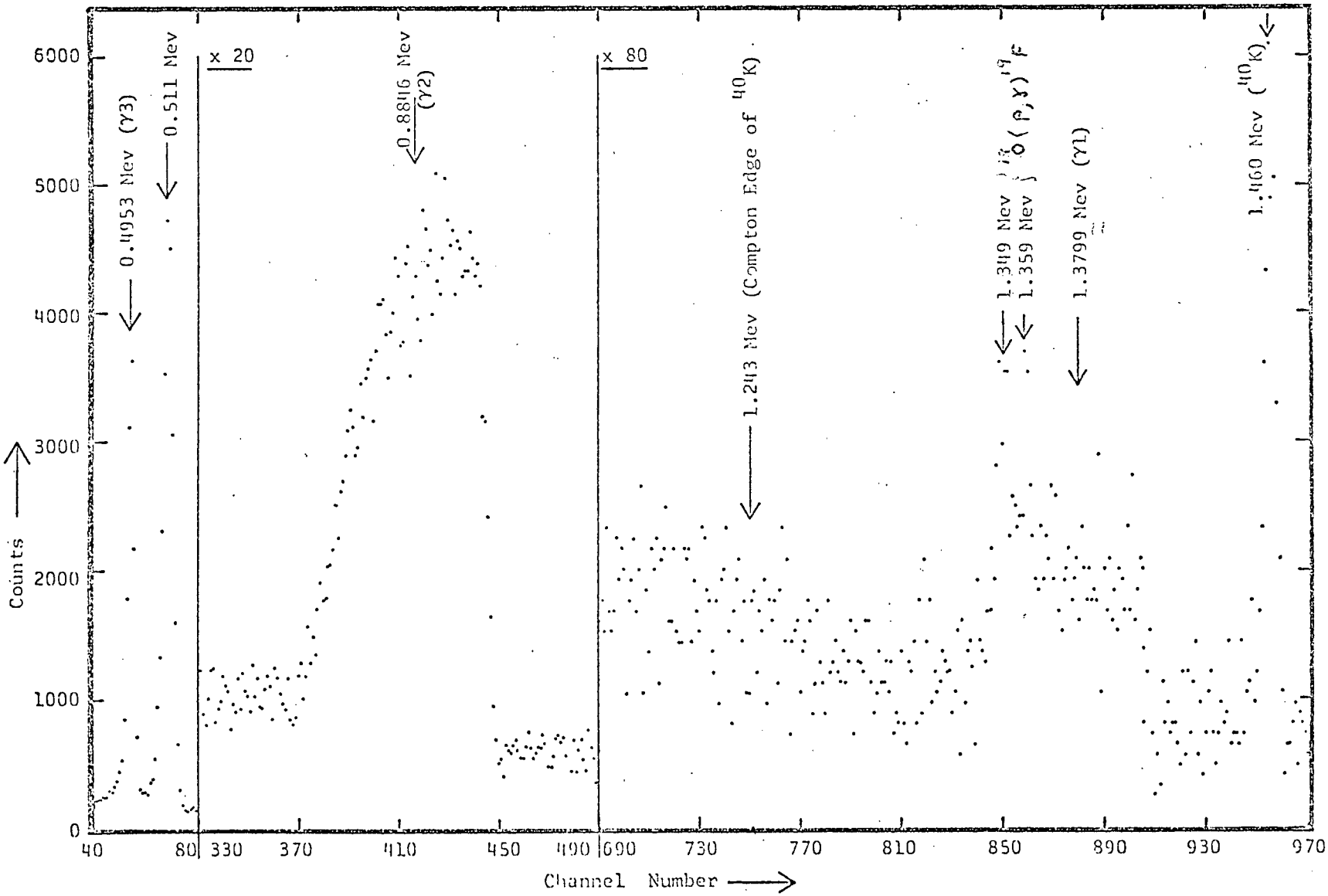


Figure 3.10 : $^{16}O(p,\gamma)^{17}F$ - Angular Distribution spectrum at 90° for 0.828 Mev proton energy.

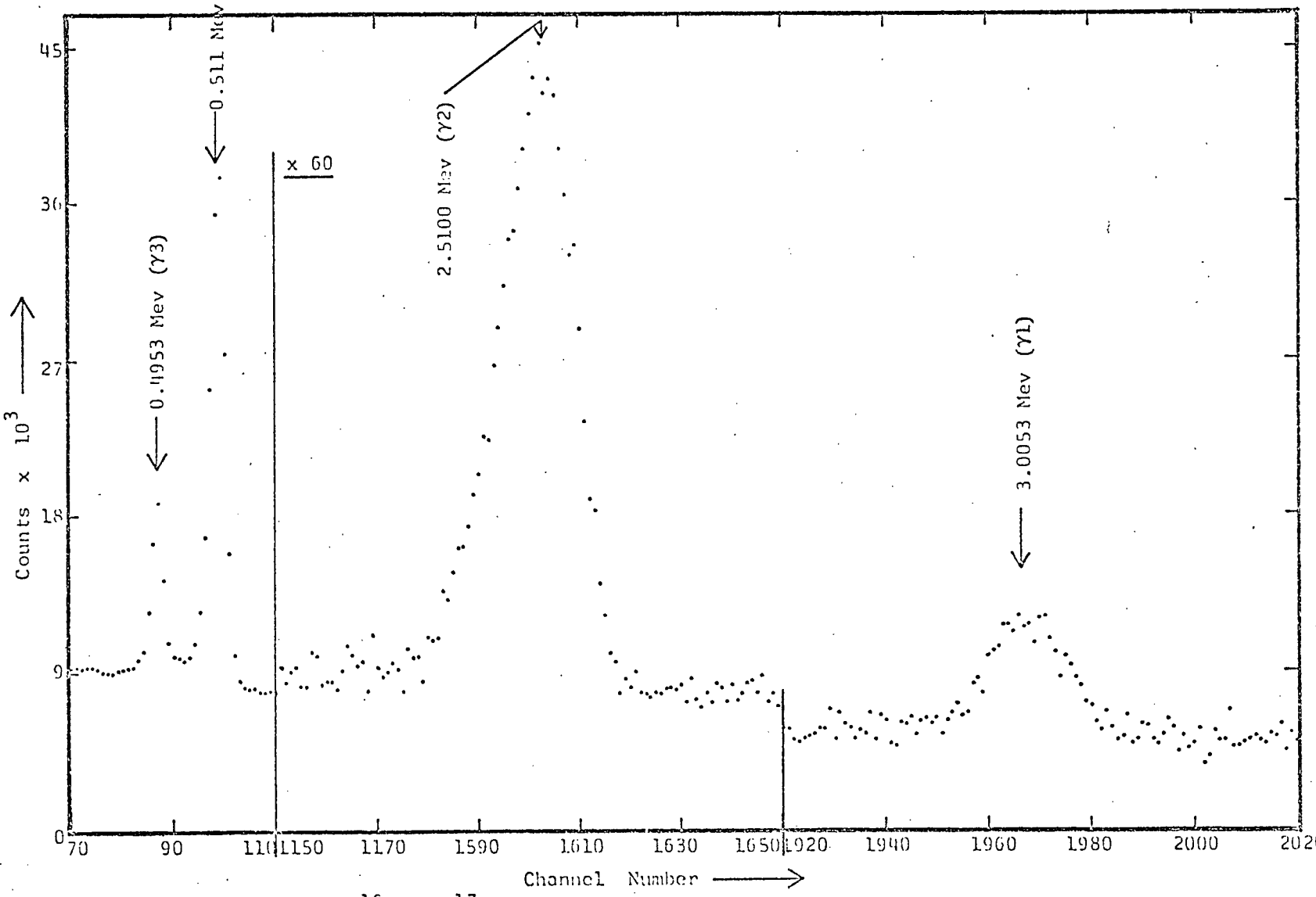


Figure 3.11 : $^{16}O(p,\gamma)^{17}F$ - Differential cross section spectrum at 90° for 2.556 Mev protons.

a peak in either spectrum due to all electronic count rate effects in that system is given directly by

$$\% \text{ removal} = \frac{\text{Number of Pulse Counts (Spectrum)}}{\text{Number of Pulse Counts (Scaler)}}$$

For the steady beam currents used, counting losses were determined to < 1% for all runs. The analyser data was converted to a useable form in the same way as before.

# CHAPTER 4

# CROSS SECTION CALCULATIONS

## 4.1 $^{16}O(p, p)^{16}O$

### 4.1a DEFINITION OF PARAMETERS AND ERRORS

The parameters that enter the calculations of the $^{16}O(p, p)^{16}O$ elastic scattering cross sections are, from eqn. 3.2.

$N_p$ = number of incident protons per run

$N_o$ = number of oxygen nuclei/cm$^2$ of target for each run

$\theta$ = scattering angle

E = reaction energy

$N_c$ = number of counts in the oxygen peak.

The determination of these quantities and their errors is discussed below.

#### Number of Incident Protons ($N_p$)

As discussed in section 3.1b, the beam current was monitored with the target biasing arrangement shown in Fig. 3.4 and the integrated charge was measured to within ± 1%.

#### Number of Oxygen Atoms/cm$^2$ of Target ($N_o$)

As revealed by data from the scattering measurements at the reference energy (Table 4.1b), the oxygen content of target #16 showed no measurable deterioration as a result of beam bombardment. Therefore, the comparisons of the runs at higher energies to the runs at the reference energy could be done assuming a constant yield at the reference

energy. Using the R.M.S. error for the different runs at the reference energy, this was valid to ± 0.4%.

Scattering Angle (θ)

The laboratory scattering angle was measured from the calibrated angular scale of the scattering chamber (section 3.1b) to be

$$\theta_{Lab} = 170°.9 \pm 0°.1 \quad .$$

This can be converted to center of mass coordinates using the relation

$$\theta_{CM} = \theta_{Lab} + \sin^{-1}\left[\frac{\text{mass of proton}}{\text{mass of } {}^{16}O}\right] \sin \theta_{Lab} \qquad -4.1$$

The result is $\theta_{CM} = 171°.5 \pm 0°.1$ .

There is a spread in the scattering angle due to multiple scattering of the beam in the target before and after the $^{16}O(p, p)^{16}O$ scattering event (Appendix C). The small change this makes to the cross section data can be determined by comparing the value of the scattering cross section at the mean angle, $\bar{\theta}$, with the value found by integrating the cross section over the weighted average of the scattering angles which contribute to the measured yield. This is given by

$$\left(\frac{d\sigma}{d\Omega}\right)(E,\theta) = \frac{\int \left(\frac{d\sigma}{d\Omega}\right)_{(E,\theta')} dP(\theta')\, d\theta'}{\int dP(\theta')\, d\theta'} \qquad - 4.2$$

where

$$dP(\theta') = \frac{1}{\theta_o\sqrt{2\pi}}\, e^{-(\theta'-\bar{\theta})^2/2\theta_o^2}\, d\theta' \qquad - 4.3$$

where $\bar{\theta} = 170°.9$

$$\theta_o = \frac{[\theta]_{RMS}}{\sqrt{2}} \quad \text{(Appendix C)} \quad .$$

The scattering cross section varies most rapidly with angle for the lower energy runs where the scattering is totally Rutherford. This is indicated by comparing the $^{16}O(p, p)^{16}O$ angular distribution at 1.25 Mev (Eppling, et. al., 1955) with the angular distribution for Rutherford scattering at this energy. This follows since the contribution to the scattering cross section from nuclear potential scattering will be predominantly S-wave scattering which is isotropic. Therefore, by replacing the total scattering cross section with the Rutherford cross section in eqn. 4.2, an upper limit to the error can be found. The results of multiple scattering effects calculated in this way using the theory of Mott and Massey (1965), are shown below,

| Proton Bombarding Energy (Mev) | $[\theta]_{RMS}$ : 1/e | $[\theta]_{RMS}$ : St. Dev. | Error in Cross Section |
|---|---|---|---|
| 0.4056 | 5°.18 | 3°.66 | 0.21% |
| 0.5053 | 3°.47 | 2°.45 | 0.09% |
| 0.6325 | 2°.75 | 1°.94 | 0.04% |
| 1.0000 | 1°.73 | 1°.22 | ≃ 0 |
| 2.0000 | 0°.86 | 0°.61 | ≃ 0 |

where the measured cross sections are greater than the cross sections for no multiple scattering by the error shown.

Reaction Energy (E)

The mean laboratory energy was determined from the bombarding energy (Appendix A) by considering the energy lost by the beam in the

target (Appendix C). The resulting errors in the energy are expressed in terms of the per cent error they give to the scattering cross section at that energy. Although the scattering at each mean energy is actually observed over a range of energies, the measured cross section and the cross section at the mean energy are not significantly different. Considering the measurement at the reference energy, where the cross section is totally Rutherford and is varying most rapidly with energy,

$$\left(\frac{d\sigma}{d\Omega}\right)_{(\bar{E},\theta)} = \frac{constant}{\bar{E}^2} \qquad -4.4$$

$$\left(\frac{d\sigma}{d\Omega}\right)_{(E,\theta)} = \int_{E_1}^{E_2} \left(\frac{d\sigma}{d\Omega}\right)_{(E',\theta)} dE' \approx \frac{constant}{E_1 E_2} \qquad -4.5$$

For $\bar{E}$ = 0.400 Mev , $\Delta E \simeq$ 10 Kev $\quad E_1$ = 0.395 Mev
$E_2$ = 0.405 Mev .

Therefore, $(\bar{E})^2 / E_1 E_2 = 1.0002$ .

Number of Counts in the Oxygen Peak ($N_c$)

The intensity or area of the $^{16}O$ peak in each scattering spectrum was found by determining the actual number of counts or "raw" area and then correcting this for electronic count rate effects and for the possible inclusion within this peak of counts due to scattering from carbon or any other contaminants that might be present in the target. The raw area was determined by a computer program which made a linear or second degree least squares fitted background subtraction followed by an addition of the counts per channel remaining. A range of "reasonable" fits were made to the background with this program and also graphically by hand. For each peak, an error to the fit was assigned by noting the variations in the peak

area for the range of possible reasonable fits. Errors were from 1% to 3% for all peaks. All $^{16}O$ peaks had > 20,000 counts, giving a statistical error of < ½%. Corrections to the area from electronic count rate effects were made as described in section 3.1c. The total count rate was monitored and the necessary corrections made using the factor 0.61% ± 0.05% loss per 1000 total counts/sec.

The carbon build-up on the target was characterized (section 3.1b) by

1) An approximately even build-up on the front and rear surfaces
2) An approximately linear build-up with accumulated beam charge.

For all energies used, the carbon peak due to scattering from the carbon accumulated on the rear of the target, $C_R$, was resolved from the $^{16}O$ peak (Appendix C). For energies up to 0.825 Mev, the carbon peak due to scattering from carbon accumulated on the front of the target, $C_F$, was embedded within the $^{16}O$ peak and its intensity was consequently included when finding the raw area of the $^{16}O$ peak and had to be corrected for. Since the intensity of these $C_F$ peaks could not be determined directly from those spectra in which they were embedded within the $^{16}O$ peak, they were corrected for as follows.

Using spectra whose $C_R$ peak is large enough above background to have its area determined, the ratio of $^{12}C$ atoms to $^{16}O$ atoms for these spectra was found by

$$\frac{\#\text{ of }^{12}C\text{ atoms}}{\#\text{ of }^{16}O\text{ atoms}} = \frac{(N_c)_{C_R}}{(N_c)_{^{16}O}} \times \frac{\left(\frac{d\sigma}{d\Omega}\right)_{^{16}O}}{\left(\frac{d\sigma}{d\Omega}\right)_{^{12}C}} \qquad - 4.6$$

where $N_C$ = number of counts in the respective peaks, and the ratio of the

scattering cross sections for protons on $^{12}C$ and $^{16}O$ was obtained from data shown in Fig. 4.1. In this figure, the $^{16}O(p, p)^{16}O$ scattering data is from the present work. The $^{12}C(p, p)^{12}C$ scattering data is from Jackson, et. al. (1953) and Milne (1954). Assuming that $C_F = C_R$ and allowing for the change with time in the amount of carbon for the other spectra, the $^{16}O$ peak for each spectrum was corrected by an amount

$$\% \text{ subtracted from } {}^{16}O \text{ peak} = \frac{\#\text{ of } {}^{12}C \text{ atoms}}{\#\text{ of } {}^{16}O \text{ atoms}} \times \frac{\left(\frac{d\sigma}{d\Omega}\right)_{^{12}C}}{\left(\frac{d\sigma}{d\Omega}\right)_{^{16}O}} \qquad - 4.7$$

For all spectra the total correction was < 2% of the $^{16}O$ peak itself. The ratio of cross sections is known to about 5-10%. And, typically, the area of $C_R$ is determined to about 10% and $C_R = C_F$ to within about 20%. Therefore, the correction is accurate to about

$$\left[\sqrt{(10\%)^2 + (10\%)^2 + (20\%)^2}\right] \times [2\%] \approx (25\%)(2\%) = 0.5\%$$

Possible corrections for scattering from contaminants of mass numbers close enough to $^{16}O$ that their contributions would be within the $^{16}O$ peak were also considered (Appendix C). The contaminants considered were

$$^{13}C,\ ^{14}N,\ ^{17}O,\ ^{18}O,\ ^{19}F$$

For all energies used the contributions in the $^{16}O$ peak due to $^{18}O$, over and above its contribution at the reference energy of 0.4056 Mev, is < 0.2% and has been neglected. Likewise the contribution from $^{17}O$ has been neglected. For all energies used, the contribution from $^{13}C$ is approximately 1% that of $^{12}C$ and has been neglected. There is no a priori reason to suppose that either $^{14}N$ or $^{19}F$ are present in the target in large quantities. Furthermore, their presence was not noticed at the higher energy runs where their scattering peaks would have been

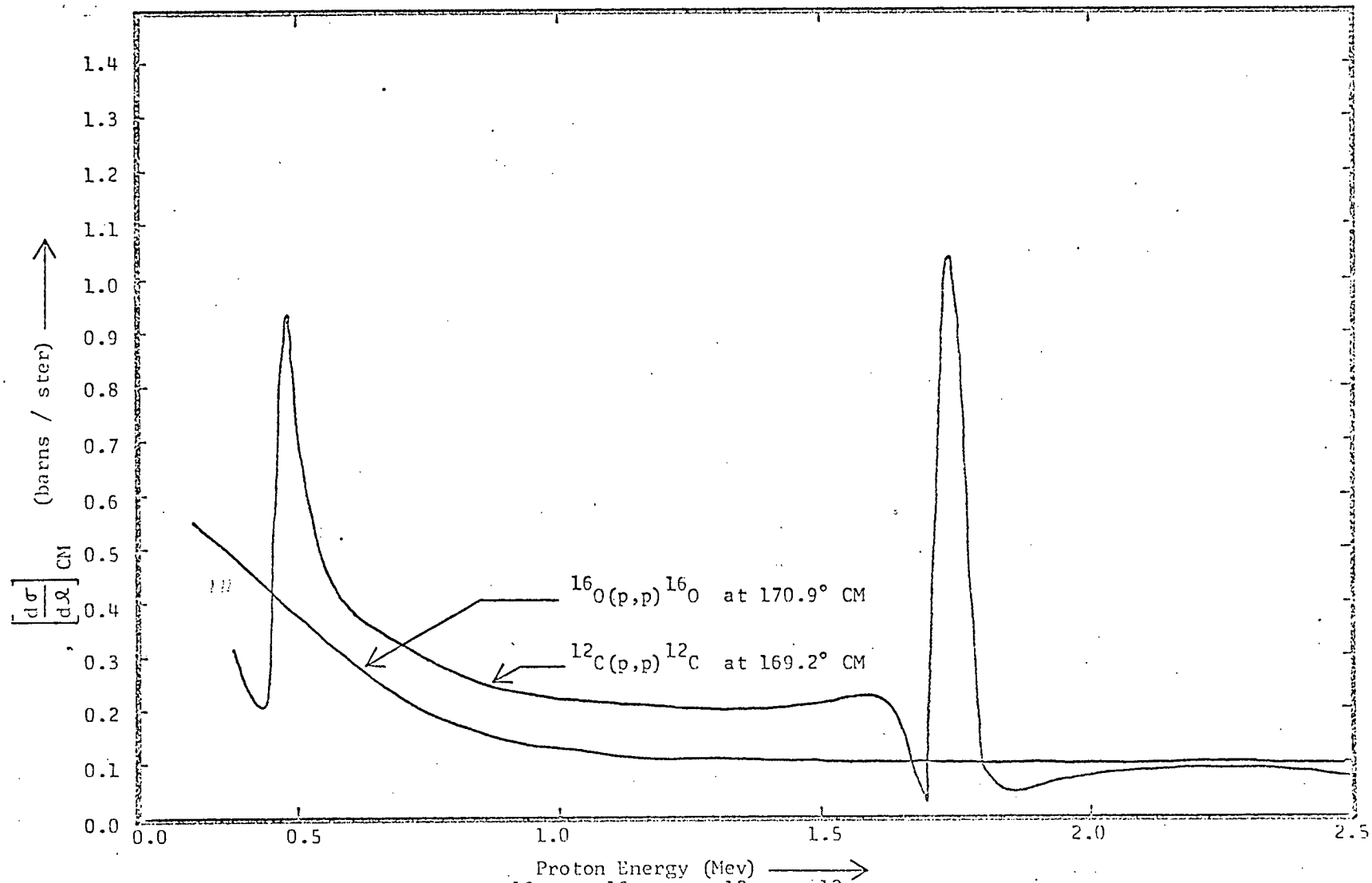


Figure 4.1 : $^{16}O(p,p)^{16}O$ and $^{12}C(p,p)^{12}C$ differential cross sections.

isolated. Therefore, contributions to the $^{16}O$ peak from these nuclei have also been neglected.

## 4.1b SCATTERING YIELDS AND CROSS SECTIONS

Using the parameters just discussed, the scattering yields for each run are tabulated in Tables 4.1a - 4.1c. Table 4.1a shows the yields from the series of runs (on target #17) that were designed to confirm that the total contribution to the scattering cross section, at the reference bombarding energy of 0.4056 Mev, was from Rutherford scattering. Table 4.1b shows the yields (on target #16) for the eight runs at the reference bombarding energy of 0.4056 Mev. Table 4.1c shows the yields (on target #16) of the 15 runs at bombarding energies from 0.5053 to 2.000 Mev. Corrections due to electronic count rate effects have been added to the raw area and corrections for the $C_F$ peak have been subtracted. The average yield at the reference energy has been decreased by 0.21% for multiple scattering effects; otherwise multiple scattering has been neglected. The final errors in each yield is the R.M.S. of the errors of the factors that contribute to it.

From Table 4.1a, the yields at 0.3334, 0.3815 and 0.4055 Mev mean center of mass energy were normalized to a yield of unity at 0.3627 Mev center of mass energy using the average of the three runs at this energy. The differences in multiple scattering corrections to the yield at 0.3627 Mev and the other three energies was < 0.1% and was neglected. A least square fit of this data to a $(E_{cm})^{-2}$ energy dependence gave a $\chi^2 = 0.56$ which for three degrees of freedom gives a Chi-squared probability of 90%. Although this probability is a little higher than would be expected considering the

| Beam Energy (Kev) | Mean Laboratory Energy (Kev) | Fitted counts in Oxygen Peak | Clock Time (sec) | Relative Integrated Charge ($\mu$c) | Total Count Rate (counts/sec) | Electronic Count Rate Correction (add) | Carbon Correction (subtract) | Relative Yield (counts/$\mu$c) |
|---|---|---|---|---|---|---|---|---|
| 405.5 | 385.6 | 26,175 | 979.2 | 40.78 | 3238 | 2.84 % | 0.42 % | 658 |
| 375.0 | 354.4 | 30,740 | 1252.8 | 40.93 | 2987 | 2.62 % | 0.64 % | 766 |
| 425.0 | 405.6 | 36,199 | 1369.8 | 60.99 | 3154 | 2.76 % | 0.24 % | 609 |
| 405.5 | 385.6 | 26,272 | 1124.4 | 40.81 | 2830 | 2.49 % | 0.42 % | 657 |
| 450.0 | 431.1 | 31,408 | 1351.2 | 60.95 | 2863 | 2.51 % | 0.50 % | 526 |
| 405.5 | 385.6 | 26,218 | 1018.8 | 40.72 | 3118 | 2.73 % | 0.42 % | 659 |
| $\pm$ 0.5 kev | $\pm$ 1.3 kev $\Rightarrow$ 0.7 % | $\pm \simeq$ 1.5% | $\pm \approx$ 0 % | $\pm <$ 1% | $\pm \approx$ 0 % | $\pm$ 0.15 % absolute $\pm \approx$ 0 % relative | $\pm$ 0.2 % | $\pm <$ 2.0% |

Table 4.1a : Scattering yields to confirm pure Rutherfore scattering at 0.4056 Mev bombarding energy.

| Beam Energy (Kev) | Mean Laboratory Energy (Kev) | Fitted counts in Oxygen Peak | Clock Time (sec) | Relative Integrated Charge ($\mu$c) | Total Count Rate (counts/sec) | Electronic Count Rate Correction (add) | Carbon Correction (subtract) | Relative Yield (counts/$\mu$c) |
|---|---|---|---|---|---|---|---|---|
| 405.6 | 385.5 | 28,450 ±2% | 1033.4 | 40.98 | 3059 | 2.69 % | 0.9 % | 707 ± 17 |
| 405.6 | 385.5 | 27,510 ±2% | 1009.1 | 40.93 | 3086 | 2.70 % | 0.9 % | 684 ± 16 |
| 405.6 | 385.5 | 27,760 ±1% | 1034.8 | 40.98 | 3022 | 2.65 % | 0.9 % | 689 ± 11 |
| 405.6 | 385.5 | 28,470 ±1% | 1009.4 | 41.00 | 3068 | 2.69 % | 0.9 % | 707 ± 11 |
| 405.6 | 385.5 | 27,800 ±1.5% | 1089.4 | 41.08 | 2901 | 2.54 % | 0.9 % | 688 ± 14 |
| 405.6 | 385.5 | 27,900 ±1% | 1054.3 | 41.05 | 3027 | 2.66 % | 0.9 % | 692 ± 11 |
| 405.5 | 385.4 | 27,909 ±1% | 1021.0 | 41.01 | 3019 | 2.64 % | 0.9 % | 693 ± 11 |
| 405.5 | 385.4 | 28,039 ±1% | 1071.6 | 40.87 | 2887 | 2.53 % | 0.9 % | 697 ± 11 |
| ± 0.5 kev | ± 1.3 kev ⇒ 0.7 % | | ± ≈ 0 % | ± < 1% | ± ≈ 0 % | ± 0.1 % absolute ± 0 % relative | ± 0.3 % | RMS Average = 694.6 ± 4.6 |

Table 4.1b : Scattering yields at the reference bombarding energy of 0.4056 Mev.

| Beam Energy (Kev) | Mean Laboratory Energy (Kev) | Fitted counts in Oxygen Peak | Clock Time (sec) ± ≈0 % | Relative Integrated Charge (μc) ± < 1% | Total Count Rate (counts/sec) ± ≈0 % | Electronic Count Rate Correction (add) ± 0.1 % | Carbon Correction (subtract) | Relative Yield (counts/μc) |
|---|---|---|---|---|---|---|---|---|
| 505.3 ± 0.5 | 487.1 ⇒ ± 0.5% | 34,800 ±3% | 1311.4 | 81.25 | 3060 | 2.69 % | (1.8 ±0.5)% | 432.2 ± 3.1% |
| 632.5 ± 0.3 | 616.2 ± 0.4% | 32,725 ±3% | 1200.2 | 121.14 | 2998 | 2.63 % | (2.0 ±0.5)% | 271.9 ± 3.1% |
| 678.8 ±1.0 | 663.1 ± 0.4% | 35,100 ±3% | 1284.7 | 141.24 | 2988 | 2.63 % | (1.8 ±0.5)% | 250.6 ± 3.1% |
| 731.3 ± 0.5 | 716.2 ± 0.4% | 30,600 ±3% | 1093.3 | 141.08 | 3048 | 2.69 % | (2.0 ±0.5)% | 218.4 ± 3.1% |
| 773.7 ± 0.5 | 759.0 ± 0.3% | 29,200 ±3% | 962.5 | 140.94 | 3112 | 2.73 % | (2.1 ±0.5)% | 208.5 ± 3.1% |
| 825.0 ± 1.0 | 810.8 ± 0.3% | 39,750 ±3% | 1236.0 | 201.21 | 2995 | 2.63 % | (2.0 ±0.5)% | 198.8 ± 3.1% |
| 875.0 ± 1.0 | 861.2 ± 0.3% | 36,600 ±3% | 1087.2 | 201.05 | 3002 | 2.66 % | NONE | 187.0 ± 3.1% |
| 919.2 ± 0.5 | 905.8 ± 0.2% | 32,050 ±2% | 1034.9 | 200.01 | 2988 | 2.63 % | NONE | 163.8 ± 2.1% |
| 991.9 ± 0.5 | 979.0 ± 0.2% | 30,400 ±2% | 840.2 | 200.84 | 3139 | 2.73 % | NONE | 155.6 ± 2.1% |
| 1118.4 ± 1.0 | 1106.3 ± 0.2% | 27,000 ±2% | 684.7 | 200.68 | 2984 | 2.63 % | NONE | 138.2 ± 2.1% |
| 1262.2 ± 1.0 | 1250.8 ± 0.2% | 25,000 ±2% | 637.3 | 200.61 | 2929 | 2.58 % | NONE | 127.9 ± 2.1% |
| 1381.3 ± 1.0 | 1370.4 ± 0.2% | 24,000 ±2% | 517.5 | 200.49 | 3276 | 2.87 % | NONE | 123.2 ± 2.1% |
| 1600.0 ± 2.0 | 1589.8 ± 0.2% | 22,840 ±2% | 330.7 | 200.33 | 3076 | 2.69 % | NONE | 117.2 ± 2.1% |
| 1800.0 ± 2.0 | 1790.3 ± 0.2% | 20,550 ±2% | 347.2 | 200.34 | 3222 | 2.84 % | NONE | 105.6 ± 2.1% |
| 2000.0 ± 2.0 | 1990.9 ± 0.2% | 20,580 ±2% | 730.5 | 200.68 | 1155 | 1.01 % | NONE | 103.6 ± 2.1% |

Table 4.1c : Scattering yields for bombarding energies from 0.5053 to 2.000 Mev.

statistical accuracy of the data, it does indicate that the scattering in the region of the reference energy is pure Rutherford scattering. The results are shown in Fig. 4.2.

The differential scattering cross section at each energy was obtained by a direct comparison of the yield with the R.M.S. yield at the reference energy. The center of mass and laboratory cross sections, expressed in mb/ster and relative to the Rutherford cross section, are given in Table 4.2. The cross section is also shown in Fig. 4.3 where comparison is made with the previous data of Eppling (1952), et. al. (1955). The best fit to the data was obtained by eye. Least square fits made with power series of various orders showed small oscillations centered approximately about the eye fit. The final error to the scattering data is

$$\epsilon_{RMS} = \frac{1}{16}\sqrt{\sum_{i=1}^{16} \epsilon_i^2} = 0.5\% \quad .$$

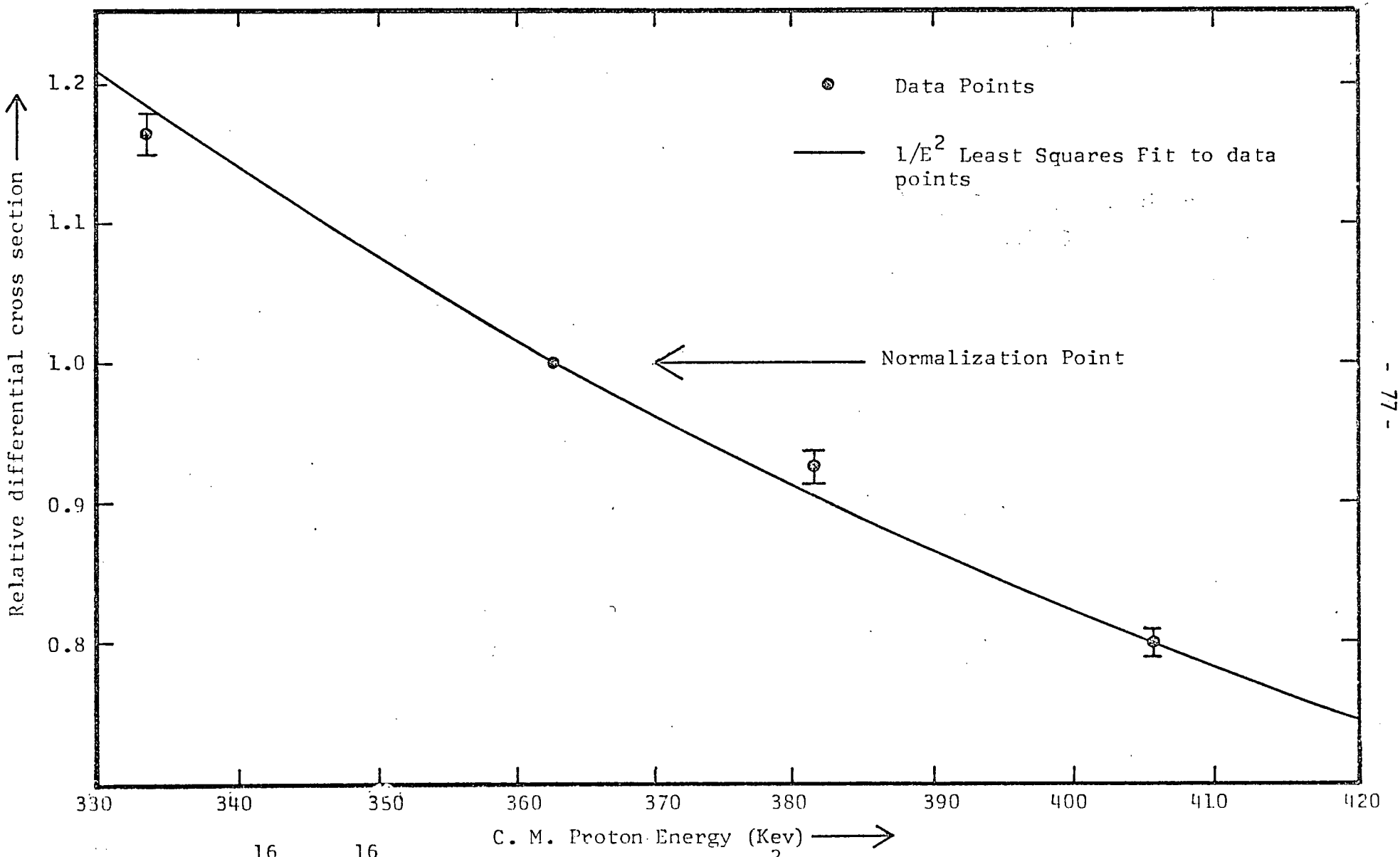


Figure 4.2 : $^{16}O(p,p)^{16}O$ cross section compared to $1/E^2$ relation at low bombarding energies.

| Mean Reaction Energy (Kev) | | Differential Cross Section (mb/ster) | | | | $\left(\frac{d\sigma}{d\Omega}\right)_{\text{Total}} / \left(\frac{d\sigma}{d\Omega}\right)_{\text{Rutherford}}$ |
|---|---|---|---|---|---|---|
| | | Rutherford | | Total | | |
| Lab. | C. M. | Lab. | C. M. | Lab. | C. M. | |
| 385.5 ± 1.3 | 362.6 | 561.1 | 638.0 | 561.1 (±4 ) | 638.0 (±4 ) | 1.0000 |
| 487.1 ± 1.3 | 458.2 | 351.4 | 399.5 | 350 ± 10 | 398 ± 11 | 0.99 ± 0.03 |
| 616.2 ± 1.2 | 579.7 | 219.6 | 249.7 | 220 ± 6 | 250 ± 7 | 1.00 ± 0.03 |
| 663.1 ± 1.1 | 623.8 | 189.6 | 215.6 | 203 ± 6 | 231 ± 6 | 1.07 ± 0.03 |
| 716.2 ± 1.1 | 673.7 | 162.6 | 184.9 | 176 ± 6 | 200 ± 6 | 1.08 ± 0.03 |
| 759.0 ± 1.1 | 714.0 | 144.7 | 164.5 | 168 ± 5 | 191 ± 5 | 1.16 ± 0.04 |
| 810.8 ± 1.5 | 762.7 | 126.8 | 144.2 | 161 ± 5 | 183 ± 5 | 1.27 ± 0.04 |
| 861.2 ± 1.5 | 810.1 | 112.4 | 127.8 | 151 ± 5 | 172 ± 5 | 1.34 ± 0.05 |
| 905.8 ± 1.0 | 852.1 | 101.6 | 115.5 | 133 ± 3 | 151 ± 3 | 1.31 ± 0.03 |
| 979.0 ± 1.0 | 920.9 | 87.0 | 98.9 | 126 ± 3 | 143 ± 3 | 1.45 ± 0.03 |
| 1106.3 ± 1.5 | 1040.7 | 68.1 | 77.4 | 111 ± 3 | 127 ± 3 | 1.64 ± 0.03 |
| 1250.8 ± 1.5 | 1176.6 | 53.3 | 60.6 | 103 ± 2.5 | 118 ± 2.5 | 1.94 ± 0.04 |
| 1370.4 ± 1.5 | 1289.1 | 44.4 | 50.5 | 99 ± 2.4 | 113 ± 2.5 | 2.24 ± 0.04 |
| 1589.8 ± 2.5 | 1495.5 | 33.0 | 37.5 | 94.7± 1.9 | 107.5± 2.2 | 2.87 ± 0.05 |
| 1790.3 ± 2.5 | 1684.1 | 26.0 | 29.6 | 85.5± 1.7 | 97.0± 2.0 | 3.28 ± 0.07 |
| 1990.9 ± 2.5 | 1872.8 | 21.0 | 23.9 | 83.9± 1.7 | 95.2± 1.9 | 3.98 ± 0.09 |

Table 4.2 : $^{16}O(p,p)^{16}O$ cross section data.

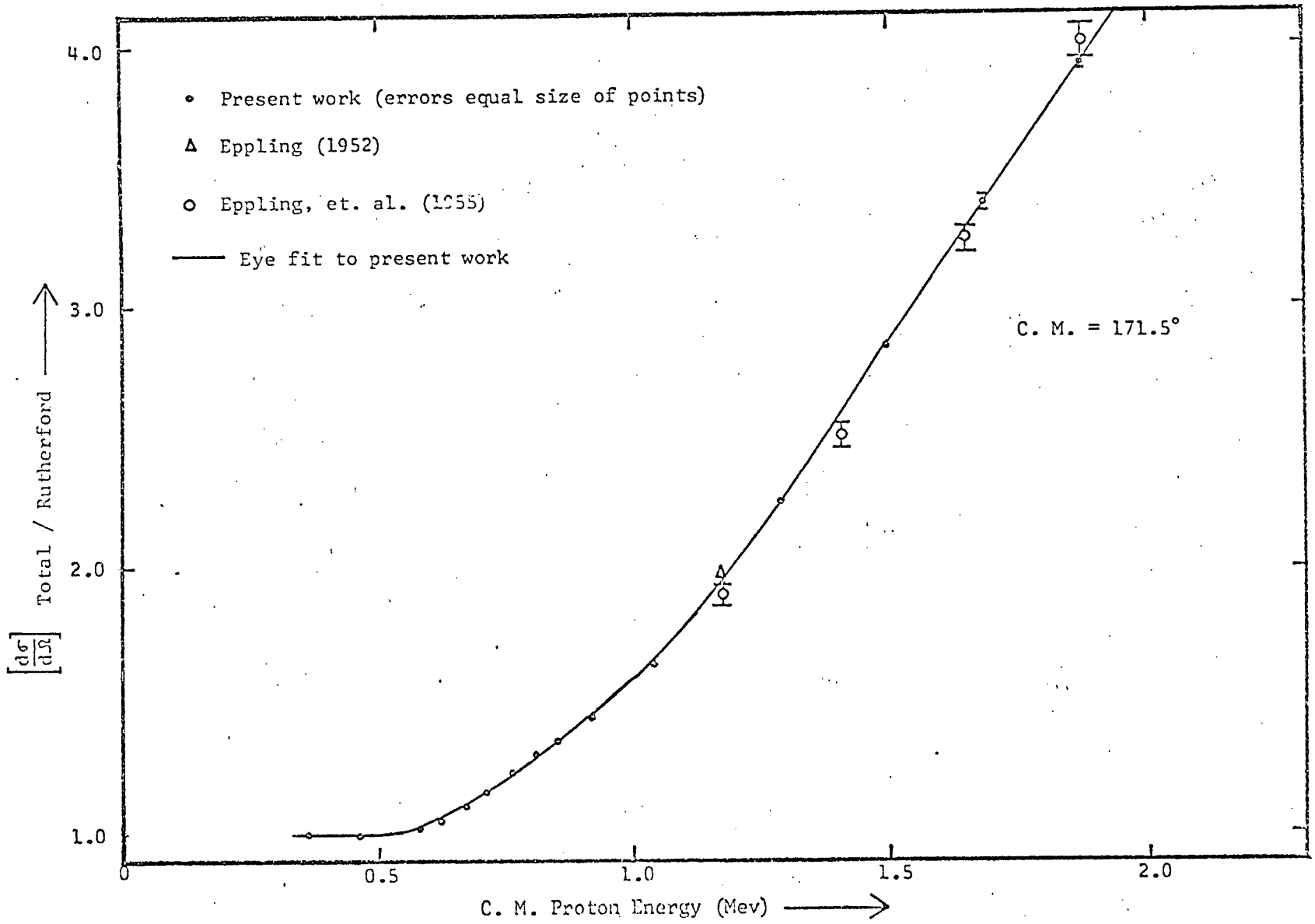


Figure 4.3 : $^{16}O(p,p)^{16}O$ differential cross section.

## 4.2 $^{16}O(p, \gamma)^{17}F$

### 4.2a DEFINITION OF PARAMETERS AND ERRORS

The parameters that enter into the estimation of the $^{16}O(p, \gamma)^{17}F$ cross sections are, from eqns. 3.4, 3.6, and 3.8,

$E$ = reaction energy

$\theta_\gamma$ = reaction angle

$\left(\frac{d\sigma}{d\Omega}\right)_{(E,\theta_p)}$ = $^{16}O(p, p)^{16}O$ differential cross section at $\theta_p$

$d\Omega_p$ = solid angle subtended by the proton detector

$(d\Omega \varepsilon T)_\gamma$ = Ge(Li) detector efficiency function

$N_{cp}$ = number of counts in the $^{16}O$ scattering spectrum

$N_{c\gamma}(\gamma=1,2,3)$ = number of counts in the gamma ray peaks .

The determination of these quantities and their errors is discussed below.

Reaction Energy (E)

The mean reaction energy was found by two independent methods. For four of the cross section runs on the Au-$WO_3$ transmission targets the mean reaction energy was determined to ± 2 or 3 Kev by calibrating the beam energy (Appendix A) and correcting for energy loss in the targets (Appendix C) whose thicknesses had been measured (section 2.4a). For the rest of the cross section runs the calibration of the beam was unreliable (Appendix A). For the angular distribution runs, the thicknesses of the $Ta_2O_5$ targets was known only approximately (section 2.4b). Therefore, for all runs the mean reaction energy was deduced from the observed energies of $\gamma 2$ in the direct capture spectra and the

reaction energetics (Fig. 1.1). The channel number of the $\gamma 2$ peak was determined by a computer program that found its centroid. Its energy was determined to ± 1 Kev by a computer program that calibrated the energy of the spectra from the energy calibration runs taken before and after each direct capture run. For those runs whose reaction energies had been found by both of these methods, the energies agreed to ± 2 Kev. For consistency, the reaction energies used were those found from the direct capture spectra.

Although some of the targets used for these measurements were considerably thicker than the targets that had been used for the previous measurements of the elastic scattering cross section, the direct capture cross section varies less rapidly with energy than does the Rutherford scattering cross section at 0.4 Mev (section 2.4a) and can still be calculated using the mean reaction energy without introducing a significant error. For the worst case of 0.8 Mev protons incident upon a 70 Kev thick oxide layer, the cross section obtained by considering the yield at the mean reaction energy differs by only ½% from the cross section obtained by estimating the energy dependent yield (obtained from the results of this work) integrated over the target thickness.

Reaction Angle ($\theta_\gamma$)

The detector angle, as measured by the angular distribution table could be set to ± ½° (section 3.2b). The position of the Ge(Li) crystal, as seen from the target, within the cryostat was determined to ± 1° (Appendix B). The angular extent of the Ge(Li) crystal was several degrees, depending upon its distance from the target (Appendix B).

Compared to this large extent of the Ge(Li) crystal, the angular spreading of the beam, after collimation and multiple scattering in the target, was relatively unimportant.

## $^{16}O(p, p)^{16}O$ Scattering Cross Sections $(d\sigma/d\Omega)_{(E,\theta_p)}$

The $^{16}O(p, p)^{16}O$ cross section was measured in this work at a mean laboratory scattering angle of 170°.9 ± 0.1°. The $^{16}O(p, \gamma)^{17}F$ direct capture cross section was normalized to the elastic scattering observed at 173°.0. Angular distribution data, accurate enough to correct the measured scattering cross section at this new angle is not available. This small correction was, therefore, estimated as follows. From the classical Rutherford scattering cross section, the relative difference between the Rutherford scattering at the two angles is

$$\frac{(d\sigma/d\Omega)^{(170°.9)}_{Rutherford} - (d\sigma/d\Omega)^{(173°.0)}_{Rutherford}}{(d\sigma/d\Omega)^{(170°.9)}_{Rutherford}} = 0.0052 \qquad - 4.8$$

The contribution to the total cross section from nuclear potential scattering should be very nearly isotropic S-wave scattering and should not be significantly different at the two angles. Therefore, the relative difference in the total scattering at the two angles becomes

$$\frac{(d\sigma/d\Omega)^{(170°.9)}_{Total} - (d\sigma/d\Omega)^{(173°.0)}_{Total}}{(d\sigma/d\Omega)^{(170°.9)}_{Total}} = \frac{0.0052}{K} \qquad - 4.9$$

where $K = \dfrac{(d\sigma/d\Omega)_{Total}}{(d\sigma/d\Omega)_{Rutherford}}$ as 170°.9 as measured in this work.

The values of the $^{16}O(p, p)^{16}O$ scattering cross section at 173°.0, used for normalizing the direct capture data, are shown below.

| Mean Laboratory Reaction Energy (Mev) | $^{16}O(p,p)^{16}O$ Lab. ($d\sigma/d\Omega$)(mb/ster) at 170°.9 Lab. | K | Correction Factor | $^{16}O(p,p)^{16}O$ Lab. ($d\sigma/d\Omega$)(mb/ster) at 173°.0 Lab. |
|---|---|---|---|---|
| 0.845 | 149.1 * | 1.27 | 0.9959 | 148.5 |
| 1.086 | 113.2 | 1.62 | 0.9970 | 112.9 |
| 1.094 | 112.7 | 1.63 | 0.9968 | 112.3 |
| 1.369 | 100.0 | 2.25 | 0.9977 | 99.8 |
| 1.670 | 91.5 | 3.06 | 0.9983 | 91.4 |
| 1.952 | 82.8 | 3.81 | 0.9986 | 82.7 |
| 2.555 | 75.1 | 5.40 | 0.9990 | 75.0 |

* From eye fit to data (Fig. 4.1c)

This small correction did not significantly change the error in the scattering data measured at 170°.9.

Proton Detector Solid Angle ($d\Omega_p$)

The plane of the circular collimator covering the proton detector was not positioned perpendicularly to the target-to-dector direction. This follows from the construction of the (p, $\gamma$) reaction chamber (Fig. 3.6), in which the proton detector is set into the end plate of the large tube which houses the beam tube. The necessary measured parameters of the detector collimator are given on page 56 of section 3.2b. The circular collimator, having been rotated through an angle

$$\phi = 180° - \theta_p = 7°.01 \pm 0°.05$$

from the normal orientation now appears to the target as an ellipse with major and minor axes of, d, and, $d\cos(\theta_p)$ respectively. Furthermore, there is an additional reduction in the solid angle due to the thickness, t, of the collimator edge.

The effective solid angle, $d\Omega$, was calculated using two approximations, both producing only second order errors. First, the protons incident upon

the detector were considered as a parallel beam. With this approximation, the effect of the edge thickness is to make the collimator appear as two ellipses, one representing the front surface and one the back surface, which are displaced laterally from each other by an amount

$$\ell = t \sin \phi = (0.023 \pm 0.002) \text{ mm} .$$

The effective area of the collimator is, therefore, reduced by an amount, $\delta A$, corresponding to the crescent shaped area which has been obstructed by this displacement. The second approximation is to consider this elliptical crescent, $\delta A$, as a circular crescent formed by similarly displacing two circles each of radius r as shown in Fig. 4.4. From the figure,

$$d\Omega_p = \frac{\pi r^2 \cos \phi - \delta A}{D^2} = 1.352 \pm 0.009 \times 10^{-3} \text{ steradians.}$$

The rotated orientation of the proton detector has had the effect of reducing the solid angle, relative to its normal value of $\pi r^2/D^2$ by $2.0 \pm 0.1\%$.

Ge(Li) Detector Efficiency Function $\left((d\Omega\ \varepsilon\ T)_\gamma\right)$

This function was determined for each of the nine geometries used as discussed in Appendix B. Its values, as read from the graphs so determined, were accurate to $< \pm 2\%$.

Number of Counts in the $^{16}O$ Peak $(N_{cp})$

The intensities of the $^{16}O$ peak in the scattering spectra were determined similarly as discussed in section 4.1. The only differences being that the electronic count rate effects were treated as discussed

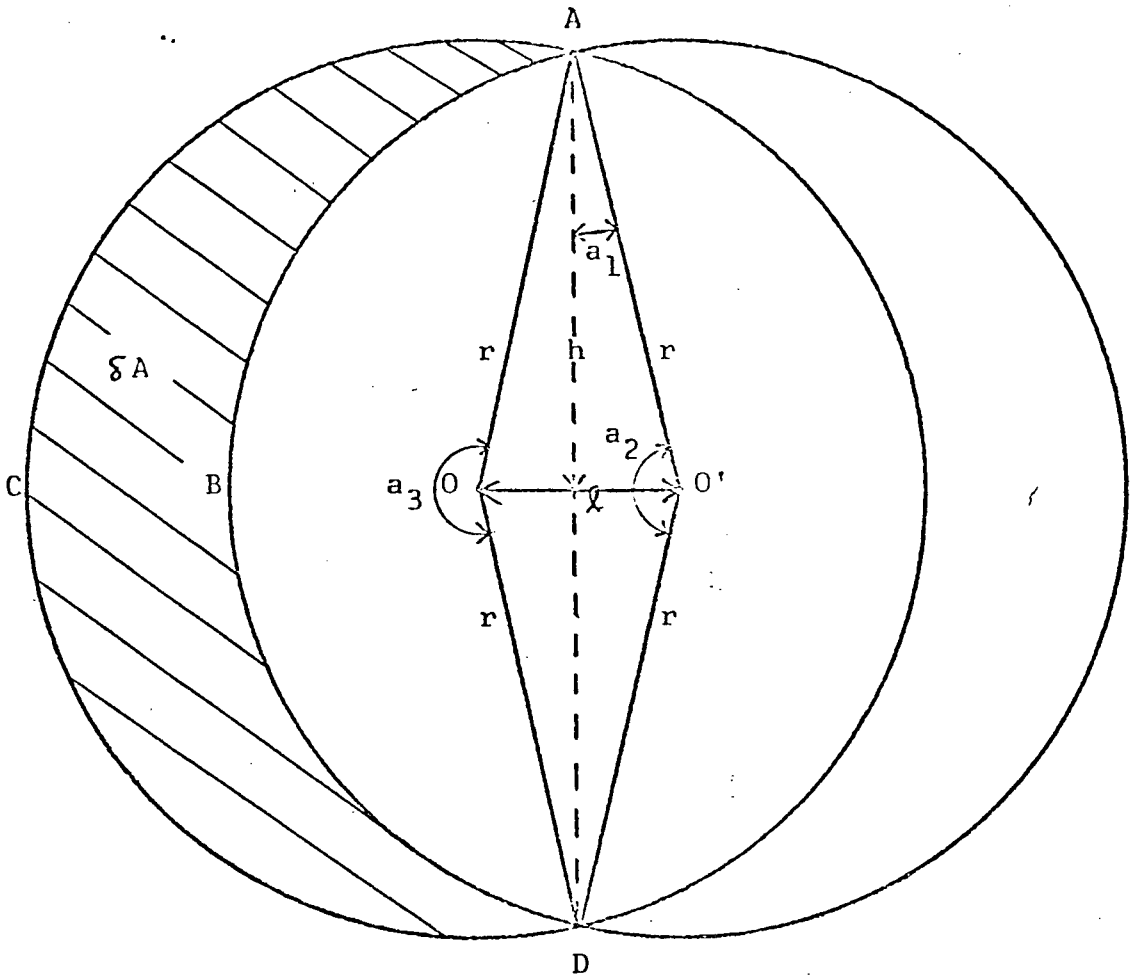


Define: $A_1$ = AODO'

$A_2$ = ABDO' = area of sector of circle O' with included angle $a_2$

$A_3$ = ACDO = " O " $a_3$

$a_1 = \sin^{-1}\left(\frac{d/2}{r}\right) = 0°.55 \pm 0°.05$

$a_2 = 2(90° - a_3) = 178°.90 \pm 0°.05$

$a_3 = 360° - a_2 = 181°.10 \pm 0°.05$

Therefore: $A_1 = dh = \frac{d^2 \cot a_1}{2} = (0.0274 \pm 0.0042)\ mm^2$

$A_2 = \frac{\pi r^2}{360}\ a_2 = (0.01239)(178°.90) = 2.2164\ mm^2$

$A_3 = \frac{\pi r^2}{360}\ a_3 = (0.01239)(181°.10) = 2.2438\ mm^2$

$\delta A = A_3 - A_2 + A_1 = (0.0548 \pm 0.0042)\ mm^2$

Figure 4.4 : Proton detector collimator geometry.

in section 3.2c, and the small correction for scattering by $^{18}O$ was included. The number of counts in the $^{16}O$ peak varied from 0.5 to $2.0 \times 10^6$ and was determined with accuracies from ± 0.1 to 0.3%.

Number of Counts in the Direct Capture Peaks ($N_{c\gamma}$)

The raw counts in the γ1 and γ2 peaks were found using the same program that was used to fit the scattering peaks. Because of the much weaker intensity of the γ1 transition, the signal-to-noise ratio for these peaks was considerably lower than for the γ2 peaks, and the determination of their number of counts was improved by constraining each γ1 peak to have a similar shape as the γ2 peak in the same spectrum. The γ3 peak, however, was partially overlapping the 0.511 Mev annihilation peak and could not be analysed in the same way. The areas of the γ3 peaks were needed only for the angular distribution data, and their areas were needed only relative to each other for each set of angular distributions at each bombarding energy (section 3.2a). These relative areas were found using a peak fitting program (Johnson, 1972), and also graphically by hand. The results agreed to within 2% for all but one of the γ3 peaks, whose areas, as found by the two methods, disagreed by 6%.

Three corrections had to be made to the raw intensities of γ1, γ2 and γ3. These corrections are, however, interdependent. They are:

1). A correction for electronic count rate effects which had to be made to all three transitions by multiplying their raw counts in each spectrum by the factor

$$K_1 = \frac{\text{\# of counts (Scaler)}}{\text{\# of counts (Spectrum)}} \qquad -4.10$$

as discussed in section 3.2c.

2). All three transitions had to be corrected for the occasional summing of $\gamma 2 + \gamma 3 \rightarrow \gamma 1$ due to the finite solid angle subtended by the Ge(Li) detector. This is a geometrical summing effect, occuring for an individual capture event, and not an electronic count rate summing of seperate capture events occurring closely in time. Any particular capture event can proceed via $\gamma 1$, or, via $\gamma 2$ followed by $\gamma 3$. If it proceeds via $\gamma 1$, there is no problem. However, given that $\gamma 2$ has been counted (which means that for this particular capture event $\gamma 1$ does not exist), there is a probability, P, that $\gamma 3$ will also be counted and cause $\gamma 2 + \gamma 3$ to sum to $\gamma 1$. The lifetime of the $s_{1/2}$ state of $^{17}F$ is $(412 \pm 9) \times 10^{-12}$ sec (Ajzenberg-Selove, 1971) which is well within the resolving time of the counting system. Although the angular distribution of $\gamma 3$ is isotropic (section 3.2a) it may still be correlated with $\gamma 2$. Unfortunately there is no $\gamma 2 - \gamma 3$ angular correlation data for $^{16}O(p, \gamma)^{17}F$. However, this total geometrical summing correction is small and any $\gamma 2 - \gamma 3$ correlation, if it did exist, would be a second order effect. Therefore, assuming $\gamma 3$ to be isotropic with respect to $\gamma 2$, the probability for geometrical summing is

$$P = \frac{1}{4\pi} (d\Omega \, \varepsilon \, T)_{E_{\gamma 3}} \qquad -4.11$$

Each summing event adds one count to $\gamma 1$ and subtracts one count from each of $\gamma 2$ and $\gamma 3$.

3). A subtraction had to be made to $\gamma 2$ for the single escape (SE) peak

of $\gamma 1$ that was included when finding its area (Appendix B). Therefore, from $\gamma 2$ there was subtracted an amount, $K_2 N_1$,

where $K_2$ = ratio of SE/FE at $E_{\gamma i}$ -4.12

$N_1$ = "true" number of counts in $\gamma 1$ .

Therefore,
$$N_1 = K_1 N_1' - P N_2$$
$$N_2 = K_1 N_2' - K_2 N_1 + P N_2 \quad \text{-4.13}$$
$$N_3 = K_1 N_3' + P N_2$$

where $N_1, N_2, N_3$ = the true number of counts in $\gamma 1$, $\gamma 2$, $\gamma 3$ after all experimental corrections have been made.

$N_1', N_2', N_3'$ = the raw counts in $\gamma 1$, $\gamma 2$, $\gamma 3$ as obtained from the fitting programs.

This set of linear equations was solved for each run. For some runs $\gamma 3$ and/or $\gamma 1$ were not analysed but the proceedure remained the same with the appropriate terms set to zero.

So far it has been implicitly assumed that the measured and corrected intensities of the desired capture transitions are not in error because of the coincidental juxtaposition with a background peak. The direct capture peaks are broadened by target thickness and exhibit a range of widths from about 15 to 70 Kev FWHM. In principle, once the peaks become broadened more than the energy resolution of the detector system (< 10 Kev FWHM), they should develop a smooth top (unless the cross section fluctuated dramatically with energy) upon which the presence of any background peaks should be evident. However, this situation is realized only for very good counting statistics per channel in the analyser. Most of the peaks dealt with here do not qualify in this respect. Any

background peaks that are a few per cent the intensity of the direct capture peaks and are present anywhere within a certain 5 - 40 Kev range would have little effect on the shape of the capture peak and would very probably be passed unnoticed.

This uncertainty in the true area of the capture peaks can be alleviated to some extent. The totality of capture spectra were inter-compared to see if in any spectra there were background peaks at energies that would cause them to coincide with the direct capture peaks of any other spectra. This survey did uncover one such background peak and resolved the anomalous cross section that had been calculated from the direct capture peak it had interfered with. This method is far from foolproof. A coincident background peak that is not present at other energies and angles can still be present in the original spectrum. It can be argued that enough is known about the direct capture cross section to know that it must vary "smoothly" with energy. Therefore, if the measured cross sections show a scatter no greater than what is consistent with the quoted errors, it is reasonable to conclude that the data is not in error from any additional uncertainties not yet corrected for.

Neglecting the possibility of this uncertainty from background peaks, the number of counts in the direct capture peaks were determined to an accuracy

from 2.0% to 10.6% for $\gamma 1$

1.0% to 3.5% for $\gamma 2$

1.0% to 1.5% (relative) for $\gamma 3$

(except for one peak in error by 6%).

## 4.2b DIRECT CAPTURE CROSS SECTIONS

Using the parameters just discussed and eqns. 3.4, 3.6, and 3.8, the direct capture differential cross sections were calculated. Table 4.3 gives the angular distributions for $\gamma 1$ and $\gamma 2$ expressed as ratios to $\gamma 3$. Table 4.4 gives the excitation data at 90° for $\gamma 1$ and $\gamma 2$.

| Mean CM Reaction Energy (Kev) ± 2 kev | Mean CM Scattering Angle (Degrees) ± 1.2° | Number of Counts | | | (dΩ ∈ T) ± 1.5 % | | | $\left(\frac{d\sigma}{d\Omega}\right)_{\gamma 1} / \left(\frac{d\sigma}{d\Omega}\right)_{\gamma 3}$ | $\left(\frac{d\sigma}{d\Omega}\right)_{\gamma 2} / \left(\frac{d\sigma}{d\Omega}\right)_{\gamma 3}$ |
|---|---|---|---|---|---|---|---|---|---|
| | | $\gamma 1$ | $\gamma 2$ | $\gamma 3$ | $E_{\gamma 1}$ | $E_{\gamma 2}$ | $E_{\gamma 3}$ | | |
| 778 | 90.3 | 746 ±10.6% | 10,364 ± 1.1% | 12,570 ± 0% | 0.0284 | 0.0422 | 0.0711 | 0.149 ±10.8% | 1.389 ± 2.4% |
| | 55.1 | 990 ± 5.3% | 10,863 ± 1.1% | 16,919 ± 1.0% | 0.0288 | 0.0435 | 0.0716 | 0.145 ± 5.8% | 1.057 ± 2.6% |
| | - 0.1 | 2097 ± 3.6% | 1,404 ± 3.9% | 30,318 ± 1.2% | 0.0258 | 0.0405 | 0.0641 | 0.172 ± 5.7% | 0.073 ± 4.6% |
| 1289 | 90.4 | 1021 ± 6.1% | 10,087 ± 1.1% | 23,047 ± 0% | 0.0201 | 0.0281 | 0.0711 | 0.157 ± 6.5% | 1.107 ± 2.4% |
| | 55.2 | 1422 ± 5.1% | 9,907 ± 1.1% | 28,840 ± 1.4% | 0.0211 | 0.0285 | 0.0716 | 0.167 ± 5.7% | 0.863 ± 2.8% |
| | 40.3 | 2127 ± 3.0% | 10,591 ± 1.1% | 43,649 ± 1.4% | 0.0217 | 0.0289 | 0.0707 | 0.159 ± 3.9% | 0.594 ± 2.8% |
| | 120.2 | 1132 ± 5.7% | 8,547 ± 1.5% | 25,725 ± 1.4% | 0.0051 | 0.0063 | 0.0157 | 0.135 ± 6.2% | 0.828 ± 3.0% |
| 1840 | 90.2 | 3034 ± 3.2% | 22,157 ± 0.7% | 48,078 ± 1.5% | 0.0175 | 0.0202 | 0.0606 | 0.219 ± 4.1% | 1.383 ± 2.3% |
| | 55.2 | 3983 ± 2.6% | 18,642 ± 0.8% | 60,764 ± 6.0% | 0.0155 | 0.0190 | 0.0645 | 0.273 ± 6.9% | 1.041 ± 6.4% |
| | 40.1 | 5010 ± 2.0% | 15,366 ± 1.0% | 63,449 ± 2.0% | 0.0164 | 0.0191 | 0.0596 | 0.287 ± 3.5% | 0.756 ± 3.1% |
| | 120.2 | 619 ± 6.0% | 3,524 ± 2.0% | 13,555 ± 0% | 0.00376 | 0.00433 | 0.01415 | 0.172 ± 6.4% | 0.850 ± 2.9% |
| 2306 | 90.2 | 1896 ± 7.4% | 12,742 ± 1.0% | 54,571 ± 0% | 0.0153 | 0.0176 | 0.0606 | 0.138 ± 7.7% | 0.804 ± 2.3% |
| | 55.2 | 3627 ± 5.8% | 13,022 ± 1.1% | 71,944 ± 1.3% | 0.0127 | 0.0157 | 0.0645 | 0.256 ± 6.3% | 0.744 ± 2.7% |
| | 40.2 | 5553 ± 3.3% | 11,073 ± 1.4% | 81,320 ± 1.4% | 0.0144 | 0.0166 | 0.0596 | 0.283 ± 4.2% | 0.489 ± 2.9% |
| | 120.2 | 939 ± 6.9% | 3,615 ± 2.0% | 17,900 ± 1.4% | 0.00336 | 0.00379 | 0.01415 | 0.221 ± 7.3% | 0.754 ± 3.2% |

Table 4.3 : $^{16}O(p,\gamma)^{17}F$ - angular distribution data.

| Mean C.M. Reaction Energy (Kev) ± 2 kev | Lab. Differential Cross Section ($\mu$b/ster) at 90° | | | |
|---|---|---|---|---|
| | $\gamma_1$ | $\gamma_2$ | $\gamma_1/\gamma_2$ | Total |
| 795 | X | 0.080 ±0.004 | X | X |
| 1024 | 0.038 ±0.002 | 0.198 ±0.009 | 0.185 ±0.013 | 0.236 ±0.009 |
| 1029 | 0.036 ±0.003 | 0.183 ±0.007 | 0.199 ±0.016 | 0.219 ±0.008 |
| 1288 | 0.046 ±0.003 | 0.306 ±0.010 | 0.150 ±0.011 | 0.352 ±0.010 |
| 1572 | 0.067 ±0.006 | 0.470 ±0.025 | 0.142 ±0.014 | 0.537 ±0.028 |
| 1836 | 0.104 ±0.006 | 0.602 ±0.019 | 0.172 ±0.011 | 0.706 ±0.020 |
| 2404 | 0.178 ±0.008 | 0.903 ±0.029 | 0.197 ±0.011 | 1.081 ±0.030 |

Table 4.4 : $^{16}O(p,\gamma)^{17}F$ - differential cross section data.

# CHAPTER 5

## COMPARISON WITH THEORY AND DISCUSSION

Before the direct capture data can be compared to theoretical calculations they must be corrected for the effects introduced by the finite size of the Ge(Li) detector. This correction is required for both the angular distribution and the differential cross section measurements.

One way of making this correction is to introduce the "Rose (1953) smoothing factors", $Q_\ell$ , for the detector (Appendix B), into the following expression for the experimental angular distribution at a given energy

$$W_{exp}(\theta) = \sum_\ell A_\ell Q_\ell P_\ell[\cos(\theta + \theta_o)] \qquad - 5.1$$

and then adjusting the unknown amplitudes, $A_\ell$ , and, if required, the offset angle, $\theta_o$ , to give a least squares best fit to the experimental data. The corrected angular distribution is then given by

$$W_{corrected}(\theta) = \sum_\ell A_\ell P_\ell(\cos\theta) \qquad - 5.2$$

which can be compared with the theoretical predictions.

The number of terms required in the Legendre polynomial expansion of the angular distribution is limited by various selection rules. For the common case of transitions between states of well defined parity, $\ell$ is limited to even values, the maximum value being the smallest of $2I_1$, $2I_2$ and 2L where $I_1$ and $I_2$ are the spins of the initial and final states and L is the multipolarity of the gamma ray transition between the states. For direct radiative capture, however, the initial continuum state contains all angular momentum components, both even and odd, and does not

have a well defined parity. Therefore, there may be coherent transitions to a given final state from initial states of different parity which will interfere with each other, introducing odd $\ell$ values into the angular distributions, and leading to a distribution that is asymmetric about 90°. On the basis of direct capture calculations of Donnelly (1967), and Chow (1973),as well as from penetrability arguments for the energies considered in this work, the maximum $\ell$ value expected is 4, arising from a small amount of d-wave capture with E2 electromagnetic transitions to both the $2s^{+}_{\frac{1}{2}}$ and $1d^{+}_{5/2}$ final states.

An attempt was made to generate corrected angular distributions by least square fitting the limited amount of angular distribution data, as described above, using a computer program developed by Olivo (1968). However, it was not possible to arrive at an unambiguous set of amplitudes, $A_\ell$, which changed smoothly with energy. In addition some solutions with minimum $\chi^2$ were not physically reasonable. It was clear that with measurements at only three angles at 0.778 Mev and four angles at each of the three higher energies there were not enough data points to produce unambiguous angular distributions. In particular, the lack of data at 0° for all but the run at the lowest energy, where the statistical accuracy was low, left considerable leeway for ambiguity. It was difficult to get reliable experimental data around 0° because of the large background in the direction of the beam, particularly at the higher energies, and because of the very low cross section for $\gamma 2$ at forward angles.

A qualitative inspection of the $\gamma 1$ angular distribution for transitions to the ground state shows a minimum at 90° rather than the maximum given by Donnelly (1967). However Donnelly's calculation based

on a direct radiative capture model using a square well neglected the separation of the initial state angular momentum components into their two $j = \ell \pm \frac{1}{2}$ total angular momentum components. Donnelly also did a calculation using a Saxon-Woods potential with a spin-orbit term which necessarily incorporated the correct splitting of the angular momentum components of the partial waves, but as he did not provide angular distribution results for this calculation, the discrepancy was not noticed. As a result Chow (1973) repeated the angular distribution calculations using the Saxon-Woods potential with improved potential parameters and with the spin-orbit term which automatically requires the incorporation of the correct phase between the two total angular momentum components of each incoming partial wave. This lead to qualitative agreement with the observed angular distribution for $\gamma_1$. The main factor contributing to this agreement was not the spin-orbit term itself, which was necessary to provide a good fit to the scattering data and binding energies, but the separation of the incoming partial waves into total angular momentum components.

As a result of the inadequacy of the direct approach for correcting the observed angular distributions for solid angle effects, an alternative approach was adopted in order to compare the experimental results with the theoretical predictions. The detector Q values, or solid angle smoothing factors (Appendix B), were introduced into the theoretical differential cross sections given by Chow (1973) so that a statistical comparison could be made between the smoothed theoretical angular distributions and the experimental ones. To introduce the Q values, the theoretical angular distributions, $W_{th}(\theta)$, were expanded in a Legendre polynomial series in

which the terms included were those given by the theoretical calculations, namely $\ell$ = 0, 1, 2, 3 terms for $\gamma 1$ and $\ell$ = 0, 1, 2, 3, 4 terms for $\gamma 2$.

The angular distribution data, obtained as the relative number of counts (Table 4.3) at each angle, were first normalized to the smoothed theoretical angular distributions by arbitrary scale factors which were determined for each transition at each energy by minimizing expressions of the form

$$\sum_{i=1}^{N} \frac{\left[ K W_{data}(\theta_i) - W'_{th}(\theta_i) \right]^2}{W'_{th}(\theta_i)} \qquad - 5.3$$

where K = arbitrary scale factor

i = label for angles at which data were taken

$W_{data}(\theta_i)$ = angular distribution data

$W'_{th}(\theta_i)$ = smoothed theoretical angular distribution.

The coefficients, $A_\ell$, of the Legendre polynomial expansion of the theoretical angular distributions, $W_{th}(\theta)$, the detector Q values, $Q_\ell$, and the resulting Legendre polynomial coefficients, $B_\ell = A_\ell Q_\ell$, of the smoothed theoretical angular distributions, $W'_{th}(\theta)$, are given in Table 5.1. The arbitrary scale factors, K, and the resulting normalized experimental angular distributions, $W_{exp}(\theta) = K W_{data}(\theta)$, are given in Table 5.2.

$W'_{th}(\theta)$ and $W_{exp}(\theta)$ are compared to each other in Figs. 5.1 to 5.4. The angles at which the $\gamma 1$ angular distribution has a minimum and the $\gamma 2$ angular distribution has a maximum are also shown. From these figures it can be seen that there is qualitative agreement between the data and theory.

A more quantitative measure of the agreement between theory and

| Energy (kev) | γ | $A_o$ | $A_1$ | $A_2$ | $A_3$ | $A_4$ |
|---|---|---|---|---|---|---|
| 778 | 1 | 0.00866 | 0.000438 | 0.00229 | -0.000240 | |
| | 2 | 0.0572 | 0.00413 | -0.0571 | -0.00413 | -0.0000538 |
| 1289 | 1 | 0.0479 | 0.00353 | 0.0165 | -0.00160 | |
| | 2 | 0.210 | 0.0180 | -0.209 | -0.0180 | -0.000265 |
| 1840 | 1 | 0.130 | 0.0120 | 0.0531 | -0.00496 | |
| | 2 | 0.420 | 0.0460 | -0.419 | -0.0460 | -0.000895 |
| 2306 | 1 | 0.229 | 0.0242 | 0.103 | -0.00960 | |
| | 2 | 0.581 | 0.0714 | -0.579 | -0.0716 | -0.00156 |

| γ | $Q_o$ | $Q_1$ | $Q_2$ | $Q_3$ | $Q_4$ |
|---|---|---|---|---|---|
| 1 | 1.000 | 0.968 | 0.907 | 0.820 | 0.714 |
| 2 | 1.000 | 0.967 | 0.903 | 0.814 | 0.704 |

| Energy (kev) | γ | $B_o$ | $B_1$ | $B_2$ | $B_3$ | $B_4$ |
|---|---|---|---|---|---|---|
| 778 | 1 | 0.00866 | 0.000424 | 0.00207 | -0.000197 | |
| | 2 | 0.0572 | 0.00399 | -0.0516 | -0.00336 | -0.0000271 |
| 1289 | 1 | 0.0479 | 0.00342 | 0.0150 | -0.00131 | |
| | 2 | 0.210 | 0.0174 | -0.189 | -0.0146 | -0.000187 |
| 1840 | 1 | 0.130 | 0.0116 | 0.0482 | -0.00406 | |
| | 2 | 0.420 | 0.0445 | -0.379 | -0.0374 | -0.000630 |
| 2306 | 1 | 0.229 | 0.0235 | 0.0934 | -0.00783 | |
| | 2 | 0.581 | 0.0691 | -0.523 | -0.0583 | -0.00110 |

Table 5.1 : Theoretical angular distribution coefficients $A_\ell$ and $B_\ell$ and detector Q factors $Q_\ell$.

| C.M. Energy (kev) | γ | K | θ | $W_{exp}(\theta)$ |
|---|---|---|---|---|
| 778 | 1 | 0.0586 | 90 | 0.00872 |
| | | | 55 | 0.00849 |
| | | | 0 | 0.0101 |
| | 2 | 0.0594 | 90 | 0.0825 |
| | | | 55 | 0.0628 |
| | | | 0 | 0.00433 |
| 1289 | 1 | 0.3046 | 120 | 0.0411 |
| | | | 90 | 0.0478 |
| | | | 55 | 0.0509 |
| | | | 40 | 0.0484 |
| | 2 | 0.2653 | 120 | 0.220 |
| | | | 90 | 0.294 |
| | | | 55 | 0.229 |
| | | | 40 | 0.158 |
| 1840 | 1 | 0.5384 | 120 | 0.0926 |
| | | | 90 | 0.118 |
| | | | 55 | 0.147 |
| | | | 40 | 0.155 |
| | 2 | 0.4477 | 120 | 0.381 |
| | | | 90 | 0.619 |
| | | | 55 | 0.466 |
| | | | 40 | 0.338 |
| 2306 | 1 | 1.0013 | 120 | 0.221 |
| | | | 90 | 0.138 |
| | | | 55 | 0.256 |
| | | | 40 | 0.283 |
| | 2 | 0.8886 | 120 | 0.700 |
| | | | 90 | 0.714 |
| | | | 55 | 0.661 |
| | | | 40 | 0.434 |

Table 5.2 : Normalized experimental angular distributions.

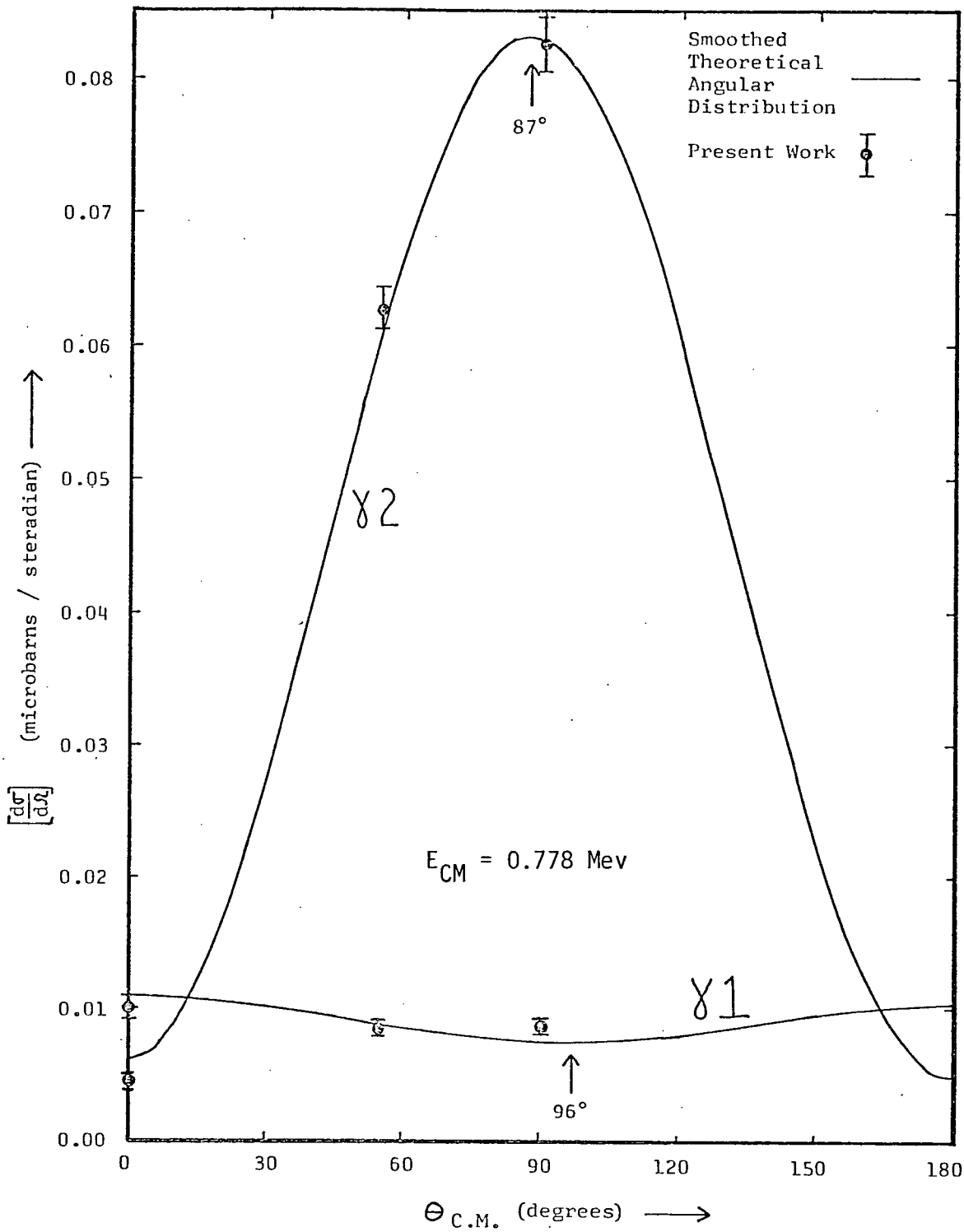


Figure 5.1: $^{16}O(p,\gamma)^{17}F$ - comparison of angular distribution data to smoothed angular distribution functions.

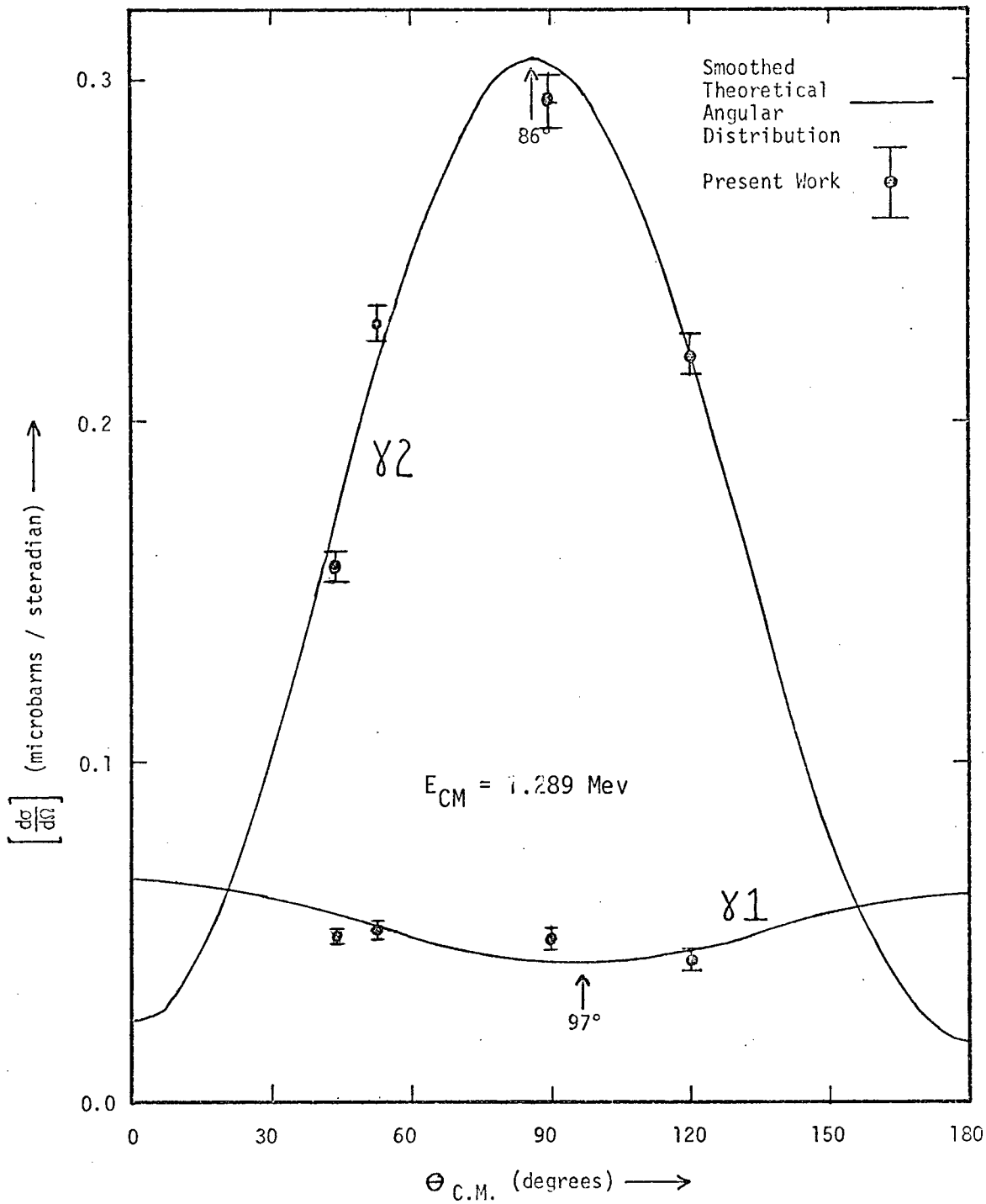


Figure 5.2 : $^{16}O(p, \gamma)^{17}F$ - comparison of angular distribution data to smoothed angular distribution functions.

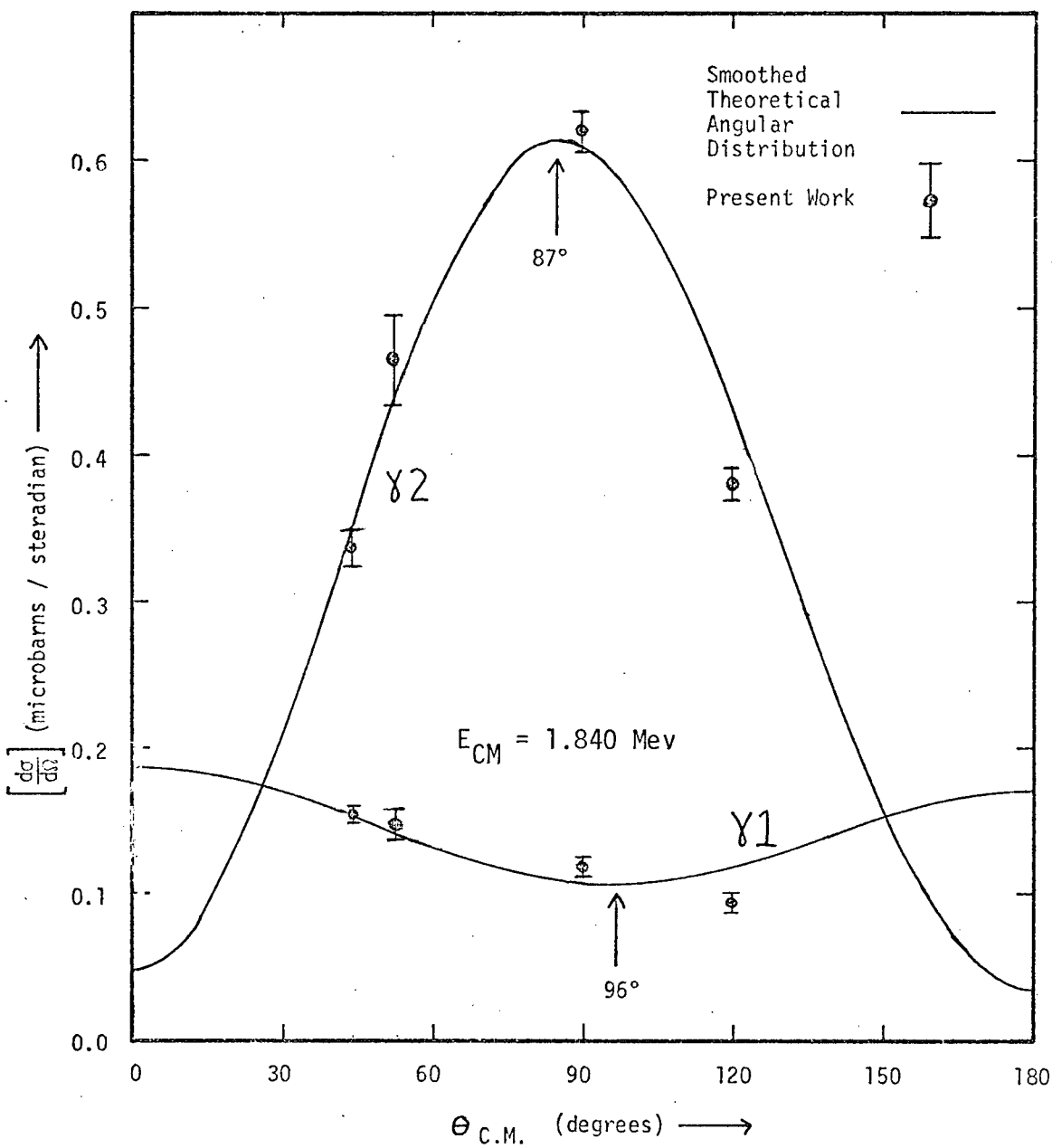


Figure 5.3 : $^{16}O(p, \gamma)^{17}F$ - comparison of angular distribution data to smoothed angular distribution functions.

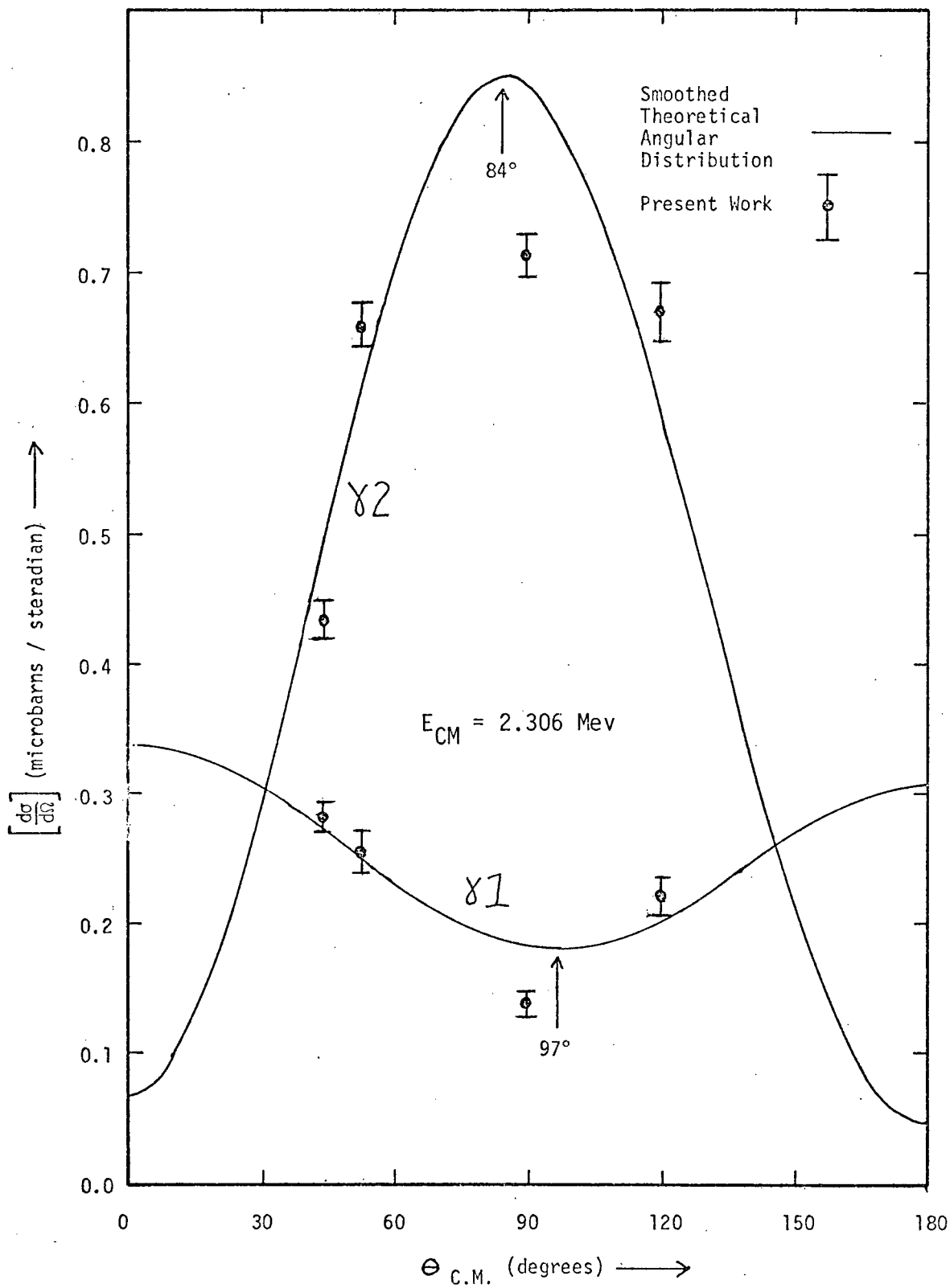


Figure 5.4 : $^{16}O(p,\gamma)^{17}F$ - comparison of angular distribution data to smoothed angular distribution functions.

experiment can be made by computing, for each angular distribution, expressions of the form

$$\sum_{i=1}^{N} \frac{\left[W'_{th}(\theta_i) - W_{exp}(\theta_i)\right]^2}{\left[\delta W_{exp}(\theta_i)\right]^2} \qquad - 5.4$$

where i = label for angles at which angular distribution data were taken

$\delta W_{exp}(\theta_i)$ = error in experimental data (Table 4.3).

Although this comparison is similar to the goodness of fit expressed by the usual $\chi^2$ test, the theory does not contain any adjustable parameters which can be varied to minimize the $\chi^2$ value. The values obtained from expression 5.4, therefore, serve only as a reference for the comparison of the data to the theory. Introducing an offset angle, $\theta_0 \leq \pm 3°$, as an adjustable parameter to allow for uncertainties in the experimental angle, improved agreement a little but did not alter the qualitative conclusions.

Further insight into the information contained in the data can be obtained by considering the individual components that comprise the calculated theoretical angular distributions. By observing the changes in the values obtained from expression 5.4 when the data was compared to calculated angular distributions which exclude contributions from various terms, one can study whether there is any evidence in the limited amount of experimental data for particular transitions that are predicted by the direct capture theory.

Such an analysis shows that, in the angular distribution for $\gamma 2$, omitting the E1/E2 interference terms, and hence eliminating the forward peaking which is evident from Figs. 5.1 to 5.4, decreases the quality of fit and causes expression 5.4 to increase drastically (for instance from 1 to 15 at 1.289 Mev). However, omitting the small E2 terms has very

little effect.

Therefore, the data indicate that $\gamma 2$ is predominantly p-wave capture (E1 transition, $\sin^2 \theta$ distribution and $A_0$ and $A_2$ coefficients), but also contains a small amount of d-wave capture (introducing E1/E2) interference terms, with asymmetry about 90° and non-zero $A_1$ and $A_3$ coefficients). Although it is doubtful that the data are sensitive to the small $A_4$ coefficient, the presence of E2 transitions is definitely indicated by the sensitivity of the data to the E1/E2 interference terms.

For the $\gamma 1$ angular distribution, the qualitative agreement shown in Figs. 5.1 to 5.4 supports the assignment of p and f-wave capture with E1/E1 interference between the p and f partial waves that produces a minimum rather than a maximum at 90°. The data, however, does not confirm an asymmetry about 90°, which would arise from interference between terms of opposite parity, since omitting the $p_{3/2} - d_{5/2} / s_{1/2} - d_{5/2}$ (E1/E2) interference term considered by Chow (1973) causes no noticeable change in expression 5.4 and leaves the presence of the $A_1$ and $A_3$ coefficients unspecified. This suggests there is relatively little s-wave capture with E2 emission to the ground state.

Corrections to the absolute differential cross section data at 90° (Table 4.4) for the finite solid angle subtended by the Ge(Li) detector were based upon the empirically determined detector size (Fig. B.3) and the theoretical angular distributions (Chow, 1973), $W_{th}(\theta)$. Correction factors were obtained at each of the four energies for which angular distribution data were taken by numerically integrating expressions of the form

$$\frac{\int k(\beta)\, F(\beta)\, W_{th}(\theta)\, d\theta}{\int k(\beta)\, F(\beta)\, d\theta} \qquad - 5.5$$

where $\beta$ = angle from detector axis

$F(\beta)$ = detector mapping function (Appendix B)

$K(\beta)$ = the geometrical weighting factor, proportional to the solid angle between $\beta + d\beta$ and $\beta - d\beta$, that absorbs the integration over the azimuthal angle, $\phi$; since $F(\beta)$ is a linear scan in the $\theta$ direction only.

These corrections have a small dependence on the bombarding energy, due to the small change in the theoretical angular distributions with energy, and were interpolated to find the corrections at the energies at which cross section measurements were made. For center of mass energies from 0.795 to 2.404 Mev, the correction factors that multiplied the differential cross section measurements (Table 4.4) varied from 1.066 to 1.072 for $\gamma 2$ and from 0.972 to 0.949 for $\gamma 1$. The error in this solid angle correction, due to errors in determining $F(\beta)$ and to uncertainties ($90° \pm 3°$) in the angle of the cross section measurements, is estimated to be less than 1%.

The measured differential cross sections, after being corrected, were converted to total cross sections assuming the validity of the theoretical angular distributions. The results are given in Table 5.3.

Fig. 5.5 shows the experimental and theoretical differential cross sections at 90° for $\gamma 1$ and $\gamma 2$. Considering that there has been no renormalization between theory and experiment once the continuum and bound state wave functions for the direct capture had been determined (by fitting scattering data and binding energies of ground and first excited states of $^{17}F$), the agreement is very satisfactory.

The total cross sections for $\gamma 1$ and $\gamma 2$ are shown in Figs. 5.6 and 5.7 along with results of earlier measurements, all of which have significantly larger errors than the present results. Fig. 5.7 shows, in addition, the theoretical results obtained by Donnelly (1967) for a square well model without a spin-orbit term (Model I) and for a Saxon-Woods potential with

| Mean C.M. Energy (Mev) ± 2 kev | γ1 | | γ2 | | Branching Ratios | |
|---|---|---|---|---|---|---|
| | $(d\sigma/d\Omega)$ Lab., 90° μb/ster. | σ Total Lab. μbarns. | $(d\sigma/d\Omega)$ Lab., 90° μb/ster. | σ Total Lab. μbarns. | $\frac{(d\sigma/d\Omega)_{\gamma 1}}{(d\sigma/d\Omega)_{\gamma 2}}$ | $\frac{(\sigma \text{ Total})_{\gamma 1}}{(\sigma \text{ Total})_{\gamma 2}}$ |
| 0.795 | X | X | 0.086 ± 0.004 | 0.73 ± 0.03 | X | X |
| 1.024 | X | X | 0.212 ± 0.009 | 1.78 ± 0.08 | X | X |
| 1.029 | X | X | 0.195 ± 0.007 | 1.64 ± 0.06 | X | X |
| 1.288 | 0.046 ± 0.003 | 0.69 ± 0.05 | 0.337 ± 0.010 | 2.83 ± 0.08 | 0.135 ± 0.010 | 0.245 ± 0.018 |
| 1.572 | 0.066 ± 0.006 | 1.01 ± 0.09 | 0.521 ± 0.025 | 4.36 ± 0.21 | 0.127 ± 0.013 | 0.231 ± 0.024 |
| 1.836 | 0.096 ± 0.006 | 1.52 ± 0.10 | 0.628 ± 0.020 | 5.27 ± 0.16 | 0.153 ± 0.010 | 0.289 ± 0.019 |
| 2.404 | 0.164 ± 0.008 | 2.66 ± 0.13 | 0.940 ± 0.030 | 7.88 ± 0.25 | 0.175 ± 0.010 | 0.338 ± 0.019 |

Table 5.3 : $^{16}O(p, \gamma)^{17}F$ cross section measurements after correction for detector size.

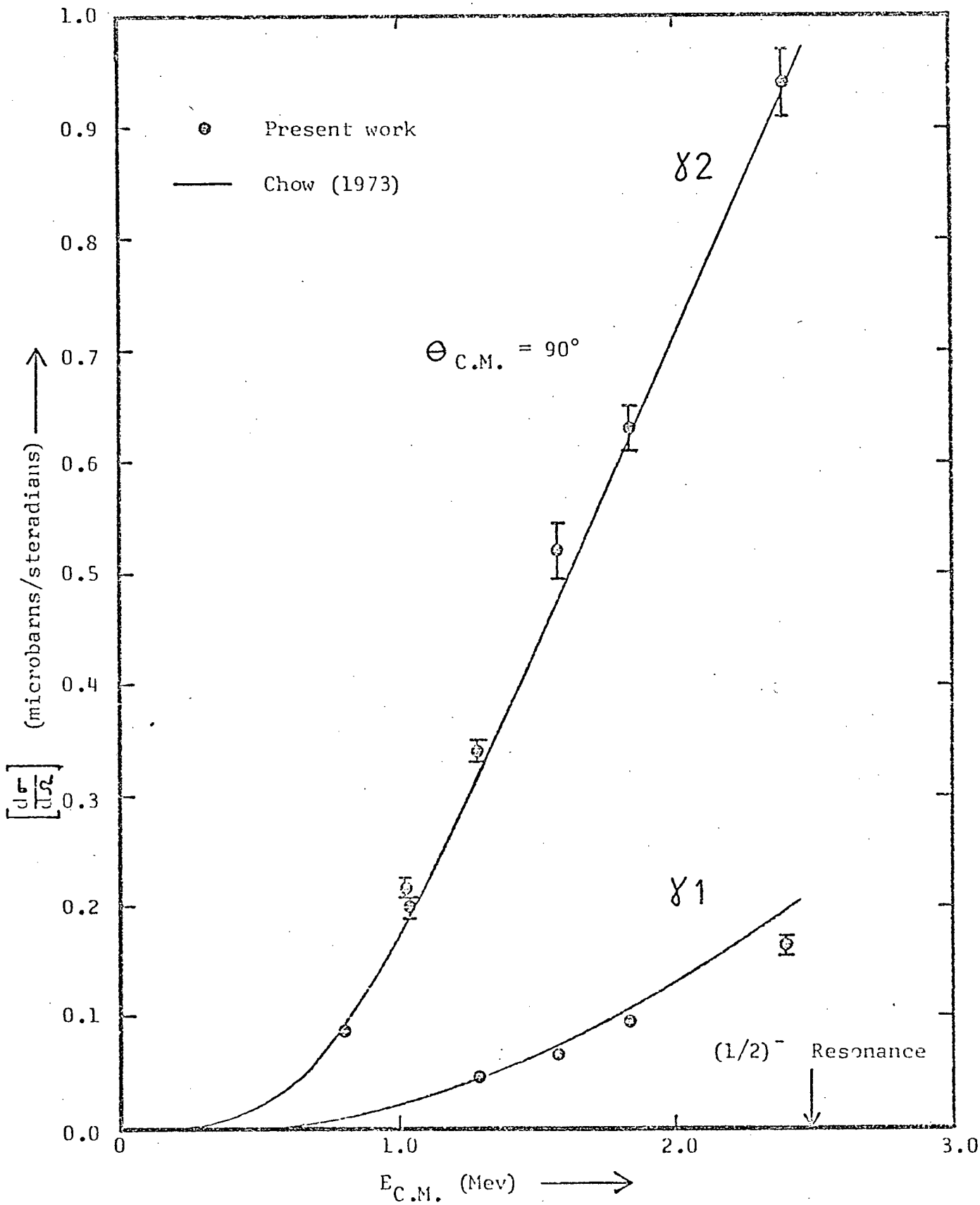


Figure 5.5 : $^{16}O(p,\gamma)^{17}F$ - differential cross section at 90° for γ1 and γ2 transitions.

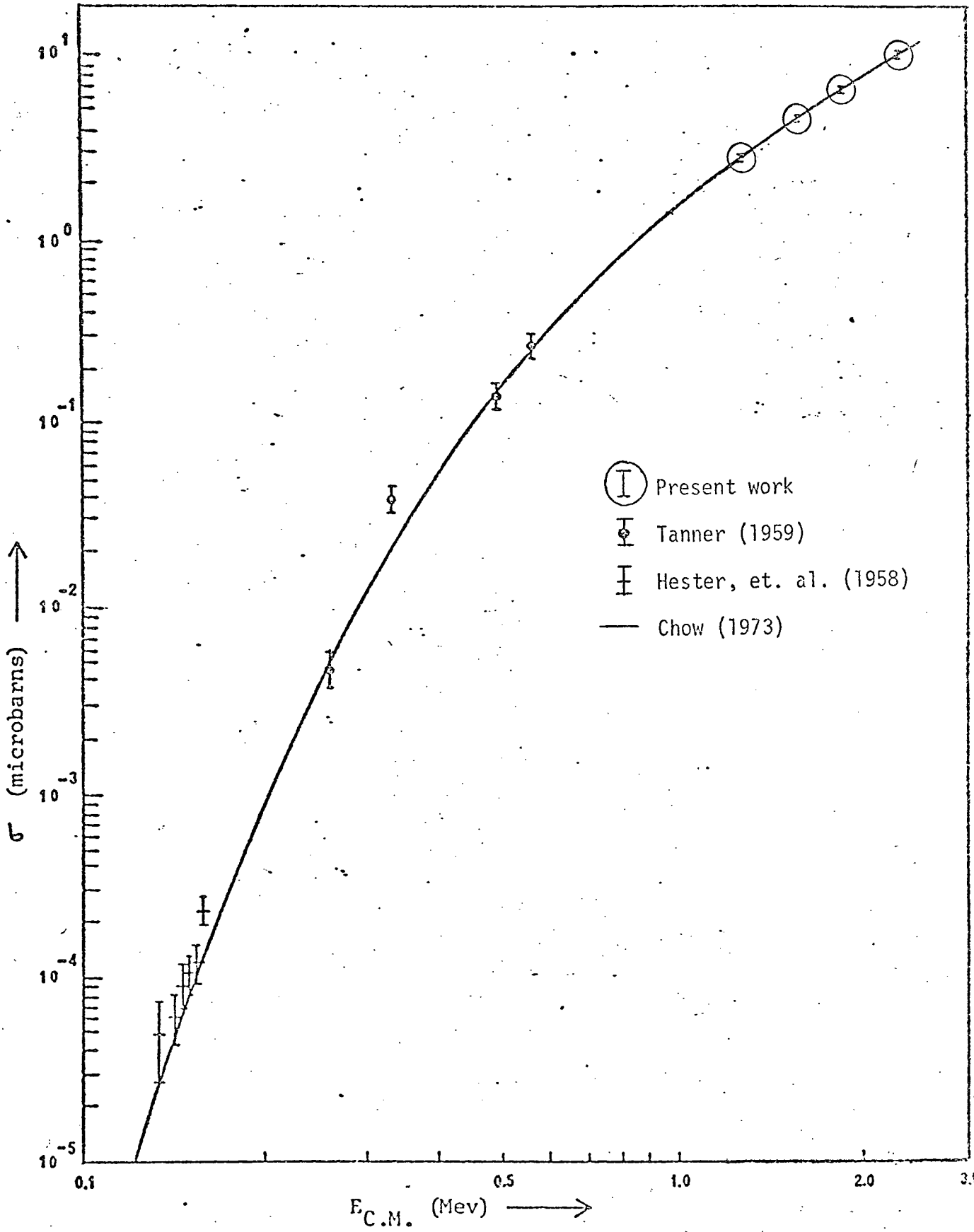


Figure 5.6 : $^{16}O(p,\gamma)^{17}F$ - total cross section.

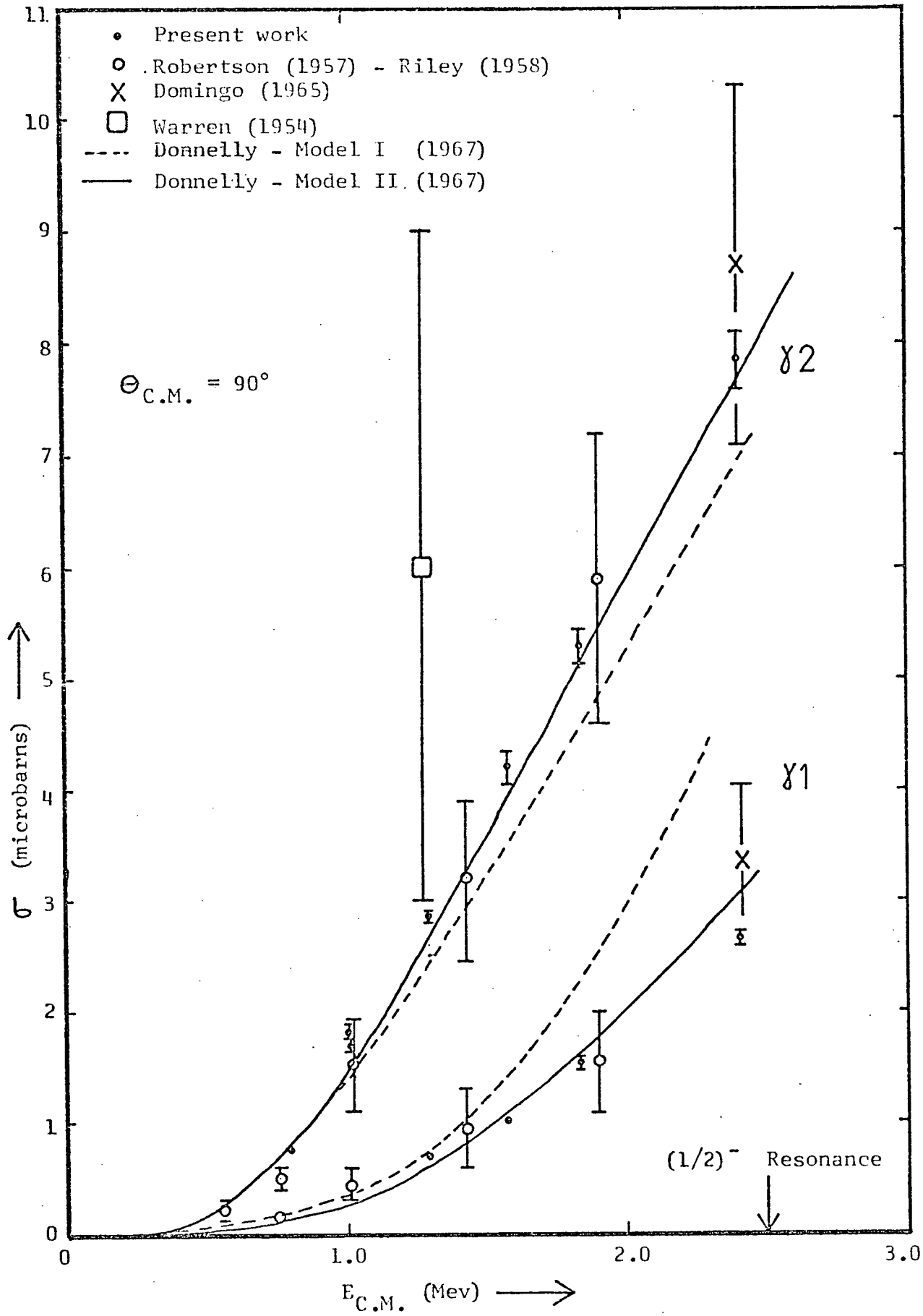


Figure 5.7 : $^{16}O(p,\gamma)^{17}F$ - total cross sections for γ1 and γ2 transitions.

a spin-orbit term (Model II). The branching ratios for $\gamma 1$ to $\gamma 2$ for both total cross sections and differential cross sections at 90° are shown as a function of energy in Fig. 5.8.

The present cross section data agree with the most recent theoretical calculations of Chow (1973) to within 5% (Fig. 5.5), and the present angular distribution data are consistent with the theoretical angular distributions of Chow (1973) (Figs. 5.1 to 5.4) even though comparison here can be only qualitative because of the limited amount of angular distribution data taken and the inability to generate experimental angular distributions from it. In addition, it is now possible to differentiate between the two models of Donnelly (1967), the present data favoring the calculations based on Model II over Model I (Fig. 5.7). At the time Donnelly's calculations were done, the available experimental data were not of sufficient accuracy to distinguish one model from the other. The differences are small, as would be expected, since the cross section is relatively insensitive to the particular model used.

As mentioned in Chapter I, the $^{16}O(p, \gamma)^{17}F$ reaction is of significance in astrophysics through its role in the CNO bi-cycle, and a determination of its rate at stellar energies is therefore of considerable interest.

For a discussion of nuclear reaction rates in stellar processes the cross section is usually expressed as

$$\sigma(E) = \frac{S(E)}{E} e^{-2\pi\eta} \qquad - 5.6$$

where, $\eta = Z_1 Z_2 e^2/\hbar v$ for particles of atomic number $Z_1$ and $Z_2$ interacting with relative velocity v and center of mass energy E, and $e^{-2\pi\eta}$ is the coulomb factor corresponding to the probability of finding an s-wave

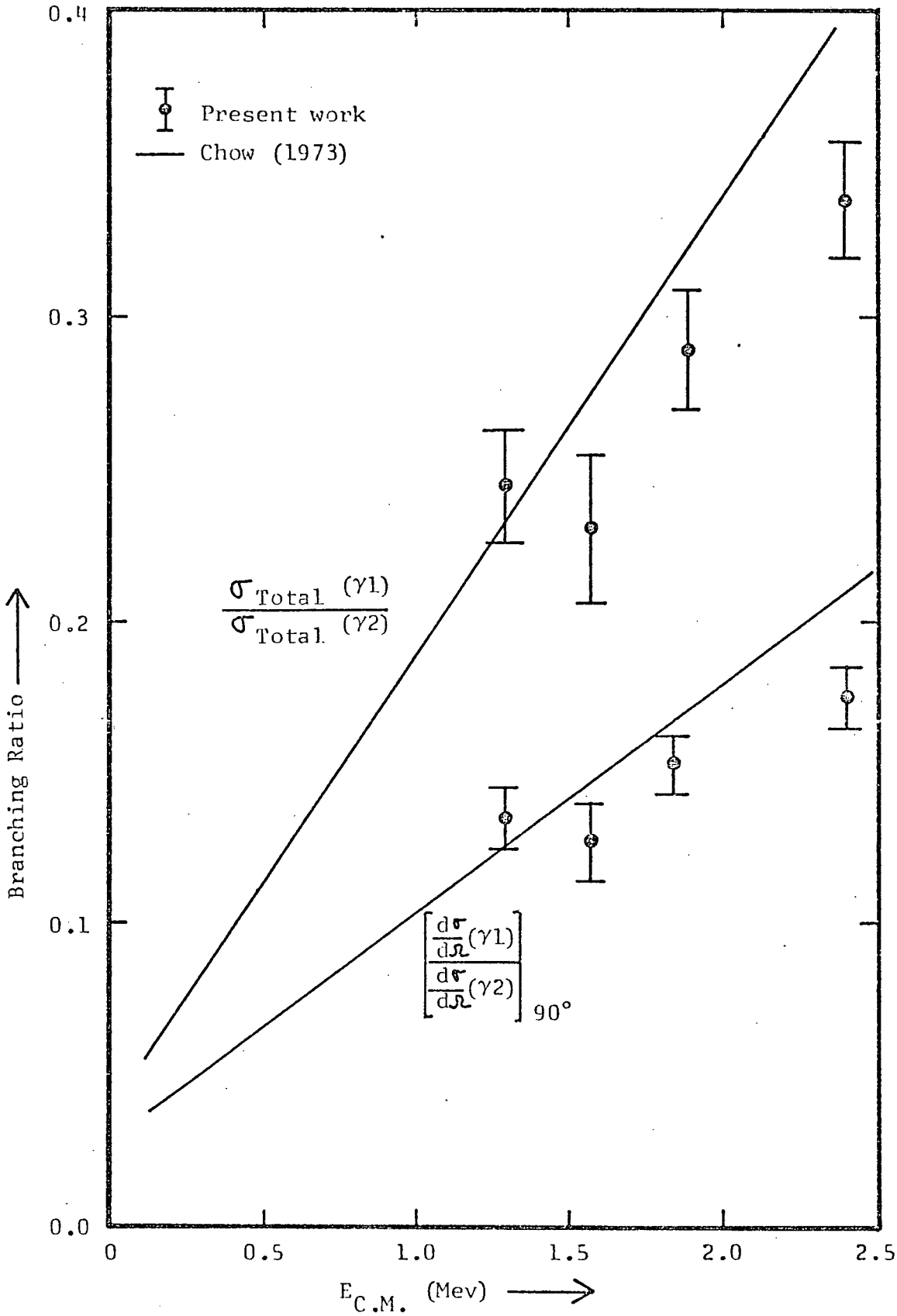


Figure 5.8 : $^{16}O(p,\gamma)^{17}F$ - $\gamma 1/\gamma 2$ branching ratios for total cross section and for differential cross section at 90°.

particle at the origin in the presence of coulomb forces, $E^{-1}$ is the energy dependence associated with the de Broglie wavelength of the incident particle, usually expressed by the factor $\lambda^2$, and S, the astrophysical S-factor, is proportional to the nuclear matrix element. The S-factor can be thought of as the "sticking factor" or the probability of capture once the incident particle reaches the nuclear surface. Writing the cross section in this way separates out the explicit energy dependence associated with the exterior wave functions from the unknown interior nuclear matrix element which is incorporated in the S-factor. As a first approximation, S is often assumed to be independent of energy at low energies.

The rates of non-resonant charged particle reactions that participate in stellar processes are proportional to the product of the energy dependent cross sections and the velocities of the particles, averaged over the Maxwell-Boltzman distribution of relative velocities. This leads to a bell-shaped energy dependence whose maximum, the "Gamow Peak", is at an energy considerably higher than the mean thermal energy characteristic of the temperature. For the two temperatures 15 and 30 x $10^6$ °K, that cover the range of temperatures where the CNO bi-cycle is important, the reaction rates for direct capture of protons by $^{16}O$ have their maximum values at 29 and 46 Kev with FWHM's of 18 and 21 Kev respectively. Even at 50 Kev, the cross section is of the order of 2 x $10^{-16}$ barns, a value which is out of reach of laboratory measurements.

Consequently, the cross section at stellar energies can only be determined by theoretical extrapolation from measurements at higher energies. The role of experimental measurements, therefore, is twofold; one to provide an accurate normalization for the extrapolation and two to provide

confidence in the validity of the extrapolation by testing the theoretical model. This can be done by comparing the experimental measurements with model predictions for the normalization, energy dependence and angular distribution of the cross sections.

The S-factor is shown versus energy in Fig. 5.9 and Table 5.4. Theoretical calculations (Chow, 1973) based upon the direct capture model with the present elastic scattering data used to determine the initial continuum states yields an extrapolated value for the total S-factor of 8.83 Kev-barns at 10 Kev center of mass energy. The large energy dependence of the S-factor for $\gamma 2$, in particular its dramatic increase with decreasing energy at low energies, arises from the low binding energy of the $\frac{1}{2}+$ first excited state. Consequently, the $^{16}O(p, \gamma)^{17}F$ reaction rate at thermal energies is determined almost entirely by direct capture to this state.

The lowest energy cross section measurements are those of Hester, et al. (1958) in the remarkably low energy range from 140 to 170 Kev. Although these measurements have large errors, and cannot give an accurate extrapolation of the S-factor to thermal energies or test detailed features of the direct capture model because they are restricted to total cross section measurements, they do clearly confirm the increase in S at low energies as predicted by the theory.

The present measurements are made at higher energies where the much larger cross sections allow the $\gamma$ rays following capture to each state in $^{17}F$ to be observed directly and allow the measurements to be made with greater precision. They provide a sensitive test of the direct capture calculations for the $^{16}O$ + proton system, on which the calculation of the

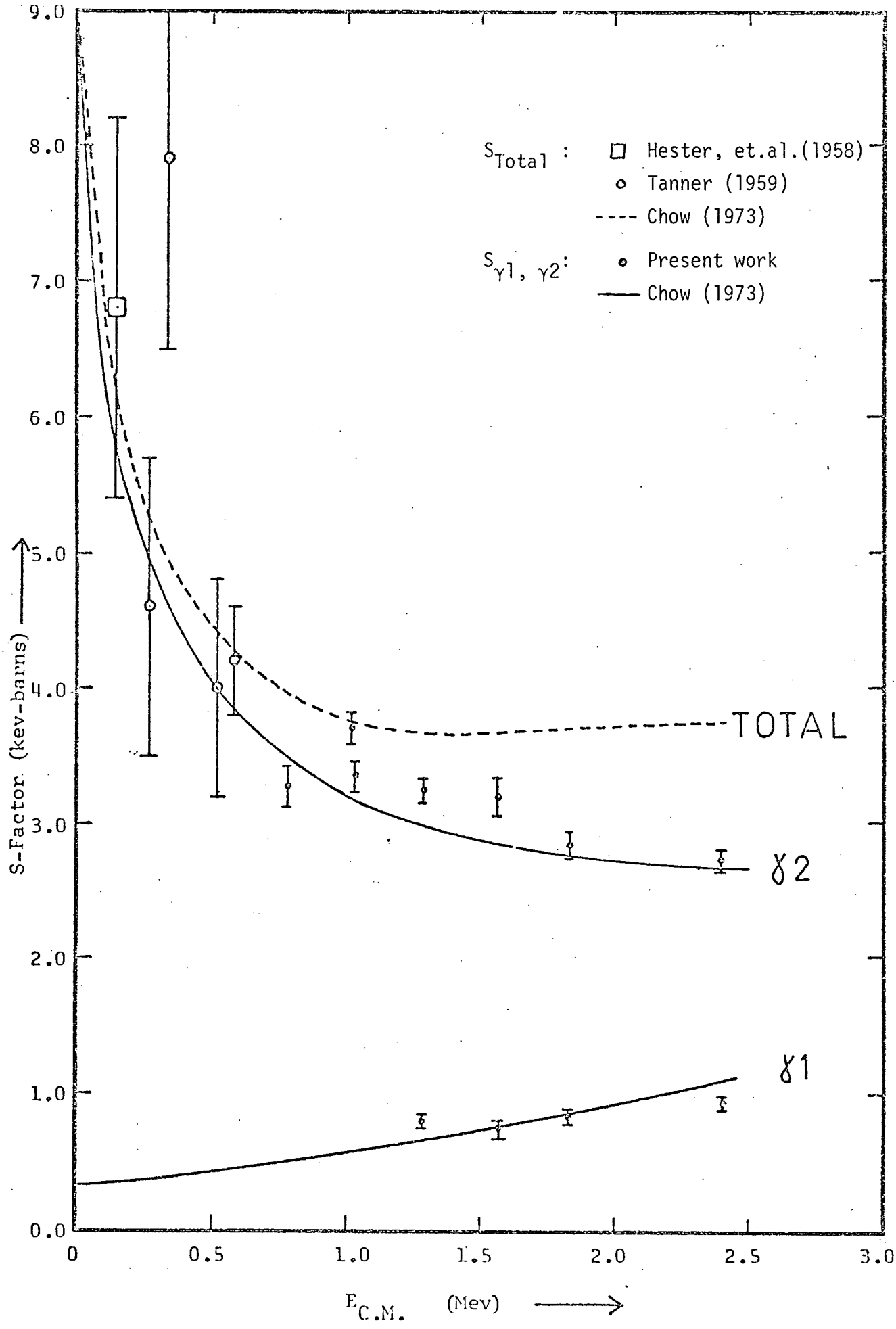


Figure 5.9 : $^{16}O(p,\gamma)^{17}F$ - Astrophysical S - Factor.

| C. M. Proton Energy (kev) | S - Factor (kev-barns) | | | | | |
|---|---|---|---|---|---|---|
| | Theoretical (Chow 1973) | | | Experimental (present work) | | |
| | $\gamma_1$ | $\gamma_2$ | Total | $\gamma_1$ | $\gamma_2$ | Total |
| 10 | 0.328 | 8.498 | 8.826 | | | |
| 40 | 0.333 | 7.659 | 7.992 | | | |
| 200 | 0.369 | 5.231 | 5.601 | | | |
| 500 | 0.447 | 3.999 | 4.445 | | | |
| 580 | 0.470 | 3.884 | 4.354 | | | |
| 778 | 0.527 | 3.478 | 4.005 | | | |
| 795 | | | | | 3.27±0.15 | |
| 1000 | 0.595 | 3.165 | 3.760 | | | |
| 1024 | | | | | 3.70±0.12 | |
| 1029 | | | | | 3.35±0.12 | |
| 1288 | | | | 0.79±0.05 | 3.24±0.09 | 4.03±0.10 |
| 1289 | 0.689 | 3.010 | 3.699 | | | |
| 1500 | 0.762 | 2.957 | 3.719 | | | |
| 1572 | | | | 0.74±0.07 | 3.20±0.15 | 3.94±0.17 |
| 1836 | | | | 0.82±0.05 | 2.85±0.09 | 3.67±0.10 |
| 1840 | 0.884 | 2.848 | 3.733 | | | |
| 2000 | 0.944 | 2.789 | 3.733 | | | |
| 2306 | 1.062 | 2.691 | 3.754 | | | |
| 2404 | | | | 0.92±0.05 | 2.73±0.09 | 3.65±0.10 |

Table 5.4 : Theoretical and experimental astrophysical S-Factors.

S-factor rests, and give a degree of confidence in the extrapolated value of the S-factor that was not possible before.

Using the theoretical calculations to define the energy dependence of the S-factor for the transitions to each state in $^{17}F$, the theoretical cross sections given by the curves of Fig. 5.9 can be normalized to give a least square fit to experimental measurements by introducing scale factors of 1.05 for $\gamma 2$ and 0.93 for $\gamma 1$. The error associated with this final result, normalized to the experimental data, can be expressed as

$$\epsilon_{Total} = \sqrt{\epsilon^2 + \frac{1}{N}\sum_{i=1}^{N}(\Delta\epsilon_i)^2} \qquad - 5.7$$

where $\epsilon$ = the systematic error, arising primarily from the calibration of the Ge(Li) detector

$\Delta\epsilon_i$ = the error (primarily statistical) associated with the determination of individual cross sections as a function of energy.

A reasonable value of $\epsilon$ is ± 2% (Section 4.2a). Values for $\Delta\epsilon_i$ can be obtained from the differential cross section data given in Table 4.4 (after removing the contribution due to $\epsilon$ which is included in the error listed there). Using these values, Eqn. 5.7 gives $\epsilon_{Total}$ = ± 6.8% for $\gamma 1$ and ± 4.1% for $\gamma 2$.

If no further error is introduced by the extrapolation to thermal energies, assuming the validity of the energy dependence of S as given by the theory (a reasonable assumption considering the good agreement between theory and experiment), then expressions for the S-factors, for each capture transition, valid for energies below 200 Kev are

$$S_{(1/2^+ \text{ state})}(E) = (9.245 - 0.0329E + 0.00007E^2) \pm 4.1\% \text{ Kev-barns}$$

$$S_{(5/2^+ \text{ state})}(E) = (0.302 + 0.0002E) \pm 6.8\% \text{ Kev-barns.}$$

BIBLIOGRAPHY

F. Ajzenberg-Selove, Nucl. Phys. A166, 1 (1971).

F. Ajzenberg-Selove, Nucl. Phys. A190, 1 (1972).

A. Aladjem and D.G. Brandon, J. Vac. Sci. Technol. 6, 635 (1969).

G.M. Bailey and D.F. Hebbard, Nucl. Phys. 46, 529 (1963a).

G.M. Bailey and D.F. Hebbard, Nucl. Phys. 49, 666 (1963b).

S. Bashkin and R.R. Carlson, Phys. Rev. 97, 1245 (1955).

H. Bethe, Phys. Rev. 55, 434 (1939).

R.R. Carlson, C.C.Kim, J.A. Jacobs and A.C.L. Barnard, Phys. Rev. 122, 607 (1961).

G.R. Caughlan and W.A. Fowler, Astrophys. J. 136, 435 (1962).

H.C. Chow, Ph.D. Thesis, University of British Columbia, (1973).

R.F. Christy and I. Duck, Nucl. Phys. 24, 89 (1961).

S.C. Curran and J.E. Strothers, Nature 145, 224 (1940).

G. Dearnaley, Rev. Sci. Instr. 31, 197 (1960).

J.J. Domingo, Nucl. Phys. 61, 39 (1965).

T.W. Donnelly, Ph.D. Thesis, University of British Columbia, (1967).

L.A. Dubridge, S.W. Barnes, J.H. Buck and C.V. Strain, Phys. Rev. 53, 447 (1938).

S. El Kateb, Private communications, (1972).

P.M. Endt and C. Van der Leun, Nucl. Phys. A105, 1 (1967).

F.J. Eppling, PhD. Thesis, University of Wisconsin, (1952).

F.J. Eppling, J.R. Cameron, R.H. Davis, Ajay S. Divatia, A.J. Galonsky, E. Goldberg and R.W. Hill, Phys. Rev. 91, 438(A) (1953).

F.J. Eppling, et. al., "AECU-3110, Annual Progress Report Covering Researches from June 1, 1954 to May 31, 1955, Massachusetts Institute of Technology" (1955).

W.A. Fowler, C.C. Lauritsen and A.V.Tollestrup, Phys. Rev. 76, 1767 (1949).

G.M. Griffiths, Comptes Rendus du Congress International de Physique Nucleaire, Paris, 447 (1958).

G.M. Griffiths, M. Lal and L.P. Robertson, Conference proceedings on "Electromagnetic Lifetimes and Properties of Nuclear States", Nuclear Science Series. Report No. 37 (1962a).

G.M. Griffiths, E.A. Larson and L.P. Robertson, Can. J. Phys. 40, 402 (1962b).

D.F. Hebbard, Nucl. Phys. 15, 289 (1960).

R.R. Henry, G.C. Phillips, C.W. Reich, and J.L. Russell, Bull. Am. Phys. Soc. 1, 96 (1956).

R.E. Hester, R.E. Pixley and W.A.S. Lamb, Phys. Rev. 111, 1604 (1958).

L. Holland, "Vacuum Deposition of Thin Films", Chapman and Hall Ltd., London, (1963).

H.L. Jackson, A.I. Galonsky, F.J. Eppling, R.W. Hill, E. Goldberg and J.R. Cameron, Phys. Rev. 89, 365 (1953).

J. Johnson, Pivate communication, (1972).

W.R. Kane and M.A. Mariscotti, Nucl. Instr. Methods 56, 189 (1967).

E. Kashy, R.R. Perry and J.R. Risser, Nucl. Instr. Methods 4, 167 (1959).

R.W. Kavanagh, Nucl. Phys. 15, 411 (1960).

K.S. Krane, Nucl. Instr. Methods 98, 205 (1972).

M. Lal, Ph.D. Thesis, University of British Columbia, (1961).

R.A. Laubenstein, M.J.W. Laubenstein, L.J. Koester and R.C. Mobley, Phys. Rev. 84, 12 (1951a).

R.A. Laubenstein and M.J.W. Laubenstein, Phys. Rev. 84, 18 (1951b).

Chin-Fan Leang, Compt. Rend. 255, 3155 (1962).

C.M. Lederer, J.M. Hollander and I. Perlman, "Table of Isotopes", John Wiley and Sons, Inc., New York (1967).

W.E. Meyerhof and N.W. Tanner, Phys. Rev. 115, 227 (1959).

E.A. Milne, Phys. Rev. 93, 762 (1954).

E.T. Mint, M.Sc. Thesis, University of British Columbia, (1970).

N.F. Mott and H.S.W. Massey, "The Theory of Atomic Collisions", Clarendon Press, Oxford (1965).

G.F. Nash, M.Sc.Thesis, University of British Columbia, (1959).

L.C. Northcliffe and R.F. Schilling, Nuclear Data Tables A7, 223 (1970).

M.A. Olivo, Ph.D. Thesis, University of British Columbia, (1968).

P.J. Riley, M.A.Sc. Thesis, University of British Columbia, (1958).

L.P. Robertson, M.A. Thesis, University of British Columbia, (1957).

C. Rolfs, Private communications, (1973).

M.E. Rose, Phys. Rev. 91, 610 (1953).

N. Tanner, Phys. Rev. 114, 1060 (1959).

W. Trost, H.J. Rose and F. Riess, Phys. Lett. 10, 83 (1964).

E. Vogt, Private communications, (1973).

J.B. Warren, K.A. Laurie, D.B. James and K.L. Erdman, Can. J. Phys. 32, 563 (1954).

J.B. Warren, T.K. Alexander and G.B. Chadwick, Phys. Rev. 101, 242 (1956).

W. Whaling, "California Institute of Technology Publication, revised" (1962).

H.H. Woodbury, A.V. Tollestrup and R.B. Day, Phys. Rev. 93, 1311 (1954).

L. Young, "Anodic Oxide Films", Academic Press, Inc., New York (1961).

L. Young, Private communications, (1972).

# APPENDIX A

## BEAM ENERGY CALIBRATION

The Van de Graaff beam energy was calibrated by using the many resonances of the $^{27}Al(p, \gamma)^{28}Si$ reaction, whose resonant energies are known accurately from 0.2 to 1.4 Mev (Endt and Van der Leun, 1967). The resonant energies used for beam calibration are shown in Table A.1. Resonances have also been studied at higher energies (Ibid), but for these energies the resonances have not been as accurately determined. Beam calibration at energies above 1.4 Mev was therefore based upon an extrapolation of the calibration determined over the lower energy range. Where possible, cross sections were measured at resonant energies. Where not, a calibration curve was determined for an energy region about the energy desired. For the short runs (< 20 min) taken when measuring the $^{16}O(p, p)^{16}O$ cross section, a single calibration was made before each run. For the long direct capture runs (many hours), the beam energy was calibrated before and after each run.

The aluminum target that was used was one made by S. El Kateb (1972). It consisted of a thin (≃ 1 Kev to 1 Mev protons) layer of aluminum deposited by evaporation onto a tantalum backing. It was situated in the extended Faraday cup of each chamber (Figs. 3.1 and 3.6) to allow close positioning of the 5 inch x 5 inch NaI crystal, which was used to count the gamma rays. The counting system included a single channel analyser whose window was set to maximize the signal-to-noise ratio, following the information given on the decay schemes from each of the levels that was excited (Ibid). The yields were large and for 2μa

| Resonance Energy (Kev) | Exitation Energy (Mev) | $\Gamma$ (ev) | Energy Window of S.C.A. (Mev) |
|---|---|---|---|
| 405.5 ± 0.3 | 11.974 | X | 4 to 8 |
| 504.88 ± 0.15 | 12.070 | < 175 | 9 to 13 |
| 506.9 ± 0.2 | 12.072 | < 145 | 9 to 13 |
| 632.6 ± 0.2 | 12.192 | < 30 | 6 to 13 |
| 678.6 ± 0.8 | 12.237 | X | 9 to 12 |
| 731.3 ± 0.2 | 12.288 | < 110 | 9 to 12 |
| 773.70 ± 0.03 | 12.329 | 14 ± 3 | 10.5 to 13 |
| 922.6 ± 0.2 | 12.472 | < 120 | 4 to 13 |
| 991.912 ± 0.043 | 12.583 | 100 ± 15 | 9 to 12 |
| 1118.4 ± 0.2 | 12.661 | 760 ± 80 | 3.5 to 8 |
| 1262.2 ± 0.3 | 12.800 | 100 ± 40 | 5 to 13 |
| 1363.72 ± 0.07 | 12.898 | 70 ± 40 | 3 to 13 |
| 1364.8 ± 0.5 | 12.899 | ≈ 1100 | 3 to 13 |
| 1381.3 ± 0.3 | 12.915 | 640 ± 60 | 3 to 13 |
| 1388.4 ± 0.3 | 12.922 | 550 ± 110 | 3 to 13 |

Table A.1 : $^{27}Al(p,\gamma)^{28}Si$ resonances used for beam energy calibration (from Endt and Van Der Leun, 1967).

beam current a running time of a few seconds per data point was usually sufficient. Fluctuation in the beam energy was about ± ¼ Kev. The energy was incremented in steps of ½ or 1 Kev.

The Van de Graaff energy was monitored in two independent ways. There was a generating voltmeter, located in the top of the high pressure vessel that enclosed the machine, so that it was facing the positive high voltage terminal. The output signal was connected to the operational amplifier of a digital voltmeter calibrated with scale divisions every 0.1 Kev. In addition there was a nuclear magnetic resonance probe (Alpha Scientific, Inc., N.M.R. Digital Gaussmeter, Model 3093) placed in the field of the 90° analysing magnet. This probe read the magnetic field directly to an accuracy of 1 : $10^5$ and indicated the value digitally in kilogauss. The magnetic field, B, and the beam energy, E, are related by

$$E = \text{constant} \times B^2 \qquad \text{- A.1}$$

The error in the voltmeter reading of a certain real beam energy is a function of many operating conditions, mostly, however, of the tank pressure and humidity. The error varies from day to day and during the course of a long run. The error also varies as a function of the beam energy, but with a very nearly linear dependence. For a voltmeter reading corresponding to a certain real beam energy, the NMR reading will depend upon the path of the beam through the 90° magnet. That is, on the position of the magnet box with respect to the vertical column of the Van de Graaff and on the focussing conditions on the beam.

A typical resonance curve showing the yield versus the voltmeter reading and a typical calibration of the beam energy at low energies to be used for

extrapolation to higher energies is shown in Fig. A.1. Care was taken to avoid changing the focussing conditions on the beam (before it left the 90° magnetic) between a beam calibration run and a cross section measurement. Because of the normalization techniques used for the $^{16}O(p, p)^{16}O$ cross section (section 3.1a), a single tank pressure had to be used which gave stable machine operation at the minimum and maximum energies used since changing the tank pressure would change the beam calibration. A pressure of about 90 lbs/in$^2$ accomplished this and the calibration of these runs was straightforward and reliable to < 1 Kev at the lower energies while somewhat worse for the higher energies.

For the $^{16}O(p, \gamma)^{17}F$ runs, the tank pressure increased steadily with time because of the heat generated by the running of the belt and this caused the voltmeter reading to drift. At energies above 2 Mev, the voltmeter would sometimes exhibit occasional discontinuous jumps of a few Kev. And occasionally the beam focussing would have to be adjusted to maintain sufficient current on the target. For these cases, the reliability of the beam calibration could be estimated by comparing the voltmeter and NMR readings at which a resonance was found before and after the run. For some of the direct capture runs, the beam calibration was reliable, for others it was very uncertain. Therefore, beam energy calibrations for the direct capture runs were supplemented with energy calibrations from the (p, $\gamma$) spectra.

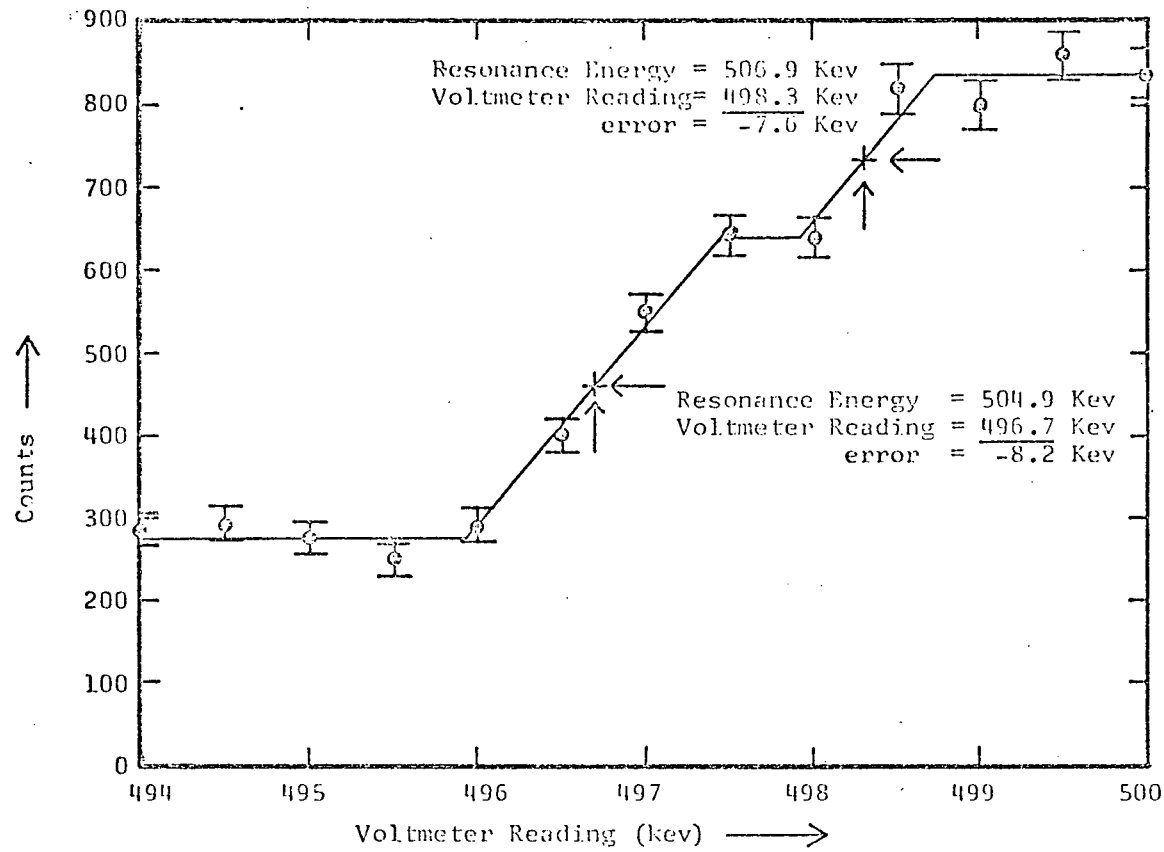


(a) : $^{27}Al(p,\gamma)^{28}Si$ resonance yield curve.

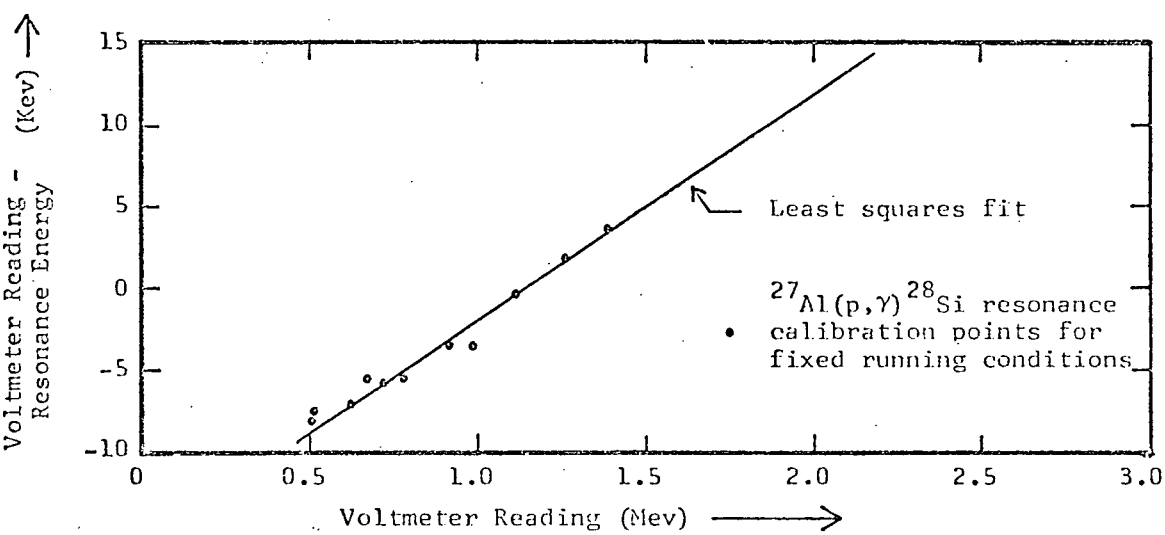


(b) : Beam calibration curve.

Figure A.1 : Van de Graaff beam energy calibration.

# APPENDIX B

## CALIBRATION OF THE GAMMA RAY DETECTOR

The gamma rays emitted following the direct capture of the incident protons by the $^{16}O$ target nuclei were detected with a large volume lithium-drifted germanium crystal. Earlier measurements of this reaction, made before the recent development of semiconductor gamma ray detectors, were made using NaI(Tℓ) scintillators. The latter detectors have the advantage of a large intrinsic gamma ray absorption efficiency which, for the larger scintillators, may approach 100% full energy absorption for 2 Mev photons compared to about 9% for the Ge(Li) crystal used here. However, by extending the running times to periods from 4 to 40 hours per run, statistical errors were reduced until they were comparable to or less than other experimental errors. NaI(Tℓ) detectors have the disadvantage of poorer energy resolution, giving a peak FWHM of about 100 Kev for 2 Mev photons compared to about 5 Kev for the Ge(Li) detectors. This leads, in many cases, to a poorer signal-to-noise ratio and in all cases it yields energy spectra in which the recognition and definition of the peaks of interest is very much more difficult in the presence of background peaks. Whereas the smaller absorption efficiency of the Ge(Li) detector can, in principle, be overcome by increased running time, except when signal-to-noise ratio is too low, the poorer energy resolution of the NaI(Tℓ) detector very often prohibits their use for the precise determination of peak intensities regardless of the counting statistics. In addition, the Ge(Li) detector energy resolution made it possible to resolve the 0.4953 Mev $\gamma 3$ peak from the 0.511 Mev annhilation peak which would not have been possible with a

NaI(Tℓ) detector. As a result it was possible to use the isotropy of $\gamma 3$ for normalizing the angular distribution data (section 3.2a).

The Nuclear Diodes Inc. Ge(Li) detector used in this work is of the closed-end circular coaxial design. Fig. B.1 shows the dimensions of of the crystal and its location within the cryostat, along with a schematic representation of its connection to the cold finger, high voltage supply and pre-amplifier input. The system includes a Nuclear Diodes model #103 fast, DC coupled, low noise pre-amplifier mounted rigidly to the cryostat. The crystal was operated with a bias of +2000 volts.

Three operating characteristics of the detector had to be determined quantitatively; the intrinsic absorbtion efficiency for a range of gamma ray energies, the effective solid angle and the relative absorption as a function of angle from its axis. It was also necessary to subtract the "single escape" contribution of $\gamma 1$ from the full energy peak of $\gamma 2$. The determination of each of these detector characteristics is discussed below.

Detector Efficiency Function

An expression for the direct capture reaction yield is given in eqn. 3.3a. The quantity $d\Omega\ \varepsilon\ T$ defined there is the "full energy peak detector efficiency function" and refers to the number of counts obtained in the full energy peak of the energy spectrum for a particular set of operating conditions. It includes the effective solid angle, $d\Omega$, subtended by the detector as seen from the beam spot, the "intrinsic full energy peak efficiency factor", $\varepsilon$, which is the fraction, of those photons which are geometrically incident on the crystal, that interact in such a way that they

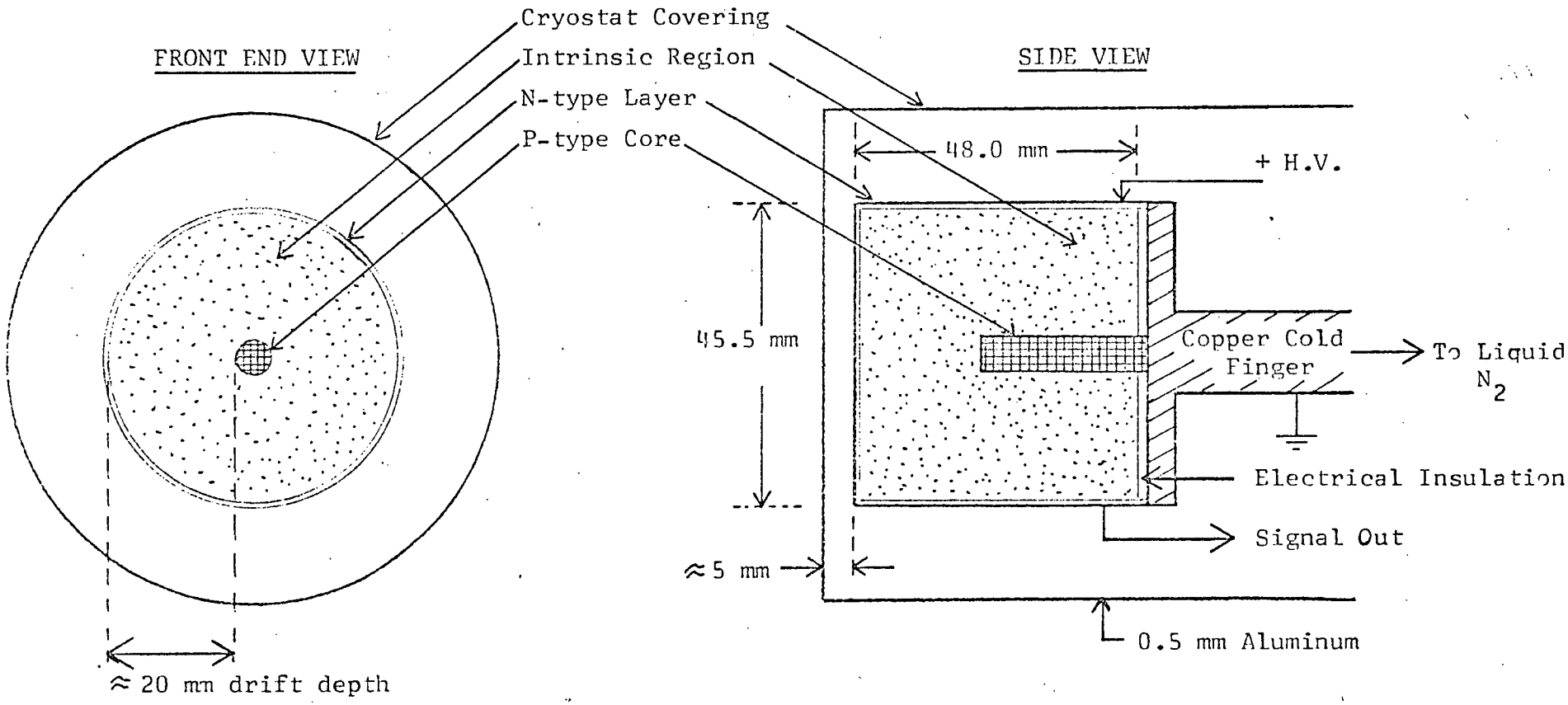


Rated efficiency : 13.8% relative to a 3" x 3" NaI scintillator at 25 cm distance for the 1.332 Mev peak of $^{60}Co$.

Figure B.1 : Nuclear Diodes Inc. Ge(Li) detector dimensions.

deposit all of their energy, and T, a transmission factor to account for absorption of gamma rays by materials in the path from the target to the detector. The absorption of the full energy of an incident photon can result from one of the following processes:

1) Photoelectric absorption.

2) Compton scattering followed by secondary absorption of the scattered photon.

3) Pair production for $E_\gamma \geq 2m_o c^2$ when both 0.511 Mev photons from the subsequent decay of the positron are totally absorbed. (One photon escaping gives rise to the "single escape" peak, 0.511 Mev below the full energy peak and both escaping gives the "double escape" peak).

The transmission factor, T, depends not only upon the vacuum enclosure over the detector but also upon the scattering chamber, the target, the target holder, and any other material present between the target and detector.

The yield from a gamma ray source can be expressed as

$$N_c = N_\gamma \frac{d\Omega}{4\pi} \varepsilon T \qquad \text{- B.1}$$

where $N_c$ = number of counts/sec in the full energy peak.

$N_\gamma$ = number of photons/sec emitted by the source

$\frac{d\Omega}{4\pi}$ = the fraction of a sphere subtended by the detector

$\varepsilon$ = the intrinsic full energy peak efficiency factor

T = the transmission coefficient (including source material and source mounting)

Therefore, from spectra that determine $N_\gamma$/sec and $N_c$/sec, the detector efficiency function, $d\Omega\ \varepsilon\ T$, is specified by the relation

$$\frac{4\pi N_c}{N_\gamma} = d\Omega \, \varepsilon \, T \qquad \text{-B.2}$$

From calibrated gamma sources which provide values of $N_\gamma$ over a sufficient range of energies, this efficiency can be determined as a function of photon energy. Furthermore, by juxtaposing these sources, one at a time, over the visible beam spot remaining after direct capture measurements, and thereby giving the same spatial ($d\Omega$) and absorbing (T) geometries for the two cases, a direct, experimentally determined absolute calibration of the Ge(Li) detector can be made. This was done for a total of nine geometries, one for each combination of detector position, target and target holder, and with or without a Cd-Cu-Al absorber in position. This graded absorber was placed in front of the detector for runs at higher energies to reduce the high count rate from x-rays.

Two types of sources were used to provide gamma rays of accurately known intensity over the required energy range. One was a set of eight absolutely calibrated gamma ray sources obtained from the International Atomic Energy Agency Laboratory, Selbersdorf, Austria. The specifications are quoted in Table B.1. This set was checked against an older set made by the same laboratory and for all of the sources there was agreement within the stated errors. The other type was a $^{228}$Th source, made to request by New England Nuclear, Inc. This was used to obtain a value of $d\Omega \, \varepsilon \, T$ at 2.6145 Mev relative to its value at 0.583 Mev by using the known ratio, 1.174 : 1.000 ± 1% respectively, of the intensities of these two transitions in the $^{228}$Th spectrum (Kane and Mariscotti, 1967).

Before the value of $N_\gamma$ for each photon energy could be used, the activity of the set of eight IAEA sources had to be up-dated (± 1 day)

| Nucleus | Initial Activity ($\mu$Ci) | Half Life | Photon Energy (Kev) | % of Disinti - gration | Source & Source Holder Self - Absorption |
|---|---|---|---|---|---|
| $^{241}_{Am}$ | 10.38 ± 0.7% | 432.9 ±0.8 years | 59.543 | 35.9 ±0.6 | 3.8 % |
| $^{57}_{Co}$ | 11.43 ± 1.0% | 271.6 ±0.5 days | 121.97<br>136.33 | 85.0 ±1.7<br>11.4 ±1.3 | 2.3 %<br>2.2 % |
| $^{203}_{Hg}$ | Not Used | | | | |
| $^{22}_{Na}$ | 9.16 ± 1.0% | 2.602 ±0.005 years | 511.006<br>1274.55 | 181.1 ±0.2<br>99.95±0.02 | 1.3 %<br>0.86% |
| $^{137}_{Cs}$ | 10.35 ± 1.8% | 30.5 ± 0.3 years | 661.635 | 85.1 ±0.4 | 1.2 % |
| $^{54}_{Mn}$ | 10.96 ± 0.7% | 312.6 ±0.3 days | 834.81 | 100.00 | 1.1 % |
| $^{60}_{Co}$ | 10.57 ± 0.6% | 5.28 ±0.01 years | 1173.23<br>1332.49 | 99.87±0.05<br>99.999±0.001 | 0.9 %<br>0.85% |
| $^{88}_{Y}$ | 10.85 ± 1.2% | 107.4 ±0.8 days | 898.04<br>1836.13 | 91.4 ±0.7<br>99.4 ±0.1 | 1.0 %<br>0.7 % |

Calibration date : January 1, 1970 , 00.00 Universal Time

Schematic of source holder :

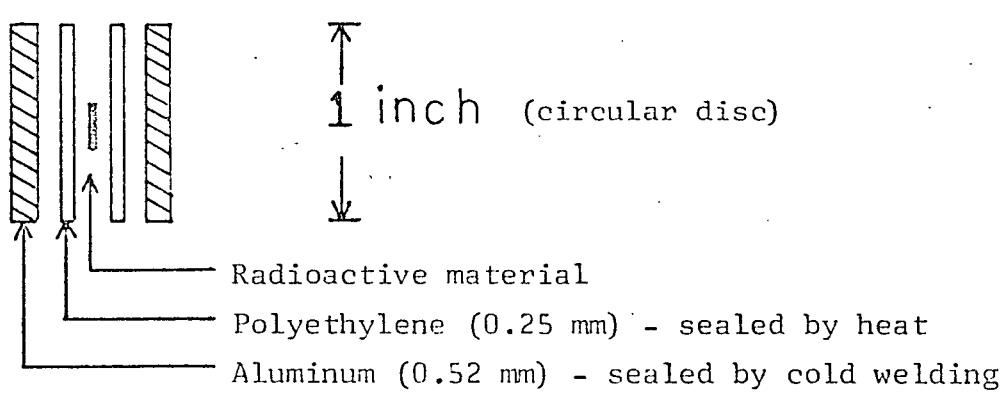


Table B.1 : IAEA source and source holder specifications.

to the time the calibration was made, and each of the intensities had to be corrected for further self-absorption because the source discs were placed at different angles with respect to the detector for the different geometries used. The values of $N_c$ were determined with a simple detector-pre-amplifier-linear amplifier-multichannel analyser system. Counting rate losses were determined by comparing the ratio of counts from a pulse generator fed into both the test input of the pre-amplifier and directly into a scaler (section 3.2c). Spectra were taken with greater than $10^4$ counts in the full energy peaks. Peak areas were found with a computer program which made a linear or second degree least squares background subtraction followed by summing of the counts per channel remaining. In all cases, $N_c$ was determined to < 1%.

This data was plotted onto large graph paper and fitted by eye with a smooth curve. It is also possible to fit the efficiency function data to various analytical functions of the energy (Kane and Mariscotti, 1967) but this was not necessary here. The values of $d\Omega\ \varepsilon\ T$ needed for differential cross section calculations (eqn. 3.4) were read from these graphs. A typical calibration curve is shown in Fig. B.2.

Detector Mapping Function

As discussed by Rose (1953), angular correlation and angular distribution data must be corrected because of the finite solid angle subtended by the detector. Only then can it represent "true" data, that would have resulted had a point detector been used, and be compared with theoretical calculations. According to Rose this correction is most simply made if the data is expressed as coefficients of a Legendre Polymonial series.

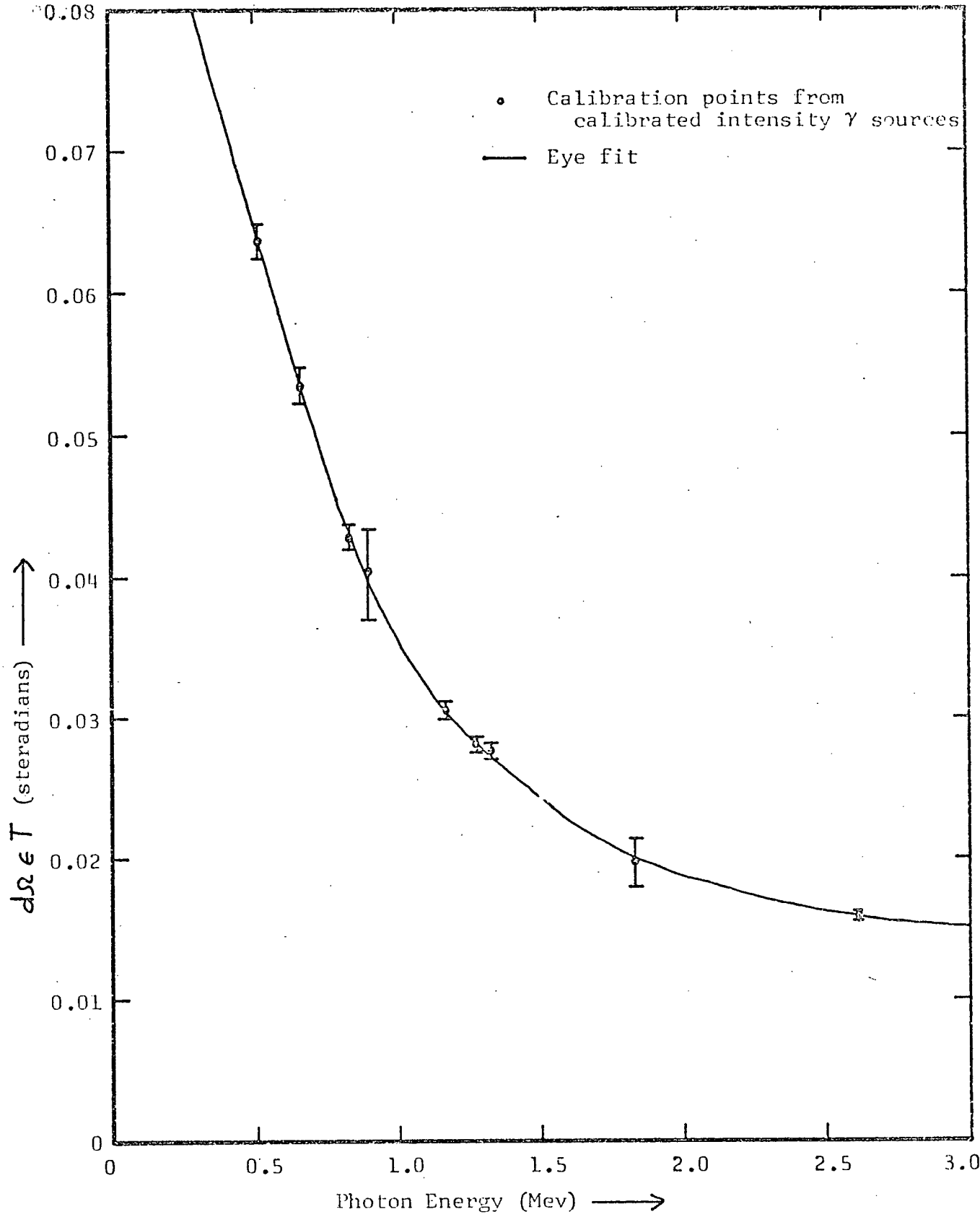


Figure B.2 : Ge(Li) detector efficiency function "$d\Omega\,\epsilon\,T$"; one of nine.

For this case,

$$W_{exp}(\theta) = \sum_{\ell} B_{\ell} P_{\ell} (\cos \theta) \qquad \text{-B.3}$$

$$W_{true}(\theta) = \sum_{\ell} A_{\ell} P_{\ell} (\cos \theta) \qquad \text{-B.4}$$

where $W_{exp}(\theta)$ and $W_{true}(\theta)$ are the experimental and true angular distribution functions

$B_{\ell}$ and $A_{\ell}$ are the amplitude coefficients for each Legendre Polynomial $P_{\ell}(\cos \theta)$ of order $\ell$.

Then $$B_{\ell} = Q_{\ell} A_{\ell} \qquad \text{-B.5}$$

where $$Q_{\ell} = J_{\ell} / J_{o} = \text{the "Rose 'smoothing' or 'Q' factors"} \qquad \text{-B.6}$$

where $$J_{\ell} = \int_{o}^{\beta_{max}} P_{\ell}(\cos \beta)\left(1 - e^{-\tau x(\beta)}\right) \sin \beta \, d\beta \qquad \text{-B.7}$$

where $\tau$ = detector absorption coefficient

$\beta$ = angle from detector axis

$x(\beta)$ = path length through detector at angle $\beta$.

The term, $1 - e^{-\tau x(\beta)}$, appearing in the $J_{\ell}$, represents the fractional absorption of the detector as a function of angle, $\beta$, from its axis. This can either be calculated or measured directly (Krane, 1972).

A detailed consideration of the theorectical absorption mechanism of a Ge(Li) crystal of the design used here presents one with a rather formidable calculation. Inaccurate knowledge of the size and shape of the p-core, edge effects, and inhomogeneous efficiency per unit volume due to non-uniform electric fields are some of the conditions that make unattractive the simplifying assumptions that would be necessary before such a calculation would be feasible. The method used here was to determine experimentally the "detector mapping function" defined as

$$F(\beta) = 1 - e^{-\tau x(\beta)} \qquad \text{-B.8}$$

The procedure was to map the absorption of the detector by scanning it in the $\beta$ direction with a strong, well collimated $^{228}$Th source. The only assumption made was that the crystal absorbed symetrically in the azimuthal direction. This follows reasonably from its circular coaxial design.

The 10 mc $^{228}$Th source that was used was obtained from the Amersham/ Searle Corp. The relative efficiency was measured at intervals of 2° from the detector axis for three gamma ray energies, 0.583, 0.860 and 2.6145 Mev, which are prominant in the $^{228}$Th spectrum, and for two target-to-detector distances. The results are shown in Fig. B.3. By interpolating, $F(\beta)$ can be determined for any photon energy. However, its variation with energy was not very great. Further mapping for positive and negative values of $\beta$ revealed that the position of the crystal within the cryostat is displaced from the center by approximately 1° as seen by the target.

The smoothing factors, $Q_\ell$, were determined for each direct capture photon energy and each detector geometry by numerically integrating the function

$$\int_0^{\beta_{max}} P_\ell(\cos\beta)\, F(\beta) \sin\beta \, d\beta$$

for each $F(\beta)$. These $Q_\ell$ were used, together with the experimental angular distribution data, as the input data for the angular distribution fitting program (Chapter 5).

Ratio of Single Escape to Full Energy Peaks versus Energy

The two direct capture gamma transitions, $\gamma 1$ and $\gamma 2$, are separated

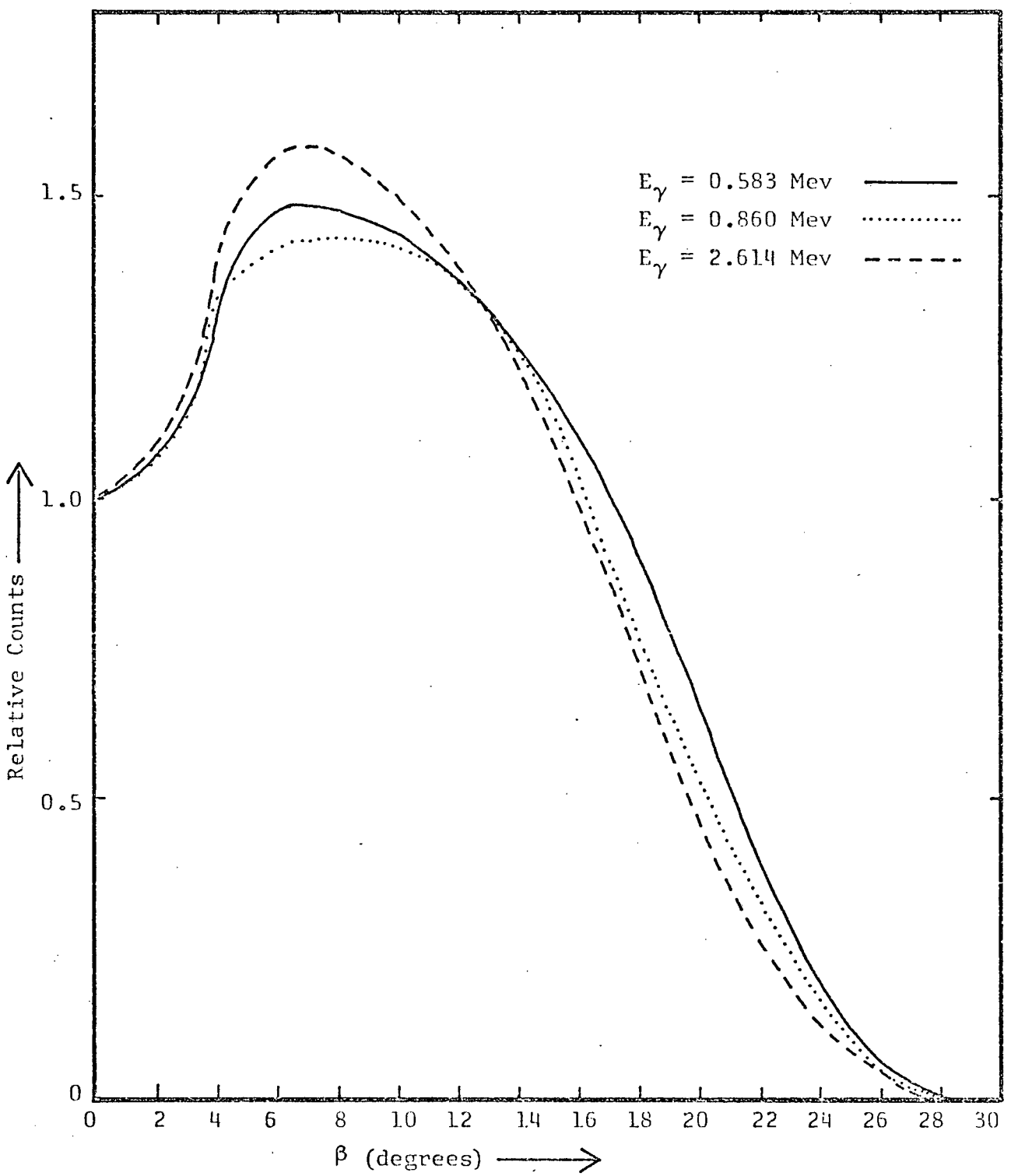


Figure B.3 : Ge(Li) detector "mapping function".

by 0.4953 Mev, the energy of the first excited state in $^{17}F$. Therefore, the energy of $\gamma 2$ is always 0.4953 Mev less than the energy of $\gamma 1$ regardless of the reaction energy. Because of the pair production mechanism of photon interaction, the interaction of a photon of energy $E(> 2m_0c^2)$ can lead to the absorption by the detector of energy E(full energy (FE) peak), $E - m_0c^2$ (single escape (SE) peak) or $E - 2m_0c^2$ (double escape (DE) peak). And because of the extensive broadening of the direct capture peaks through beam energy loss in the target, the SE peak of $\gamma 1$ will be embedded within the FE peak of $\gamma 2$. This must be corrected for before the correct intensity of $\gamma 2$ can be found. The ratios of SE/FE and DE/FE versus photon energy for this detector, as determined by Johnson (1972), is shown in Fig. B.4. The correction itself is discussed in section 4.2a.

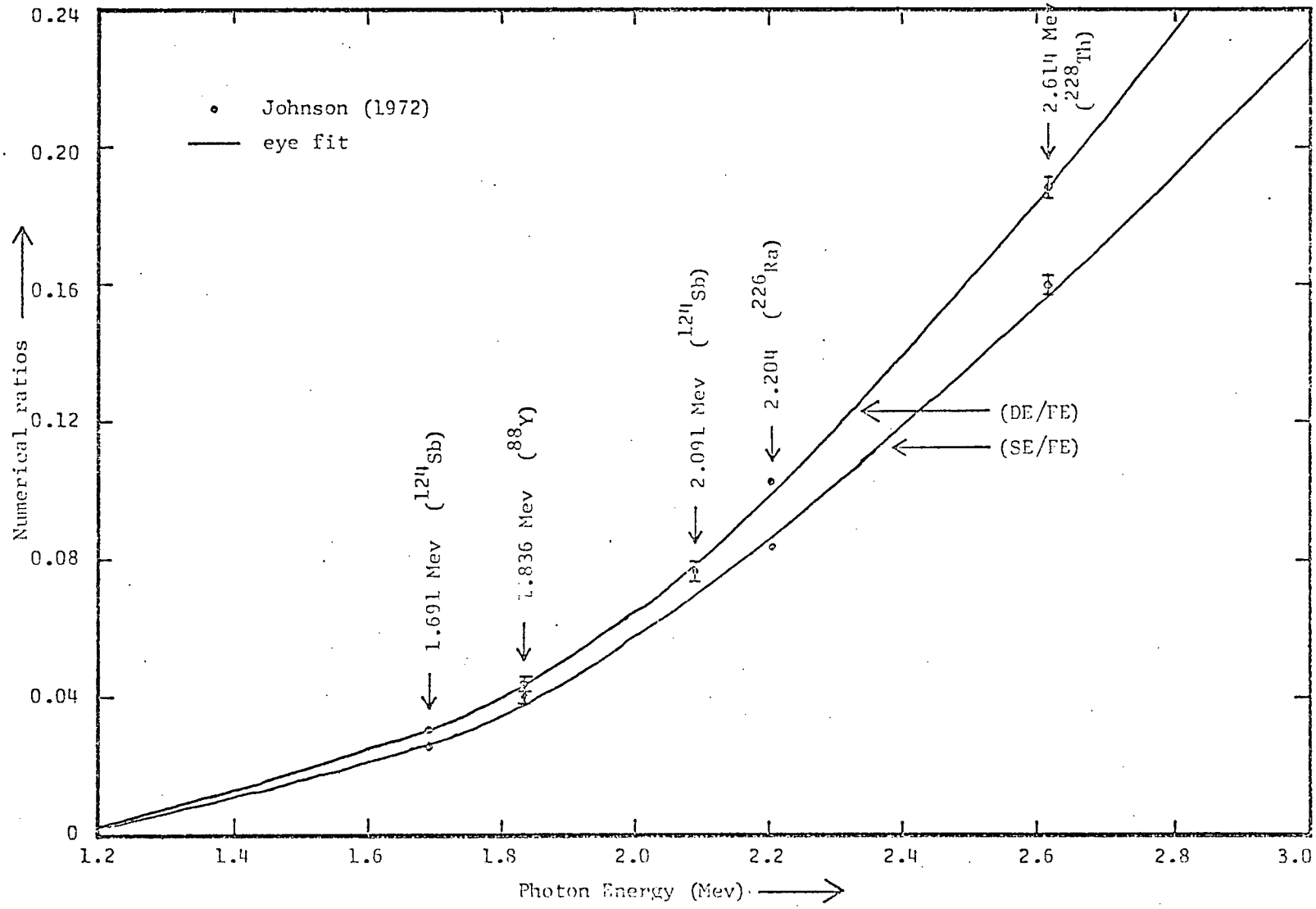


Figure B.4 : Ratios of single escape (SE) and double escape (DE) peaks to the full energy (FE) peak for the Ge(Li) detector.

# APPENDIX C

## BEAM - TARGET INTERACTION

The data obtained in nuclear reaction measurements is in most cases an average over a range of energies and angles as a result of target thickness and geometrical sizes of targets and detectors. It is important to take these factors into consideration when interpreting the results.

### Reaction Energy

A beam of protons incident upon a target will suffer an energy loss (but no appreciable change in direction) as a result of ionization and excitation of the atomic electrons in the target. The laboratory energies for the scattering or capture of the protons are determined by the incident beam energy (Appendix A) corrected for energy losses in the target (section 2.4a). In the case of scattering, the energies of the protons which are incident on the detector after being scattered are determined by the kinematics of the elastic scattering as well as by energy losses involved in going into the target to the point of scattering and coming out again.

The energetics of the energy loss suffered by the beam in the Au-$WO_3$ targets before and after being scattered by $^{16}O$ nuclei, are shown schematically in Figs. C.1 and C.2 where:

Notation: 1, 2, 3 = front surface, gold-oxide interface, rear surface

$C_F$, $C_R$ = carbon layers on front, rear surface

Unprimed, primed = before, after scattering event

$E_i$ = proton energy at location i (= 1, 2, 3) before scattering

$(E_i)'_x$ = " " " i ( " ) after "

by nucleus x (= Au, W, O, C).

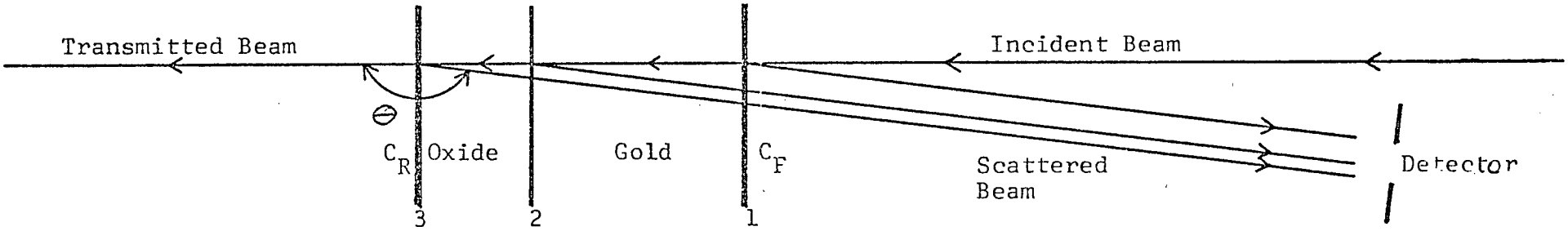


| Target Location | PROTON ENERGY (LABORATORY) | | | | | | | | | | |
|---|---|---|---|---|---|---|---|---|---|---|---|
| | Incident | Scattered | | | | | Detected | | | | |
| | | Au | W | O | $C_F$ | $C_R$ | Au | W | O | $C_F$ | $C_R$ |
| 1 | $E_1$ = Bombarding Energy | $(E_1)'_{Au}$ | | | $(E_1)'_C$ | | $(E_1)'_{Au}$ | | | $(E_1)'_C$ | |
| 2 | $E_2 = E_1 - \Delta(Au)$ | $(E_2)'_{Au}$ | $(E_2)'_W$ | $(E_2)'_O$ | | | $(E_2)'_{Au} - \Delta'(Au)$ | $(E_2)'_W - \Delta'(Au)$ | $(E_2)'_O - \Delta'(Au)$ | | |
| 3 | $E_3 = E_1 - \Delta(Au + Oxide)$ | | $(E_3)'_W$ | $(E_3)'_O$ | | $(E_3)'_C$ | | $(E_3)'_W - \Delta'(Au + Oxide)$ | $(E_3)'_O - \Delta'(Au + Oxide)$ | | $(E_3)'_C - \Delta'(Au + Oxide)$ |

Figure C.1 : Beam energy loss in target.

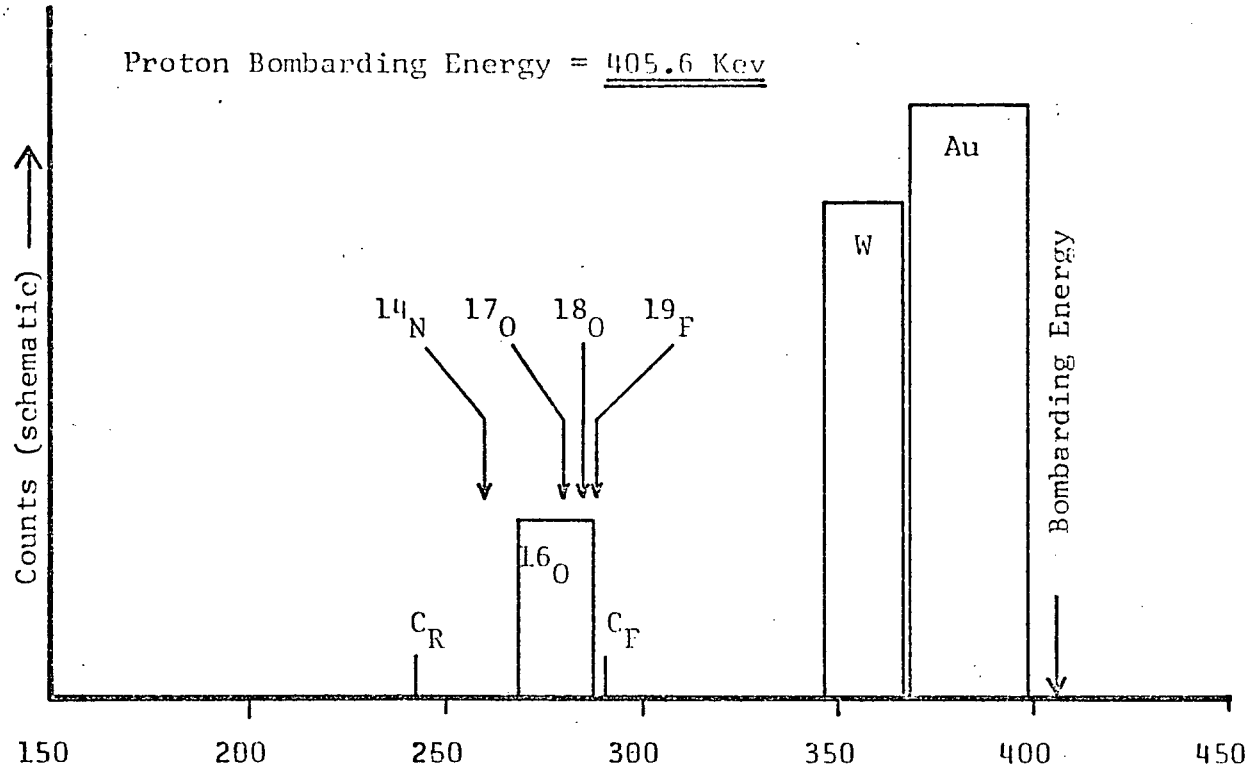


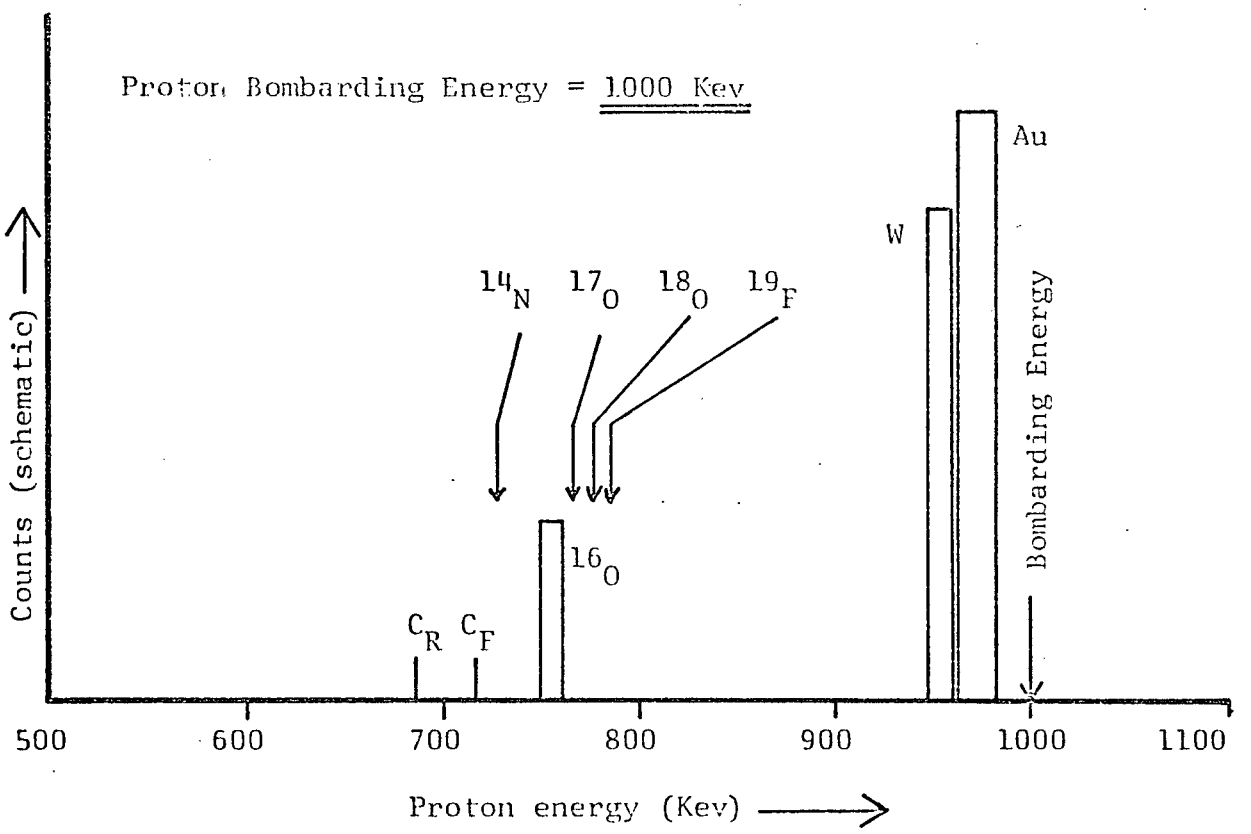


Figure C.2 : "Ideal" scattering spectra (target #16).

Certain features of the beam energy loss and their affect on the scattering spectra become apparent from Figs. C.1 and C.2. The $C_R$ peak is effectively biased in energy below the low energy side of the oxygen peak by approximately the energy difference between the scattering of the protons from $^{16}O$ and $^{12}C$. Facing the oxide layer toward the beam would have shifted the gold peak to lower energy and the tungsten and oxygen peaks to higher energy, and increased the interference between the oxygen peak and the low energy tail of the Au-W peak at the lower energy runs. In fact, this interference effectively limited the allowable thicknesses of the Au and $WO_3$ layers. Also, it can be seen that even with accurate knowledge of the incident beam energy and the energy losses in the two target layers, the mass identification of a particular background peak or, alternatively, the position within the spectrum of the peak from a contaminant of a given mass, depends upon some assumption about the distribution of the contaminant within the target. The carbon contamination was found to be located in equal proportions on the front and rear surfaces of the target (section 3.1b). Considerations for any other possible contaminants were made assuming them to be distributed uniformly throughout the $WO_3$ layer. This follows reasonably from the particularly clean nature of the gold and its deposition by evaporation in contrast to the inherently "dirty" sputtering process. The position of peaks that would arise from scattering from $^{13}C$, $^{14}N$, $^{17}O$, $^{18}O$, $^{19}F$ are shown in Fig. C.2.

Scattering Angle

A beam of protons incident upon a target will be deflected (but without appreciable energy loss) due to scattering by the nuclei of the

target material. This scattering is predominantly small angle scattering by the large Z nuclei. For reference, 0.4 Mev protons scattered by gold nuclei must be scattered by 50° before losing 1 Kev energy. For the thickness of the targets used, the incident protons will, on the average, suffer many scatterings and the resulting angular spread of the beam should be described by the theory of multiple scattering.

For such multiple scattering, a parallel beam of incident protons will emerge, from the target, distributed normally about the incident direction in a cone whose R.M.S. half-angle at "1/e" height is $[\theta]_{RMS}$ (Mott and Massey, 1965). Calculations were made to determine $[\theta]_{RMS}$ or, equivalently, the half-angle at one standard deviation, $\theta_s = [\theta]_{RMS}/\sqrt{2}$, for the various running conditions.